



Spatiotemporal variability of evapotranspiration in Suterhland

L Sello



orcid.org 0000-0002-8559-3560

Dissertation accepted in fulfilment of the requirements for
the degree *Master of Science in Geography and
Environmental Management* at the North-West University

Supervisor: Dr RP Burger

Co-supervisor: Dr G Mahed

Graduation October 2019

24308277

ACKNOWLEDGEMENTS

All thanks to the power of the Almighty. One who gave me the strength and wisdom to complete my thesis.

Special thanks to my mom for all the sacrifices, patience and encouragement throughout my schooling career. The moral support from my family is also highly treasured.

I cordially wish to express my sincere gratitude to my supervisors, Dr. Gaathier Mahed, for funding this research, his scholarly suggestion and teaching me R. I am also grateful to Dr. Roelof Burger, my co-supervisor for his data visualisation input and structuring my thesis. The involvement of both of you is held in high esteem.

I would like to thank my friends for their undying support through bad and good times. More especially Luckson Muyemeki for teaching me ILWIS.

ABSTRACT

In a semi-arid and water scarce country like South Africa with a significant number of consumers of water, it is pivotal to determine the rate of evapotranspiration with a high degree of certainty. Measurements of evapotranspiration can be useful in areas where the demand for water exceeds the supply thereof. Precise measurements of spatiotemporal variability of evapotranspiration are pivotal in disciplines of meteorology, agriculture and hydrology, especially in semi-arid and arid areas where water scarcity is becoming a hindrance on economic welfare and sustainable development.

Evapotranspiration models have been developed with a combination of remote sensing and meteorological data inputs. After careful consideration of the various surface energy balance algorithm which include; surface energy balance index, surface energy balance system, simplified surface energy balance index, mapping evapotranspiration with internalized calibration and surface energy balance algorithm for land. The surface energy balance algorithm for land was selected because of its success rate of modelling evapotranspiration in semi-arid areas. The pre-packaged Surface Energy Balance Algorithm for Land model along with Landsat 7 satellite imagery, was used to determine the parameters of the energy balance model and the spatiotemporal variability of evapotranspiration. The spatiotemporal variability of the evapotranspiration quantified with Landsat 7 was validated with the American Society of Civil Engineers Reference evapotranspiration equation (ASCE ETSZ).

The study was conducted for the 8th, 24th of December 2009 and the 9th of January 2010 in Sutherland. The SEBAL results showed a good agreement with the ASCE ETSZ results for the 24th of December 2009 with evapotranspiration rates of 0.52mm and 0.29mm, respectively. A good agreement between ASCE ETSZ and SEBAL evapotranspiration measurements was also obtained for the 9th of January 2010, with evapotranspiration readings of 0.44m and 0.37mm, respectively. However for the satellite image acquired on the 8th of December 2009 the evapotranspiration measurements were not in agreement with the point based measurement, with a reading of 0.9mm and 0.3mm, respectively. It was concluded that in order to achieve a high degree of remotely sensed evapotranspiration measurements, point-based instruments which cover a larger spatial area should be utilised.

Keywords: Evapotranspiration, Semi-arid, Remote sensing, ILWIS, Reference evapotranspiration

Table of Contents

ACKNOWLEDGEMENTS	II
ABSTRACT	III
LIST OF FIGURES	VII
LIST OF TABLES	IX
LIST OF ABBREVIATIONS	X
1. INTRODUCTION	1
1.1 BACKGROUND TO RESEARCH	1
1.2 JUSTIFICATION AND PROBLEM STATEMENT	2
1.3 OBJECTIVES OF THE STUDY.....	5
2. LITERATURE REVIEW	7
2.1 OVERVIEW OF EVAPOTRANSPIRATION	7
2.2 FACTORS REGULATING EVAPOTRANSPIRATION.....	9
2.3 EVOLUTION AND ADVANCES OF REMOTE SENSING IN ENVIRONMENTAL STUDIES	12
2.4 SURFACE ENERGY BUDGET AND SURFACE ENERGY BALANCE MODELS	17
2.5 SURFACE ENERGY BALANCE MODELS.....	20
2.5.1 SURFACE ENERGY BALANCE INDEX (SEBI)	20
2.5.2 SURFACE ENERGY BALANCE SYSTEM (SEBS)	21
2.5.3 SIMPLIFIED SURFACE ENERGY BALANCE INDEX (S-SEBI).....	23
2.5.4 SURFACE ENERGY BALANCE ALGORITHM FOR LAND (SEBAL)	25
2.5.5 MAPPING EVAPOTRANSPIRATION AT HIGH RESOLUTION AND WITH INTERNALIZED CALIBRATION (METRIC).....	28
2.5.6 TWO-SOURCE MODELS (TSM)	29
2.6 APPLICATION OF SEBAL WITH LANDSAT 7	31
2.7 METHODS OF ESTIMATING EVAPOTRANSPIRATION	33
3. MATERIALS AND METHODS	36
3.1 VALIDATION SITE AND STUDY BACKGROUND	36
3.1.1 CLIMATE.....	37
3.1.2 GEOLOGY AND GEOHYDROLOGY.....	37
3.2 METHODOLOGY	41

3.2.1	REMOTE SENSING ACQUISITION AND PREPROCESSING	41
3.2.2	SATELLITE DATA	41
3.2.3	CONVERSION TO RADIANCE.....	41
3.2.4	RADIANCE TO REFLECTANCE	43
3.2.5	CONVERSION OF BAND 6 INTO LAND SURFACE TEMPERATURE	44
3.3	SOLAR ZENITH ANGLE	44
3.3.1	SOLAR DECLINATION	44
3.3.2	EQUATION OF TIME	45
3.3.3	LOCAL APPARENT TIME (LAT).....	45
3.3.4	HOUR ANGLE.....	45
3.3.5	SOLAR ZENITH ANGLE/ THE SOLAR INCIDENCE ANGLE	46
3.3.6	CONVERSION OF REFLECTANCE (ρ) AND TEMPERATURE (T_{rad}) INTO MAPS	47
3.4	SEBAL METHODOLOGY	47
3.4.1	PLANETARY ALBEDO (r_p).....	48
3.4.2	BROADBAND SURFACE ALBEDO (r_o)	49
3.5	BIO PHYSICAL PARAMETERS	49
3.5.1	NORMALIZED DIFFERENCE VEGETATION INDEX.....	50
3.5.2	SOIL ADJUSTED VEGETATION INDEX (SAVI)	51
3.5.3	LEAF AREA INDEX.....	53
3.5.4	AERODYNAMIC ROUGHNESS LENGTH (Z_{om})	53
3.5.5	SURFACE ROUGHNESS FOR HEAT TRANSPORT (Z_{oh})	54
3.5.6	DISPLACEMENT HEIGHT AND WIND PROFILE	54
3.6	SURFACE EMISSIVITY.....	55
3.7	INCOMING SHORTWAVE RADIATION.....	56
3.8	SOIL HEAT FLUX	56
3.9	SENSIBLE HEAT FLUX (H)	57
3.9.1	AERODYNAMIC RESISTANCE TO HEAT TRANSPORT (r_{ah}).....	58
3.9.2	FRICTION VELOCITY (u^*)	58
3.9.3	WIND SPEED AT BLENDING HEIGHT (U_B)	59

3.9.4	MONIN-OBUKHOV LENGTH (L)	59
3.9.5	CORRECTION FACTORS	60
3.10	INSTANTANEOUS LATENT HEAT FLUX	63
3.11	EVAPORATIVE FRACTION	63
3.12	DAILY NET RADIATION	63
3.13	DAILY EVAPOTRANSPIRATION	66
3.14	REFERENCE EVAPOTRANSPIRATION EQUATION	66
3.15	CHARACTERISING EVAPORATION AND RAINFALL DATA OF SUTHERLAND	67
4.	RESULTS AND DISCUSSION	68
4.1	EVAPORATION AND RAINFALL DATA FROM AN A-CLASS TYPE PAN	68
4.2	SPATIOTEMPORAL VARIABILITY OF SURFACE ENERGY BALANCE PARAMETERS	70
4.2.1	RELATIONSHIP BETWEEN SURFACE TEMPERATURE AND LATENT HEAT FLUX	70
4.2.2	LATENT HEAT FLUX	71
4.2.3	SOIL HEAT FLUX	72
4.2.4	RN DAY	73
4.2.5	NORMALISED DIFFERENCE IN VEGETATION INDEX	73
4.3	SPATIOTEMPORAL VARIABILITY IN EVAPOTRANSPIRATION MEASUREMENTS	76
5.	CONCLUSION AND RECOMMENDATIONS	78
5.1	RESEARCH SUMMARY AND RECOMMENDATIONS	78
5.2	LIMITATIONS	79
5.3	CONTRIBUTION TO THE BODY OF KNOWLEDGE	79
6.	REFERENCE LIST	80
	APPENDIX A	95
	APPENDIX B	98
	APPENDIX C	99

LIST OF FIGURES

Figure 1: The global hydrological cycle (Trenberth et al., 2007)	2
Figure 2: Figure showing the leaf stomata (Allen <i>et al.</i> , 1998)	8
Figure 3: Figure showing the factors regulating the rate of evapotranspiration (Allen <i>et al.</i> , 1998)	10
Figure 4: Representation of the role of advective air over irrigated and dry land (McMahon <i>et al.</i> , 2013).....	11
Figure 5: Representation of the net radiation components	18
Figure 6: Schematic relationship between surface reflectance and surface temperature in the S-SEBI algorithm (Roerink <i>et al.</i> , 2009; Li <i>et al.</i> , 2009 and Liou and Kar, 2014).....	24
Figure 7: The primary components required in a SEBAL model (Bastiaanssen, 1998)	26
Figure 8: Locality map of Sutherland	36
Figure 9 : Land use/cover map of Sutherland (Landsat, 2014)	39
Figure 10: Actual framework of how to determine evapotranspiration (Opoku-Duah <i>et al.</i> , 2008)	47
Figure 11: Typical reflectance spectrum of a stressed and healthy plant (Kumar and Silva, 1973, cited by Govaerts and Verhulst, 2010)	50
Figure 12: Actual framework of deriving the Soil Adjusted Vegetation Index value (Bala 2010)	52
Figure 13: Inversely proportional relationship between wind speed and height (Immerzeel <i>et al.</i> , 2006).....	55
Figure 14: Solving for coefficients using the dry and wet pixels	62
Figure 15: The iterative process used to determine sensible heat flux values (Bala, 2010)	62
Figure 16: Class-A type pan	67
Figure 17: Class A pan-type evaporation and precipitation data from the year 1983-2009	68
Figure 18: Class A pan-type Monthly evaporation and precipitation data from the year 1983-2009.....	69
Figure 19: Relationship between surface temperature and latent heat flux obtained with SEBAL	70

Figure 20: Spatiotemporal measurements of surface temperature estimated with SEBAL for cloud free days on December 4 th , 2000; December 24 th , 2009; January 09 th , 2010.....	71
Figure 21: Spatiotemporal measurements of latent heat flux estimated with SEBAL for cloud free days on December 4 th , 2000; December 24 th , 2009; January 09 th , 2010.	72
Figure 22: Spatiotemporal measurements of soil heat flux estimated with SEBAL for cloud free days on December 4 th , 2000; December 24 th , 2009; January 09 th , 2010.	72
Figure 23: Spatiotemporal measurements of daily net radiation estimated with SEBAL for cloud free days on December 4 th , 2000, December 24 th , 2009, January 09 th , 2010.....	73
Figure 24: Spatiotemporal measurements of NDVI estimated with SEBAL for cloud free days on December 4 th , 2000, December 24 th , 2009, January 09 th , 2010.....	74
Figure 25: Relationship between NDVI and surface temperature	75
Figure 26: Spatiotemporal measurements of evapotranspiration estimated with SEBAL for cloud free days on December 4 th , 2000, December 24 th , 2009, January 09 th , 2010.....	76
Figure 27: Comparison of the daily evapotranspiration estimated with SEBAL and ASCE ETSZ equation	77
Figure 28: Solving for correlation coefficient satellite for satellite image acquired on the 24 th of December 2009	98
Figure 29: Solving for correlation coefficient for satellite image acquired on the 9 th of January 2010.....	98
Figure 30: Iterative process for stabilising the sensible heat flux value, for the image acquired on the 8 th of December 2009.....	99
Figure 31: Iterative process for stabilising the sensible heat flux value, for the image acquired on the 24 th of December 2009.....	99
Figure 32: Iterative process for stabilising the sensible heat flux value, for the image acquired on the 9 th of January 2010	99

LIST OF TABLES

Table 1: Summary of various satellite imaging systems.....	15
Table 2: Summary of remote sensing models.....	30
Table 3: The various Landsat satellites, sensors, bandwidths and spatial resolution	31
Table 4: A summary of four methods of estimating evapotranspiration	34
Table 5: Stratigraphy of the Karoo Supergroup.....	37
Table 6: Satellite imaging data acquired for the study.....	41
Table 7: Spectral radiance range for Landsat 7 in watts	43

LIST OF ABBREVIATIONS

LIST OF SYMBOLS	
a_s	: CONSTANT VALUE OF 0.25
b_s	: CONSTANT VALUE OF 0.5
C_1	: IS A CONSTANT TAKEN AS 0.13 FOR COMPUTING LAI
C_1	: FREE PARAMETER EQUAL TO 20.6
C_1	: THE CLOUDINESS FACTOR, CONSTANT VALUE OF 0.9
C_1	: CONSTANT VALUE OF -5.5
C_2	: IS A CONSTANT TAKEN AS 0.35 FOR COMPUTING LAI
C_2	: CONSTANT VALUE OF 5.8
C_a	: DENSITY OF THE AIR 1.17 KG M ⁻³
C_p	: THE SPECIFIC AIR HEAT (JKG ⁻¹ K ⁻¹)
$Cos\theta$: SOLAR INCIDENT ANGLE
d_1	: THE CLOUDINESS FACTOR, CONSTANT VALUE OF 0.1
d_a	: DAY ANGLE
d_n	: JULIAN DAY
d_r	: EARTH-SUN DISTANCE IN ASTRONOMICAL UNITS
e_d	: SATURATION VAPOR PRESSURE
e_{sky}	: EMISSIVITY OF THE AIR
E_t	: EQUATION OF TIME
ET_{24}	: DAILY EVAPOTRANSPIRATION MM/DAY
ET_{sz}	: STANDARDIZED REFERENCE CROP EVAPOTRANSPIRATION
$f_{cloudiness}$: THE CLOUDINESS FACTOR
G_0	: SOIL HEAT FLUX(W/M ⁻²)

L_c	:	LONGITUDE
L_λ	:	SPECTRAL RADIANCE AT THE SENSOR'S APERTURE
R_a	:	EXTRA-TERRESTRIAL SOLAR IRRADIANCE
r_{ah}	:	AERODYNAMIC RESISTANCE TO HEAT TRANSPORT BETWEEN REFERENCE AND SURFACE LEVEL(SM^{-1})
$R_L \uparrow$:	LONGWAVE OUTGOING
$R_L \downarrow$:	LONGWAVE INCOMING
R_n	:	NET RADIATION
R_{nl}	:	LONG WAVE RADIATION
R_{ns}	:	NET SHORT-WAVE RADIATION
r_o	:	BROADBAND ALBEDO
r_p	:	PLANETARY ALBEDO
R_s	:	GLOBAL SOLAR RADIATION
$R_s \uparrow$:	SHORTWAVE OUTGOING
$R_s \downarrow$:	SHORTWAVE INCOMING
$R_s \downarrow$:	INCOMING SHORTWAVE RADIATION
Rn_{day}	:	TOTAL DAILY NET RADIATION
s_c	:	SOLAR CONSTANT
\mathcal{T}_a	:	TRANSMISSIVITY OF THE ATMOSPHERE
T_a	:	AIR TEMPERATURE
T_s	:	SURFACE TEMPERATURE
U_*	:	FRICITION VELOCITY IN (MS^{-1})
U_b	:	WIND VELOCITY AT BLENDING HEIGHT TAKEN AS 200 METERS(MS^{-1}).
U_{ref}	:	WIND SPEED FROM THE METEOROLOGICAL WEATHER STATION.

Z_0	:	SURFACE ROUGHNESS
Z_B	:	BLENDING HEIGHT 200M
Z_{oh}	:	SURFACE ROUGHNESS FOR HEAT TRANSPORT
Z_{om}	:	SURFACE ROUGHNESS FOR MOMENTUM TRANSPORT
Z_{ref}	:	THE REFERENCE HEIGHT FOR THE DETERMINATION OF WIND SPEED AT 2M.
ϵ_0	:	SURFACE EMISSIVITY
ϵ_a	:	APPARENT EMISSIVITY
Λ_{ins}	:	INSTANTANEOUS EVAPORATIVE FRACTION
ρ_{air}	:	THE DENSITY OF THE AIR
ρ_p	:	UNITLESS PLANETARY REFLECTANCE
τ^2	:	TRANSMISSIVITY
τ_{day}	:	DAILY TRANSMITTANCE
ϕ	:	LATITUDE PIXEL
c	:	EMPIRICAL COEFFICIENTS
d	:	EMPIRICAL COEFFICIENTS
d	:	DISPLACEMENT HEIGHT
dT	:	THE VARIATION BETWEEN THE AIR TEMPERATURE AND THE AERODYNAMIC TEMPERATURE OF THE NEAR SURFACE
$ESUN_\lambda$:	MEAN SOLAR SPECTRAL IRRADIANCES
g	:	GRAVITATIONAL FORCE
h	:	VEGETATION HEIGHT
H	:	SENSIBLE HEAT FLUX (W/M ²)
K	:	VON KARMAN'S CONSTANT (0.41)

K1	:	CALIBRATION CONSTANT 1= 666.09 W/ (M ² * STER * MM)
K2	:	CALIBRATION CONSTANT 2 =1282.71 KELVIN
L	:	ADJUSTMENT FACTOR(0.5)
L	:	MONIN-OBUKHOV LENGTH
LAT	:	LOCAL APPARENT TIME
LE	:	LATENT ENERGY FLUX
n	:	SUNSHINE HOURS
N	:	DAY LENGTH
N	:	NUMBER OF PIXELS
T	:	EFFECTIVE AT-SATELLITE TEMPERATURE IN KELVIN
α	:	SURFACE ALBEDO
δ	:	SOLAR DECLINATION
μm	:	MICROMETER
σ	:	STEFAN-BOLTZMANN CONSTANT
Xh	:	CORRECTION FACTOR FOR HEAT TRANSPORT
Xm	:	CORRECTION FACTOR FOR MOMENTUM TRANSPORT
ψh	:	CORRECTION FACTOR FOR HEAT TRANSFER
ψm	:	CORRECTION FACTOR FOR MOMENTUM TRANSFER
ω	:	HOUR ANGLE

1. INTRODUCTION

The introduction of the dissertation will be discussed under chapter 1. This chapter will introduce the background of the research, justification for pursuing this research and the objectives of the study.

1.1 BACKGROUND TO RESEARCH

South Africa is considered as a water-stressed country because the majority of the land is regarded as semi-arid (Gibson, 2013) having recorded an average of 403mm rainfall during the drought period of 2015 (WWF-SA, 2016). South Africa's annual rainfall averages less than 500mm $year^{-1}$, with average evaporation rates of 1800mm $year^{-1}$, whereas the global rainfall averages around 814mm $year^{-1}$ (Fisher *et al.*, 2005; Gibson, 2013). However, two-thirds of the global rainfall is returned back to the atmosphere as evapotranspiration (Jato-Espino *et al.*, 2017; Oki and Kanae, 2006). Thus evapotranspiration is the most sizeable parameter of the terrestrial hydrological cycle after precipitation (Glenn *et al.*, 2007; Shoko *et al.*, 2015).

In semi-arid and arid regions, water is predominantly lost in the water budget through evapotranspiration processes (Jin *et al.*, 2013). Variations in evapotranspiration processes tend to alter the spatial distribution of water sources (Maeda, 2011; Jin *et al.*, 2013). The uneven spatial distribution of rainfall across South Africa results in the uneven availability of water, with two-thirds of the country inheriting a smaller fraction of the national rainfall average (Gibson *et al.*, 2013).

In the arid and semi-arid regions, water resources are restricted leading to low levels of water being available for domestic and irrigation purposes (Laounia *et al.*, 2017). This process of the water cycle is predominantly governed by incoming solar radiation. Water is vaporized from land and ocean surfaces, conveyed by winds, and precipitated to create clouds which produce, rain, snow, hail, sleet that falls to the ocean and land (Trenberth *et al.*, 2007). Soil moisture or snow can be a form of temporary storage of precipitation over land. The remaining surplus of precipitation is stored as groundwater or runs-off and creates rivers and streams, which causes an outflow of freshwater into oceans, as a result completing the terrestrial hydrological cycle (Trenberth *et al.*, 2007), Figure 1.

The parameters associated with the hydrological cycle such as the energy inside the oceans, salt minerals and various nutrients on the land surface are redistributed and transported inside the Earth's climate system (Chahine, 1992 and Schlesinger 1997, cited by Trenberth, 2011).

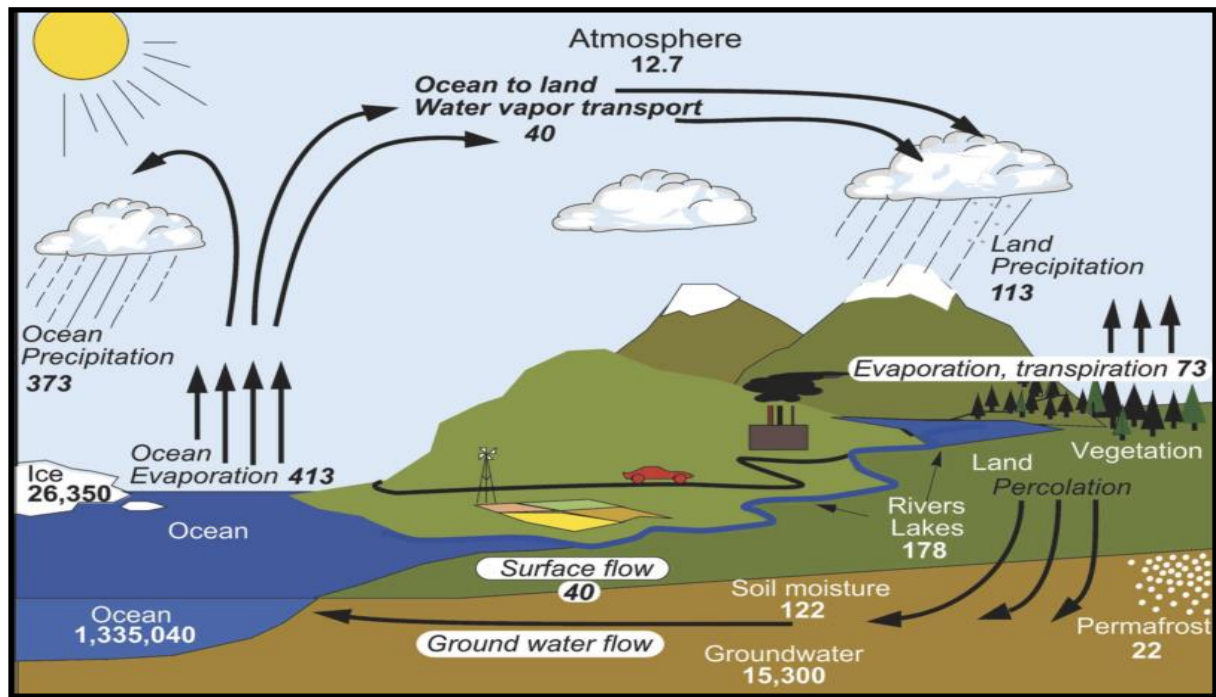


Figure 1: The global hydrological cycle (Trenberth et al., 2007)

Numerous studies have endeavored to gain a comprehensive perspective of the global hydrological cycle (Oki and Kanae, 2006). However, our understanding of the various parameters of the hydrological cycle is still limited due, to a lack of representative data for oceanic precipitation, terrestrial run-off and surface evaporation amongst other hydrological outputs (Trenberth et al., 2007). Acquiring reliable values of the different components of the hydrological cycle is also problematic (Trenberth et al., 2007).

1.2 JUSTIFICATION AND PROBLEM STATEMENT

The issue facing irrigated agriculture today is to enhance the world's food production whilst enhancing food security through more effective and efficient use of water (Bandara, 2006). In order for current agricultural practices to sustain communities by 2025, approximately 17% more irrigated water will be required (Engelbrecht and Engelbrecht, 2016). This leaves a burden for Southern African countries situated in semi-arid and arid areas as groundwater and surface water are a scarce resource (Bouman, 2007).

Comprehensive knowledge and access to South Africa's groundwater resources is pivotal in eradicating the country's water security issues. Today only a small fraction of 15% of the country's groundwater is being abstracted for consumption (WWF-SA, 2016). In most cases, the communities that rely on groundwater have no other form of alternative water sources. The African Ministers Council on Water announced in 2008 that groundwater resources will play a strategic and essential role in Africa, specifically for communities that are neglected and most vulnerable (WWF-SA, 2016).

It is predicted that the global near-surface temperature experiences a 3 degrees increase annually (Engelbrecht et al., 2015). The International Panel on Climate Change, Third Assessment Report concluded that this increase in surface temperature is closely associated with anthropogenic climate change (Houghton *et al.*, 2001). Should this trend of an increase in surface temperature strengthen or persist in the 21st century, severe impacts will not only be limited to a reduction in soil-moisture availability but also impact on agriculture (Thornton et al., 2011) and biodiversity (Engelbrecht and Engelbrecht, 2016; Engelbrecht et al., 2015). Anthropogenic climate change and an increase in surface temperature has the ability to decrease water availability and intensify the magnitude of drought impact (Danodia et al., 2017; Sperna Weiland et al., 2012; Trenberth et al., 2007).

Drought impacts have rapidly increased in parts of the United States and Africa (Trenberth *et al.*, 2007). It has been proven that anthropogenic climate change influences the magnitude, duration and the frequency of the drought (Diffenbaugh, 2015). The droughts that were experienced in the Sahel and the Horn of Africa are realistic examples of Africa's potential risk of being exposed to drought under climate change (Lyon and Dewitt, 2012). Prolonged periods of droughts have affected both the non-agricultural and agricultural sectors in South Africa (Hedden and Cilliers, 2014). The president of South Africa announced on the 16th of January 2004 that six provinces are considered disaster zones and 4 million citizens were exposed to a threat of a decline in food security due to drought (International Federation of Red Cross, 2004). In 2003, 2006, 2008 and 2011 the community of Setlagole in the North-West province was exposed to extreme drought events (Shoroma, 2014). This manifested in a decline of crop production and an increase in livestock mortality of more than 50 000 units (Shoroma, 2014).

One of the big questions in hydrology is, what are the impacts associated with a warmer climate, will a warmer climate intensify the terrestrial hydrological cycle and if so to what extent? There is an overwhelming concern with this question because an intensified terrestrial hydrological cycle will intensify the frequency of droughts, floods and storms (Huntington, 2006). These challenges can be mitigated through technically and effective remotely sensed estimations of evapotranspiration (Danodia et al., 2017).

With the recent precipitation fluctuations and increasing temperature, crop yield and water availability will be reduced in the near future (Benites and Castellanos, 2015; Kang et al., 2009). The cause of crop yield failure and low production of crops in a rainfed agriculture system is because of low levels of water in the soil (Gill and Punt, 2010). This is caused by erratic and low levels of rainfall as well as poor management of available water resources (Benites and Castellanos, 2015). The management of soil moisture is of cardinal importance in flood predictions and irrigation management (Vey et al., 2016). Enhancing water availability in the soil can result in reduced risk of agricultural yield, improved agricultural yields, maintenance of high levels of water in wells and the continuity of stream flows and rivers (Benites and Castellanos, 2015).

The application of remote sensing techniques can be utilised to examine agricultural variables (nutrients, yield, water, etc.) which represents a significant source of information that can be utilised to increase agricultural yield and enhance water management (Cordova et al., 2015; Kogan, 1999). Soil water content or soil moisture, together with evapotranspiration measurements, can be a key indicator of future and current irrigation needs (Hassan-esfahani et al., 2015, 2014).

Comprehensive knowledge of soil moisture content, latent (LE) and sensible (H) heat fluxes is indispensable for numerous environmental applications including; irrigation management systems, drought, plant growth monitoring, plant water demand and productivity (Anderson et al., 2007; Dodds et al., 2005). It is still difficult to make precise measurements of evapotranspiration, especially in data scarce and spatially heterogeneous areas (Kiptala et al., 2013), because evapotranspiration varies in space and time (Tsouni et al., 2008). Precise measurements of evapotranspiration are not only significant for climate change but also have applications in hydrological modeling and monitoring, weather forecasting and drought monitoring (Anderson et al., 2007; Bastiaanssen et al., 2002; Gibson, 2013; Zhao et al., 2013). In addition, evapotranspiration is of paramount importance in both the energy and water balance, mainly because of the link it provides between the land surface energy balance and the land surface water balance (Khaldi et al., 2011; Zhao et al., 2013).

With frequent updates, satellite images have shown positive results in measuring spatial information of evapotranspiration at different temporal and spatial scales, even in regions where meteorological data may be limited (Jin, 2013; Gibson *et al.*, 2013; Majozi *et al.*, 2017). Information found in the near-infrared, thermal infrared and visible band can be applied in retrieving atmospheric temperature, land surface temperature and vegetation index (Su, 2002). These parameters can then be used as useful inputs to model evapotranspiration and surface fluxes based on the energy balance equation (Liou and Kar, 2014).

Therefore, for the purpose of this study, a remote sensing approach using the surface energy balance algorithm (SEBAL) and Landsat imaging system will be used to determine the accuracy of remotely sensed evapotranspiration measurements as compared to point based measurements. The main reason for using a remote sensing approach and SEBAL is because remote sensing estimates provide large spatiotemporal variability of evapotranspiration as compared to point based measurements (Khaldi *et al.*, 2011; Shoko *et al.*, 2015). Secondly, SEBAL is a commonly utilised remotely sensed model that determines the parameters of the surface energy balance and evapotranspiration, by integrating meteorological data and satellite imagery (Numata *et al.*, 2017). Thirdly, SEBAL has shown great prospects in determining the rate of evapotranspiration over large heterogeneous areas using minimum ground-based meteorological data (Kiptala *et al.*, 2013a; Su *et al.*, 2003; Tasumi *et al.*, 2003). Lastly, SEBAL has an internal automatic correction which eludes the rectification of atmospheric effects on surface temperature and it can be applied in arid and semi-arid regions (Liou and Kar, 2014).

1.3 OBJECTIVES OF THE STUDY

Evapotranspiration can be quantified at multiple scales ranging from a basin to a forest to a leaf (Senay *et al.*, 2011) or from a global, to continental, to a regional scale, to a mesoscale (Kustas and Norman, 1996). However, this research is focused on determining the spatiotemporal variability of evapotranspiration measurements in a mesoscale. The measurements will be done on a daily basis because of its applications in agriculture, hydrology and the climatology (Kustas and Norman, 1996).

Evapotranspiration measurements calculated on a monthly or an annual basis are more applicable to climatological applications than agricultural practices and hydrology (Kustas and Norman, 1996). The objectives of this study are given as follows:

1. Characterising the rainfall and evaporation data of Sutherland;

2. Assessing and mapping the spatiotemporal evapotranspiration measurements by utilising LANDSAT 7 products, SEBAL model and Integrated Land and Water Information System; and
3. Validating the spatiotemporal evapotranspiration maps acquired through remote sensing techniques with ground based meteorological data, which is used as inputs in the American Society of Civil Engineers Reference Evapotranspiration Equation (ASCE ETSZ).

Ultimately the aim of the study is to validate the satellite-based evapotranspiration measurements with the ground-based evapotranspiration measurements . Mainly, because field validation of remotely sensed evapotranspiration measurements is a necessity, which allows for the utilisation of remotely sensed data with a high degree of certainty (Gibson, 2013).

2. LITERATURE REVIEW

Chapter 2 is focused on the literature review that will be discussed under 7 sub-sections. The first sub-section (2.1), will give an overview of the concept of evapotranspiration. Sub-section (2.2) will focus on factors regulating the rate of evapotranspiration from your weather parameters to your environmental factors. Sub-section (2.3) gives an overview of the history of remote sensing and its applications in environmental science. There are different methods of determining evapotranspiration by using the surface energy balance algorithm, these methods including the surface energy balance will be discussed under subsection (2.4 and 2.5). This study uses the SEBAL model therefore, a subsection of SEBAL and its application to Landsat is presented in sub-section (2.6). The various methods of evapotranspiration that are commonly utilised are summarised in sub-section (2.7).

2.1 OVERVIEW OF EVAPOTRANSPIRATION

Evapotranspiration also known as actual evapotranspiration or consumptive use is explained as a combination of two processes whereby water is lost from transpiration and evaporation (Jovanovic et al., 2015; Ramoelo et al., 2014). Although, the partitioning of evapotranspiration into transpiration, soil evaporation is not well-known (Lawrence *et al.*, 2006). Transpiration tends to be the dominant contributor to evapotranspiration (Glenn et al., 2007). This can be validated by a study conducted by Ferreira *et al.*, (1996) in Portugal regarding the contribution of soil evaporation and plant transpiration to evapotranspiration. The study proved that transpiration had an 82% contribution to evapotranspiration and soil evaporation had an 18% contribution to evapotranspiration.

Evaporation is a single process where water is lost from the surface and where water changes its state from a gas to a liquid (Allen *et al.*, 1998; Kalma *et al.*, 2008; Verstraeten *et al.*, 2008; McMahon *et al.*, 2013). Water does not only evaporate from the soil surfaces but it tends to evaporate from an array of predominant sources of, vegetation, paved areas, and the atmosphere (Richard G. Allen et al., 1998; Senay et al., 2011).

Given that evaporation is occurring on a soil surface, the following two parameters tend to have an impact on the rate at which evaporation occurs; the magnitude of shading provided by the crop canopy and the quantity of water available on the surface (Todd et al., 1991). Various studies have proved that low levels of crop canopy cover and soggy soil surfaces result in a high ratio of evaporation as compared to transpiration (Hsiao and Xu, 2005). This can be validated by the study of Fereres and Villalobos (1990). Where the evaporation rate was 60%-80% for land cultivated with maize, cotton, and sunflower with a leaf area index of

0.6 to 1.2. The study Bethenod *et al.*, (2000) can also be used as an example, where the leaf area index was 4.0 and the soil evaporation was computed to be 10% of the total evapotranspiration.

Transpiration which is explained by Nouri *et al.*, (2013) as the direct evaporation from vegetation surfaces, accounts for the motion of water within a plant. Following the loss of water in the form of vapor through the plant's stomata (Alexandris and Stricevic, 2013). Vaporization tends to occur in the intercellular spaces of the leaf (Richard G. Allen *et al.*, 1998). Crops lose their water and some of its nutrients through the stomata as shown in Figure 2. These pores are explained as openings in the leaf through which carbon dioxide enters the leaf through assimilation as water vapor leaves the plant through transpiration (Richard G. Allen *et al.*, 1998; Cow and Ton, 1971). The rate of transpiration in the plants is controlled by the opening and closing of the stomata's pores (Richard G. Allen *et al.*, 1998). When the stomata have closed the rate of transpiration decreases; and when it opens transpiration increases (Yocum, 1935). Furthermore, the rate of transpiration in plants is influenced by the diameter of the stomata (Verstraeten *et al.*, 2008).

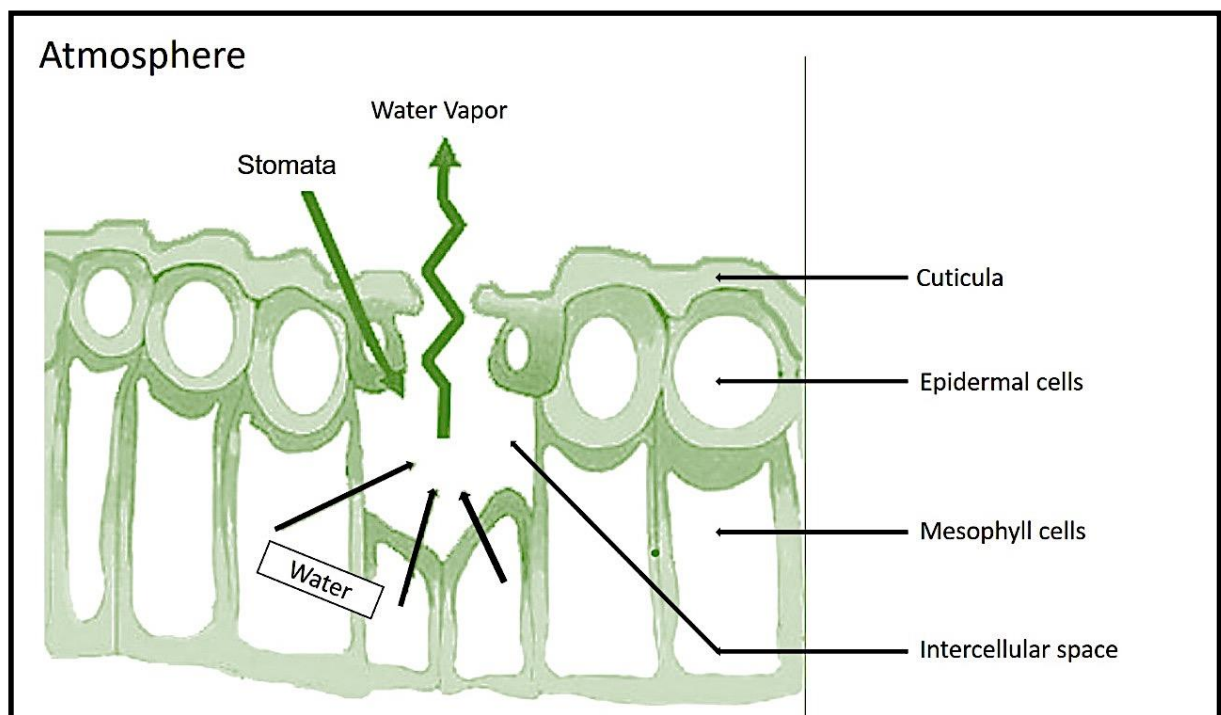


Figure 2: Figure showing the leaf stomata (Allen *et al.*, 1998)

Similar to evaporation, transpiration rates are influenced by the amount of solar radiation, wind speed, vapor pressure gradient, soil cover, and albedo (Alexandris and Stricevic, 2013). Hence, the latter parameters should be considered when determining the rate of both transpiration and evaporation (Richard G. Allen et al., 1998). In addition, the crop characteristics, cultivation practices, and environmental aspects are amongst other parameters which tend to influence the rate of transpiration (Alexandris and Stricevic, 2013). The transpiration process will only come to rest once the vegetation becomes stressed to the wilting point, which occurs when there isn't enough water for plants to transpire (Norton and Silvertooth, 2017).

A familiar topic related to evapotranspiration is reference evapotranspiration or potential evapotranspiration. According to Maeda *et al.*, (2011) reference evapotranspiration is simply defined as the rate of evapotranspiration that would occur from a cool-grass or alfalfa surface. However, the surface should have adequate supply of water (Alexandris and Stricevic, 2013; Brown, 2000). On the other hand, the American Society of Civil Engineers explained this phenomenon as “the ET rate from a uniform surface of dense actively growing vegetation having specified height and surface resistance (to transfer water vapor), not short of soil water, and representing an expanse of at least 100m of the same or similar vegetation” (Brown, 2000). If the rate of potential evapotranspiration is greater than the actual rate of evapotranspiration, plants will go to the state of complete wilting and soil surfaces will dry out (Alexandris and Stricevic, 2013).

In this manner, potential evapotranspiration is considered as the greatest evapotranspiration rate conceivable with a given octet of physical and meteorological parameters (Dingman, 1994). Thus, any supply of water that exceeds the potential evapotranspiration is solely wasted. Hence, the need for precise measurements of reference evapotranspiration for water resource management, planning and for irrigation scheduling (Lee and Cho, 2012).

2.2 FACTORS REGULATING EVAPOTRANSPIRATION

There are various factors which affect the process of evapotranspiration either (potential evapotranspiration or actual evapotranspiration), amongst those factors is crop characteristics, meteorological parameters and environmental factors (Courault et al., 2003; Kundu et al., 2015). Figure 3 represents the parameters which influence the rate of evapotranspiration.

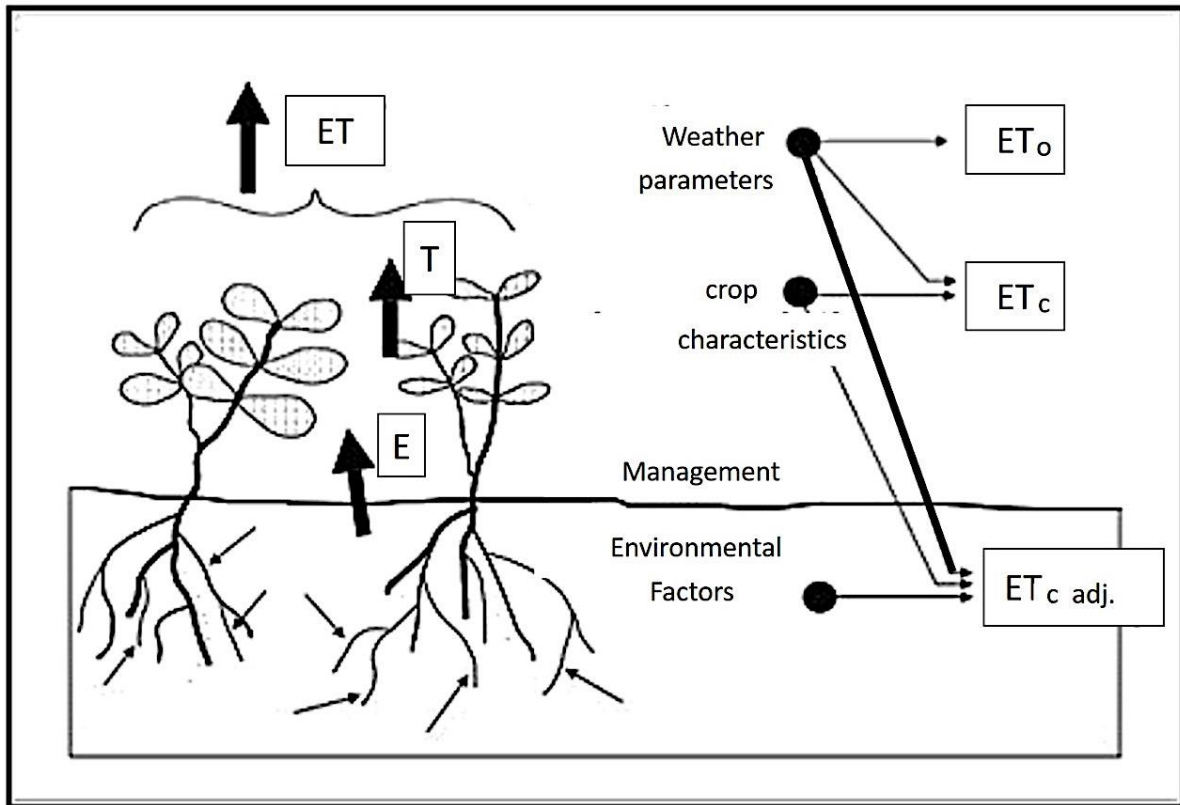


Figure 3:Figure showing the factors regulating the rate of evapotranspiration (Allen *et al.*, 1998)

The main meteorological parameters influencing the rate of evapotranspiration are; wind speed, air temperature, net solar radiation and humidity (Fisher *et al.*, 2005; Kalma and Mccabe, 2008).

The largest source of energy is by far solar radiation which ranges from infrared to the ultraviolet spectrum (Campillo *et al.*, 2012). Solar radiation or solar energy is explained as the energy emitted by the sun, this energy is in the form of electromagnetic radiation (Fu, 2003). Not all the radiation discharged by the sun reaches the Earth's surface, the ultraviolet wavelengths are normally absorbed by the Ozone layer and gases in the atmosphere (Campillo *et al.*, 2012). Furthermore, the total amount of solar radiation that reaches the Earth's surface depends on the turbidity of the atmosphere (Menon *et al.*, 2002; Ali *et al.*, 2013) and cloud cover, (Hatzianastassiou *et al.*, 2005).

Ambient air temperature is influenced by the amount of heat discharged to the Earth's surface and by the amount of solar radiation absorbed by the atmosphere. The rate of evapotranspiration in a vegetated area is controlled by sensible heat, where the air is transported over crops to exert this controlling influence (Liou and Kumar Kar, 2014). In cloudy

cool weather, the attenuation of vapor by evapotranspiration is less greater than in sunny warm weather (Allen *et al.*, 1998).

The energy supply from solar radiation and the ambient air may be the key drivers of evapotranspiration but the key factor that governs vapor removal is the difference between the ambient air and the water vapor pressure at the evapotranspiring locality (Katul and Parlange, 1992). Hot and dry areas consume a lot of water due to the great amount of solar radiation reaching the Earth's surface. However, in humid regions, the rate of evapotranspiration is fairly low because the air is close to saturation (Liou and Kumar Kar, 2014).

The mechanism of vapor removal does not solely depend on humidity, solar radiation and temperature. Air and wind turbulence is by far the most prominent regulating factor of vapor removal (Pearlmutter, 2001). To a large extent, the increase in wind speed tends to increase the evapotranspiration rate (Valipour, 2015).

When air advances through a surface area, water vapor is transported at the tempo parallel to the product of the wind speed and water vapor content (Monteith, 1965). This transport is coined advective flow, which exists throughout the atmosphere. When air advances through a dry to an irrigated land, the amount of water vapor expands to a higher value, Figure 4. As reported by McMahon *et al.*, (2013) the evaporation rate inclines to a higher value over irrigated land as compared to the dryland. This is because the overpassing air over the dryland will be drier and hotter, thus enhancing the amount of available heat energy in irrigated land (Morton 1983 cited by, McMahon *et al.*, 2013)

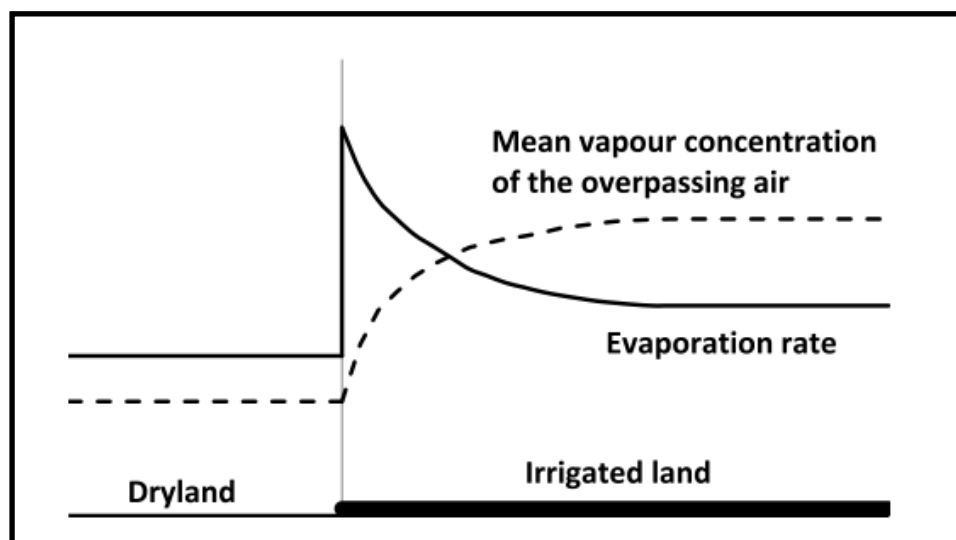


Figure 4: Representation of the role of advective air over irrigated and dry land (McMahon *et al.*, 2013)

Physical characteristics of plants are of paramount importance in the evapotranspiration process. Allen *et al.*, (1998) denotes these plant characteristics as leaf shape, crop height, leaf albedo and growth stage. When quantifying evapotranspiration in crop fields a variety of parameters such as; the crop type, the development stage and variety should be taken into consideration (Brown, 2000 and Courault *et al.*, 2003). The plant's stage of development, density and size regulate evapotranspiration to some extent (Richard G. Allen *et al.*, 1998; Dye, 2013). Large plants and regions with thick plant canopies tend increase the rate of evapotranspiration whereas small-scale plants in regions with sparse plant canopies tend to decrease evapotranspiration (Brown, 2000 and Pearlmutter *et al.*, 2008). The differences in resistance to crop height, transpiration, reflection, crop roughness, crop rooting characteristics, ground cover will produce variability in evapotranspiration levels for different crops under the same environmental conditions (Stephenson, 1998; Brown, 2000; Courault *et al.*, 2003).

Finally, environmental factors such as substandard land fertility, soil salinity, restricted application of fertilizers, the existence of hard soil horizons, substandard soil management, and the presence of pests and disease may restrict the crop development and to a large extent minimize evapotranspiration (Allen *et al.*, 1998). Another factor which needs to be considered in the evapotranspiration process is the soil characteristics which include parameters such as albedo, heat capacity and the soil chemistry (Allen *et al.*, 1998).

2.3 EVOLUTION AND ADVANCES OF REMOTE SENSING IN ENVIRONMENTAL STUDIES

The science of studying, interpreting and analysing a physical property without being in direct contact with it via the use of instruments is referred to as remote-sensing (Shaw and Burke, 2003). These analyses of a physical object are made at remote distance (Conway, 1997). Various techniques which can be applied in the field of remote sensing were highlighted in the work of (Conway, 1997 and Ogunode and Akombelwa, 2017) which include:

- computer-based analysis of non-visible radiation;
- manual interpretation of aerial photos; and
- non-visible radiation gathered by sensors on satellite technology.

The evolution and history of remote sensing can be characterised into eight categories, some running concurrent in time frames, and unique in terms of concept of utilization of data, technology, data characteristics and applications in science (Melesse *et al.*, 2007). These eight categories are:

- **Airborne remote sensing era:** The evolution of the airborne remote sensing era began during the first and second world war. During this era remote sensing was mainly used for mapping, military surveillance, surveying and reconnaissance.
- **Rudimentary spaceborne satellite remote sensing era:** This era began with the launch of rudimentary satellites at the late 1950s such as Explorer 1 by the United States and Sputnik 1 originating from Russia. Immediately after the launch of the latter two satellites in the late 1950s, the first meteorological satellite by the United States called the Television and Infrared Observational Satellite-1 (TIROS-1) were launched.
- **Spy satellite remote sensing era:** During this era spy satellites such as Corona were mainly used. Data was mainly gathered for military purposes was not digital and had to be stored in hard copies.
- **Meteorological satellite sensor remote sensing era:** The initial meteorological satellite sensors comprised of polar orbiting National Oceanic and Atmospheric Administration (NOAA), Advanced Very High-Resolution Radiometer (AVHRR) and geo-synchronous Geostationary Operational Environmental Satellite (GOES). This was a time period where data began to be stored in digital format and was analysed using computer software and hardware. In addition, this was an era when environmental applications and global coverage became practical.
- **Landsat era:** In 1972 the first Landsat was launched, which was equipped with two earth-viewing imagers; an 80m four spectral-band multispectral (MSS) and a return beam vidicon. In 1975 and 1978 Landsat 2 and 3 were launched respectively, both these satellites were configured simultaneously and carried the MSS (Melesse *et al.*, 2007). Landsat 4 was introduced with a new sensor called the Thematic Mapper. The Thematic Mapper improved the ground resolution and had more spectral bands (Masek *et al.*, 2001). In 1984 Landsat 5, a replica of Landsat 4 was introduced and 26 years later- 21 years beyond its 5-year life span, it's still providing quality data. Landsat 6 is a variant of Landsat 7 which was launched on the 15th of April, 1999 and failed during launch (Melesse *et al.*, 2007). Furthermore, Landsat 6 is equipped with a 15-meter panchromatic band (Masek *et al.*, 2001). **Table 2** gives a synopsis of the various Landsat satellites. The Landsat era provides equally good satellite data as sun-synchronous land satellites such as Indian Remote Sensing Satellite (IRS) and Systeme pour l'Observation (SPOT) of France. These satellites have global coverage and have a high resolution (nominal 2.5-80 meter). This is the most significant era that

introduced the application of environmental applications of remote sensing globally and locally.

- **Earth Observing system era:** The launch of the Terra satellite in 1999 introduced the era of the Earth Observing System. This era has introduced frequent global coverage with high level processing. The data can be accessed by researchers at no cost. The active spaceborne using radar become dominant during this era with the launch of the Japanese Earth Resources Satellite (JERS), European Radar Satellite (ERS), Advanced Land Observation Satellite (ALOS) and Radarsat. On the other hand, the Shuttle Radar Technology Mission (SRTM) was mainly utilised for digital elevation.
- **New Millennium era:** This era focuses on cutting edge satellites which were launched in a parallel time period as the Earth Observing System era, but the ideas and concepts are completely different. The new Millennium era basically focuses on future generation, sensors and satellites, which include the Earth Observing-1 conveying the initial spaceborne hyperspectral data.
- **Private industry era:** This era consists of an array of innovations. Firstly, the possibility of data being collected at very high resolutions (<10 meter). An example of a sensor that collects such high-resolution data is a Quickbird satellite. Secondly a whole new dynamic approach of collecting data, represented by the Rapideye satellite, having a daily coverage of the Earth in 5 spectral bands at a 6.5-meter resolution. Thirdly, the launch of micro-satellites which are designed by the survey satellite technology Ltd. Lastly is the introduction of Google Earth providing data access of the world and therefore making it user friendly for non-specialists to pan and zoom remote sensing data (Melesse *et al.*, 2007).

Table 1: Summary of various satellite imaging systems

Sensor	Spatial resolution	Spectral bands	Satellite revisit
1. Coarse Resolution Sensors	(meters)	(#)	(days)
AVHRR	1000m	4	daily
MODIS	250, 500, 1000m	36/37	daily
2. Multi Spectral Sensors			
Landsat 1-3	56×79m	4	16 days
Landsat 4-5 TM	30m	7	16 days
Landsat-7 ETM+	30m	8	16 days
ASTER	15, 30, 90m	15	16 days
ALI	30m	10	16 days
Spot-1 -2 -3 -4	2.5-2m	15	3-5
IRS-1C	23.5m	15	16
IRS-P6-A WIFS	56	4	16
CBERS -2 -3B -3 -4	20 m pan 20 m MS 5 m pan 20 m MS	11	
3. Hyper-Spectral Sensor			
Hyperion	30m	196	16
4. Hyper-Spatial Sensor			
IKONOS	1-4m	4	5

Sensor	Spatial resolution	Spectral bands	Satellite revisit
QUICKBIRD	0.61-2.44m	4	5
RESOURCESAT	5.8m	3	24
RAPID EYE	6.5m	5	1-2
WORLDVIEW	0.55m	1	1.7-5.9
FORMOSAT-2	2-8m	5	daily
KOMPSAT-2	1-4m	5	3-28

Remote sensing enables researchers and individuals to observe the Earth, but it also leads to the possibility of acquiring spatiotemporal variability measurements of the Earth's properties (Mucina *et al.*, 2006). The ultimate goal of remote sensing in the discipline of hydrology is to unfold approaches used measure hydrometeorological fluxes and states (Schmugge *et al.*, 2002). The primary variables include:

- Near-surface soil moisture;
- Water equivalent/snow cover;
- Land use and vegetation cover;
- Land surface temperature; and
- Water quality.

On the other hand, the hydrometeorological fluxes consists of snowmelt runoff, plant transpiration and soil evaporation which is coined evapotranspiration (Schmugge *et al.*, 2002). Although many researchers aim to quantify evapotranspiration measurements for agronomical and hydrological applications, it is often a difficult task to quantify these fluxes which require expensive instruments (Melesse *et al.*, 2007). A cheaper hydrological modelling approach can be used as an alternative where the modelling depends on the water balance-based algorithms (Allen *et al.*, 1998; Senay *et al.*, 2007) and on the energy balance algorithm (Allen *et al.*, 2005; Bastiaanssen *et al.*, 1998b; Senay *et al.*, 2007). This thesis employs an energy balance modelling approach therefore a detailed overview of the modelling approach will only be limited to the surface energy balance algorithm.

2.4 SURFACE ENERGY BUDGET AND SURFACE ENERGY BALANCE MODELS

The Earth's system works like an energy balance, which means that a similar measure of energy that enters the Earth's system leaves the system (Liou and Kar, 2012). Due to this phenomenon, the temperature of the entire system remains uniform over an extended period of time. However, variations in spatiotemporal measurements of temperature remain evident within the Earth's system. A portion of these changes are caused by various surface conditions, such as whether the surface is covered by ice or whether the surface is water or land (Liou and Kar, 2012). Such discrepancies lead to variations in the surface energy balance.

The surface energy balance equation at the land-air interface, which is based on radiative fluxes and turbulent, is described in Equation 1 (Roerink *et al.*, 2000). The incoming solar radiation is used for (Paul and Aiken, 2013):

- Warming up the soil and is represented by the soil heat flux (G);
- Warming up the surface environment and is represented by the sensible heat flux (H); and
- Vaporizing water from soil/crop surfaces which is represented by (LE) and transforming water into vapor.

The net radiation equation can be written as (Hadjimitsis and Papadavid, 2011):

$$R_n = G + H + LE \quad (1)$$

where G represents the soil heat flux ($W.m^{-2}$), H indicates sensible heat flux ($W.m^{-2}$), and LE (L indicates the latent heat of vapourization whereas E symbolizes the actual evapotranspiration) indicates the latent heat flux ($W.m^{-2}$).

The sum of the aforementioned parameters equals the net solar radiation. The net radiation can be determined from the residual between the incoming solar radiation ($R_s \downarrow$) and outgoing shortwave solar radiation ($R_s \uparrow$), and the difference between the downwelling atmospheric ($R_s \downarrow$), and emissivity of the surface as well as the reflected long wave radiation ($R_L \uparrow$) (Majozi *et al.*, 2017). The radiation balance considers the net radiation as the balance between the incoming and outgoing radiation under a stable atmosphere, **Error! Reference source not found.** (Allen *et al.*, 1998):

$$R_n = R_s \downarrow + R_s \uparrow + R_L \downarrow - R_L \uparrow \quad (2)$$

where R_n is considered to be the net radiation ($W.m^{-2}$), $R_s \downarrow$ is regarded as the incoming short-wave radiation ($W.m^{-2}$), and $R_s \uparrow$ is seen as the outgoing short-wave radiation ($W.m^{-2}$), while $R_L \downarrow$ is considered as incoming long-wave radiation ($W.m^{-2}$), and $R_L \uparrow$ indicates the outgoing long-wave radiation ($W.m^{-2}$). The net short-wave radiation is given as follows:

$$\Sigma R_s = (1 - \alpha)R_s \downarrow = (1 - \alpha) \cdot (S_c \times \cos\theta \times d_r \times T_a) \quad (3)$$

where the surface albedo is symbolized by α , solar constant is represented by S_c in ($W.m^{-2}$), and the solar incident angle is symbolized by θ , while the distance between the sun and the Earth is represented by d_r , and transmissivity of the atmosphere is indicated by T_a .

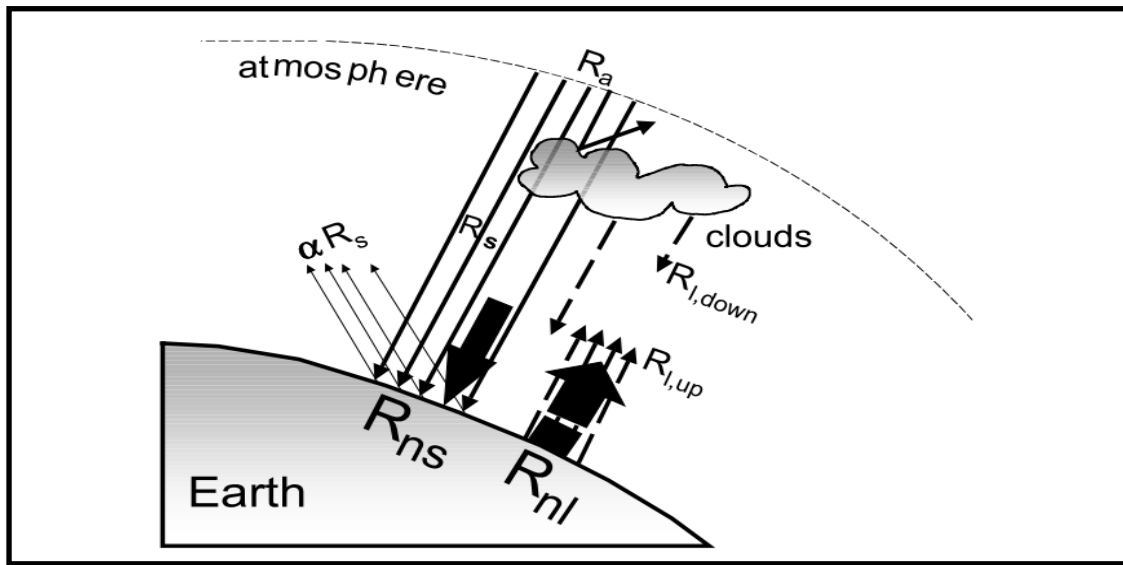


Figure 5: Representation of the net radiation components

The incoming long-wave radiation is the thermal radiation flux moving towards the Earth's surface from the atmosphere (Mölg *et al.*, 2009). The emissivity of the air can be quantified as a function of pressure, water vapor and temperature on cloud free days:

$$R_L \downarrow = e_{sky} \times \sigma \times T_a^4 \quad (4)$$

where e_{sky} represents the emissivity of the air, σ represents the Stefan-Boltzmann constant ($W.m^{-2}.K^{-4}$), and T_a represents the air temperature (K). The outgoing long-wave radiation is formulated by the use of the Stefan-Boltzmann equation as:

$$R_L \uparrow = \epsilon_0 \times \sigma \times T_s^4 \quad (5)$$

where the surface emissivity is represented by ϵ_0 and the surface temperature (K) is indicated by T_s .

The sensible heat flux (H) which is a product of the net solar radiation equation is explained as the rate of heat loss to the air by conduction and convection due to the difference in temperature (Trezza, 2002). The importance of sensible heat in evapotranspiration is the relationship between sensible heat and temperature, since sensible heat flux content is dependent on temperature. A decline in sensible heat flux causes a decline in surface temperature (McJannet et al., 2011). The sensible heat flux equation can be given as:

$$H = \rho_{air} C_p \frac{dT}{r_{ah}} \quad (6)$$

Where ρ_{air} symbolizes the density of the air (kg.m^{-3}), C_p indicates the specific air heat, while dT refers to the variation between the air temperature and the aerodynamic temperature of the near surface, ($dT = T_a - T_s$), and r_{ah} represents the aerodynamic resistance (Sun *et al.*, 2011). The aerodynamic resistance is explained as a narrow layer of non-turbulent air (about 1 to 3 mm thick) close to the surface (McMahon et al., 2013). This resistance is termed as atmospheric or aerodynamic resistance.

The latent heat flux which is a component of the net solar radiation equation, is explained as the loss of latent heat from the surface due to evapotranspiration (Bastiaanssen et al., 2005; Paul and Aiken, 2013). The latent heat originates from equation 1 and can be written as follows:

$$LE = R_n - G - H \quad (7)$$

A detailed understanding of the latent heat flux, sensible heat and soil moisture content is of paramount importance in various environmental applications such as; plant growth and productivity, cultivation and irrigation management scheduling, (Liou and Kar, 2014). Satellite radiances are metamorphosed by remote sensing energy balance algorithms into land surface features such as leaf area index, albedo, surface roughness, vegetation indices, surface temperature and surface emissivity to determine evapotranspiration as a residual of the energy balance algorithm, Equation 7 (Gowda et al., 2007).

2.5 SURFACE ENERGY BALANCE MODELS

2.5.1 SURFACE ENERGY BALANCE INDEX (SEBI)

This method of deriving evapotranspiration from an evaporation fraction was developed by, Menetti and Choudhury, (1993) and is based on the crop water stress index (Jackson *et al.*, 1981). In this method, relative evaporation is acquired by enlarging or diminishing a surface temperature that lies within the maximum range of temperature. This is indicated by high peaks in the surface energy balance denoting a theoretical lower and upper bound on the surface and air temperature variation (Liou and Kumar Kar, 2014). In this approach air temperature is considered to be zero under dry-condition due to the restricted availability of water for a specific set of boundary layer characteristics. This is done in order to enable the latent heat flux density to take its maximum value $T_{s,max}$ (maximum surface temperature). $T_{s,max}$ which is represented in Equation 8 and is adopted from the bulk transfer equation is given as:

$$T_{s,max} = \langle T \rangle_{pbl} + r_{a,max} \left(\frac{H}{\rho C_p} \right) \quad (8)$$

where the average boundary layer temperature (K) is symbolized by $\langle T \rangle_{pbl}$ (Van den Hurk Hurk, 2001). While the maximum aerodynamic resistance to sensible heat transfer (s/m) is represented by $r_{a,max}$.

Equation 9 determines the wet region minimum surface temperature by quantifying reference evapotranspiration through the use of the Penman-Monteith equation which considers no internal resistance:

$$T_{s,min} = \langle T \rangle_{pbl} + \frac{r_{a,min} (R_n - G) \frac{e_{sat} - e}{\gamma}}{\rho C_p \left(1 + \frac{\Delta}{\gamma} \right)} \quad (9)$$

where the minimum aerodynamic resistance in s/m is indicated by $r_{a,min}$ and e and e_{sat} represents actual and saturation vapor pressure, respectively. While the slope of the saturation vapor pressure as a function of T_a is measured in K·Pa/°C is represented by Δ . The psychrometric constant which is measured in K·Pa/°C is bestowed as γ . Incorporating the extreme and minimum surface temperatures with the observed surface temperature, can enable the quantification of evaporation fraction by the use of the following equation:

$$\frac{LE}{LE_p} = 1 - \frac{\Delta T \times r_a^{-1} - \Delta T_{min} \times r_{a,min}^{-1}}{\Delta T_{max} \times r_{a,max}^{-1} - \Delta T_{min} \times r_{a,min}^{-1}}$$

(10)

where $\Delta T = T_s - T_{pbl}$, $\Delta T_{min} = T_{s,min} - T_{pbl}$, and $\Delta T_{max} = T_{s,max} - T_{pbl}$ (Van den Hurk, 2001). The surface temperature (T_s) is calculated through the use of the image data situated in the thermal region of each pixel. The potential air temperature at the top of the Planetary Boundary layer or at a higher altitude is represented by T_{pbl} . Through the modification of the crop water stress index, Choudhury and Menenti (1993) managed to redefine the pixel-wise ranges theoretically for T_s and LE to record the surface variability of evaporation caused by aerodynamic roughness and albedo.

2.5.2 SURFACE ENERGY BALANCE SYSTEM (SEBS)

Another popular surface energy balance model is the Surface Energy Balance System (SEBS). This model was developed by Su, (2002) to determine surface evaporation fraction and turbulent fluxes from satellite imaging systems computing data in the visible, near infrared, and thermal infrared range, with the use of ancillary meteorological data. The SEBS algorithm requires three categories of data information (Shoko et al., 2015; Su, 2002):

1. **Remotely sensed data:** The remote sensing data consists of emissivity, surface albedo, leaf area index, fractional vegetation and roughness height
2. **Solar radiation:** This refers to downward longwave radiation and downward solar radiation, which can be quantified directly or as a model output
3. **Meteorological data at a reference height:** This category include temperature, air pressure, humidity and wind speed variables

SEBS determines the evaporative fraction from an energy balance, by measuring the roughness length needed for heat transfer, and by measuring the physical parameters at restricting (Choudhury, 1989). In this model, the dry limit value is considered to be zero for the latent heat flux, which implies that the sensible heat flux reaches its maximum value, for example $H_{dry} = R_n - G$. On the contrary, evapotranspiration takes place at the wet limit, the evapotranspiration occurs at a potential rate (LE_{wet}) whilst the sensible heat flux keeps its minimum value of, H_{wet} . The sensible heat flux at the dry and wet limits are represented in equation 11 and 12 as:

$$H_{dry} = R_n - G \tag{11}$$

$$H_{wet} = R_n - G - LE_{wet} \tag{12}$$

where the r_a heavily relies on the on the Obukhov length, which on the contrary is a function of the sensible heat flux and the friction velocity. The Obukhov length is expressed in equation 13 (Parlange and Katul, 1995; Su, 2002; Gibson, 2013):

$$L = -\frac{\rho C_p u_*^3 \theta_v}{KgH} \quad (13)$$

where ρ is the density of the air, C_p is the specific heat at a constant temperature, u_* is the frictional velocity, K is the von Karman's constant which is the value of 0.4, g is the acceleration caused by gravity, H is the specific sensible heat flux and θ_v is defined as the potential virtual temperature close to the surface. The evaporative fraction (EF) and relative evaporative fraction (EF_r) can be given as:

$$EF = \frac{EF_r \times LE_{wet}}{R_n - G} \quad (13)$$

$$EF = \frac{EF_r \times LE_{wet}}{R_n - G} \quad (14)$$

The SEBS makes use of ground-based meteorological measurements and land parameters derived from remote sensing data as its inputs. Jia *et al.*, (2013) proposed a redefined model of SEBS and used the large aperture Scintillometers to validate the estimated sensible heat flux. According to Su *et al.*, (2003), the accuracy of SEBS in estimating evapotranspiration is close to a margin of 10%-15% as compared to in-situ measurements. Like any other model SEBS has various advantages which include:

1. The energy balanced is considered at the limiting cases, restricting issues which reduce the uncertainty involved in meteorological variables and surface temperature.
2. Instead of using the same values, modern formulation of the roughness height for heat transfer can be attained.
3. Actual turbulent heat flux can be characterised without being knowledgeable of the subject.
4. The parameters linked with the surface resistance are represented

SEBS has been extensively applied with MODIS data products and thermal bands over large spatially distributed heterogeneous areas in Southern Africa (Gibson, 2013; Shoko *et al.*,

2015). The complicated solution of the turbulent heat fluxes and the numerous parameters required by the SEBS model makes it inconsistent especially when the data is not available (Liou and Kar, 2014). The validation of this algorithm was done under three different land cover types which include: grasslands, agricultural and forested sites. The algorithm can be used to estimate turbulent fluxes at different spatial scales with a high degree of accuracy (Su, 2002).

2.5.3 **SIMPLIFIED SURFACE ENERGY BALANCE INDEX (S-SEBI)**

The Simplified Surface Energy Balance Index is a new method which originates from SEBI. This method ascertains a reflectance dependent minimum temperature for wet conditions and a reflectance dependent maximum temperature for dry conditions, after which the latent and sensible heat flux are subdivided following the actual surface temperature (Roerink *et al.*, 2000). In addition, S-SEBI needs spectral radiances scanned under clear skies in the spectral range of the visible, near-infrared and thermal band. This will determine remote sensing parameters such as: surface temperature, vegetation index and surface albedo (Roerink *et al.*, 2000).

Given that the air temperature and global radiation is stable, a physical description to the observed surface temperature and albedo in the S-SEBI method can be bestowed (Roerink *et al.*, 2000). This is achieved when surface features within the observed image varies between dry/bright pixels and dark/wet pixels. At low surface albedo, the surface temperature which describes the partitioning of the residual energy into latent and sensible heat (Kustas and Norman, 1996) will remain more or less constant with an increase in reflectance, Figure 6. This is due to the prevalence of adequate water supply from saturated surfaces like irrigated land and open water (Roerink *et al.*, 2000 and Liou and Kar, 2014). However, higher reflectance will result in an increase of surface temperature to an unknown value. The latter phenomena is then termed “evaporation controlled” because an alteration in temperature at this point is vastly influenced by a decline in evapotranspiration as a result of inadequate availability of moisture in the soil, Figure 6 (Li *et al.*, 2009). Therefore, the accessible energy is used solely for surface heating. Consequently, a rise in surface reflectance produces a decrease in net radiation as a result decreasing the available energy. This process results in a decline in surface temperature with an increase in surface reflectance, Figure 6. This phenomenon is then termed “radiation controlled” (Roerink *et al.*, 2000; Li *et al.*, 2009, Liou and Kar, 2014).

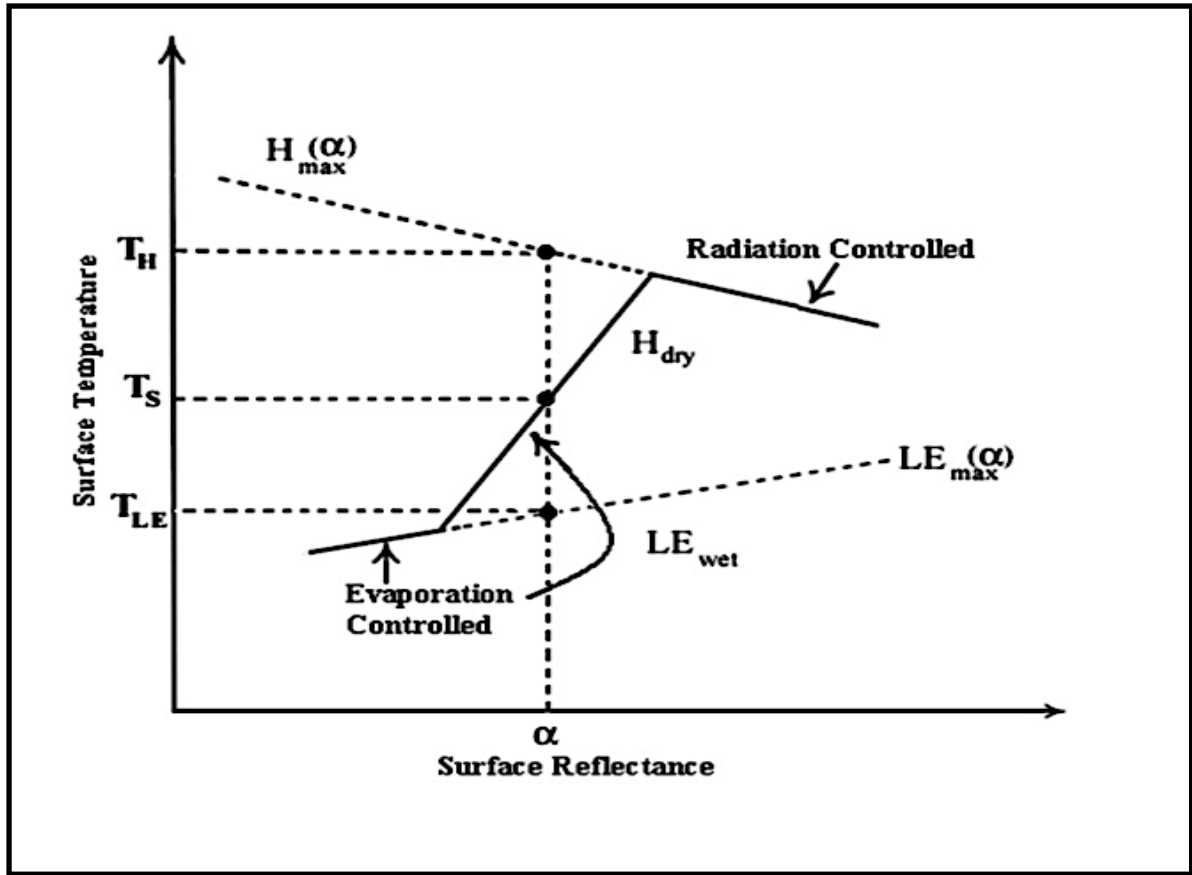


Figure 6: Schematic relationship between surface reflectance and surface temperature in the S-SEBI algorithm (Roerink *et al.*, 2009; Li *et al.*, 2009 and Liou and Kar, 2014)

The S-SEBI makes use of an evaporative fraction which is derived from the wet and dry regions, and developed by combining the reflection-dependent surface temperature between the reflection-dependent minimum and maximum surface temperature (Roerink *et al.*, 2000 and Li *et al.*, 2009) as indicated in Equation 15:

$$EF = \frac{(T_H - T_S)}{(T_H - T_{LE})} \quad (15)$$

where the surface temperature T_H corresponds to dry pixels and indicates the minimum latent heat flux ($LE_{dry} = 0$) and the maximum latent heat flux which are represented by ($H_{dry} = R_n - G$). The surface temperature which corresponds to wet pixels is represented by T_{LE} , and also represents the minimum sensible heat flux ($H_{wet} = 0$) and maximum latent heat flux ($LE_{wet} = (R_n - G)$) for a given surface albedo. Through the use of the regression equation T_{LE} and T_H can be calculated as:

$$T_{LE} = C_{min} + d_{min}\alpha$$

(16)

$$T_H = C_{max} + d_{max}\alpha$$

(17)

where the scatter plot of T_s and α is used to calculate the empirical coefficients of C_{max} , d_{max} , C_{min} and d_{min} over the entire study area. In conclusion, the evaporative fraction is determined from equation (15) utilising equation (16) and (17). S-SEBI has the following advantages (Roerink *et al.*, 2000):

1. It does not require any additional meteorological data provided the availability of surface extremes on the area of interest.
2. A change in reflectance (albedo) values results in a variation of extreme temperatures of dry and wet conditions. Unlike SEBAL, a constant temperature is calculated for dry and wet conditions.

2.5.4 SURFACE ENERGY BALANCE ALGORITHM FOR LAND (SEBAL)

SEBAL was inaugurated by Bastiaanssen *et al.*, (1998) in Netherlands. SEBAL relies on a satellite imaging system computing data in the near visible (0.4 to 0.7 μm), near-infrared (0.7 to 3.0 μm) and thermal-infrared band (3 to 14 μm) such as, NOAA, Landsat, AVHRR, ASTER and MODIS (Kalma, 2008; Sun *et al.*, 2011) together with ground based ancillary weather data of humidity, wind speed, air temperature and solar radiation (Ahmad *et al.*, 2006). These two parameters (Satellite imaging system and ground based meteorological data) will enable the SEBAL model to accurately estimate spatial variations in evapotranspiration measurements (Bastiaanssen *et al.*, 1998). In addition, the principles parameters required in the SEBAL model which are indicated in Figure 7 include:

- Surface parameters (surface temperature, albedo and vegetation index);
- Land surface parameterization;
- Surface energy balance (soil heat, net radiation, latent heat and sensible heat flux); and
- Moisture indicator (Bowen ratio, Evaporation fraction and Priestley and Taylor coefficient surface resistance).

The SEBAL converts the satellite radiances into surface parameters of surface temperature, surface albedo and vegetation index, which are used to deduce the surface fluxes used in quantifying the rate of evapotranspiration on different land cover types (Bastiaanssen, 1995; Bastiaanssen *et al.*, 1998; Bastiaanssen *et al.*, 2005). The main surface flux which is then

used to determine the rate of evapotranspiration as a residual of the energy balance is latent heat flux, Equation, 7 (Tsouni et al., 2008). This is calculated using latent heat flux because satellites do not measure near surface vapor flux or vapor content (Allen *et al.*, 2005).

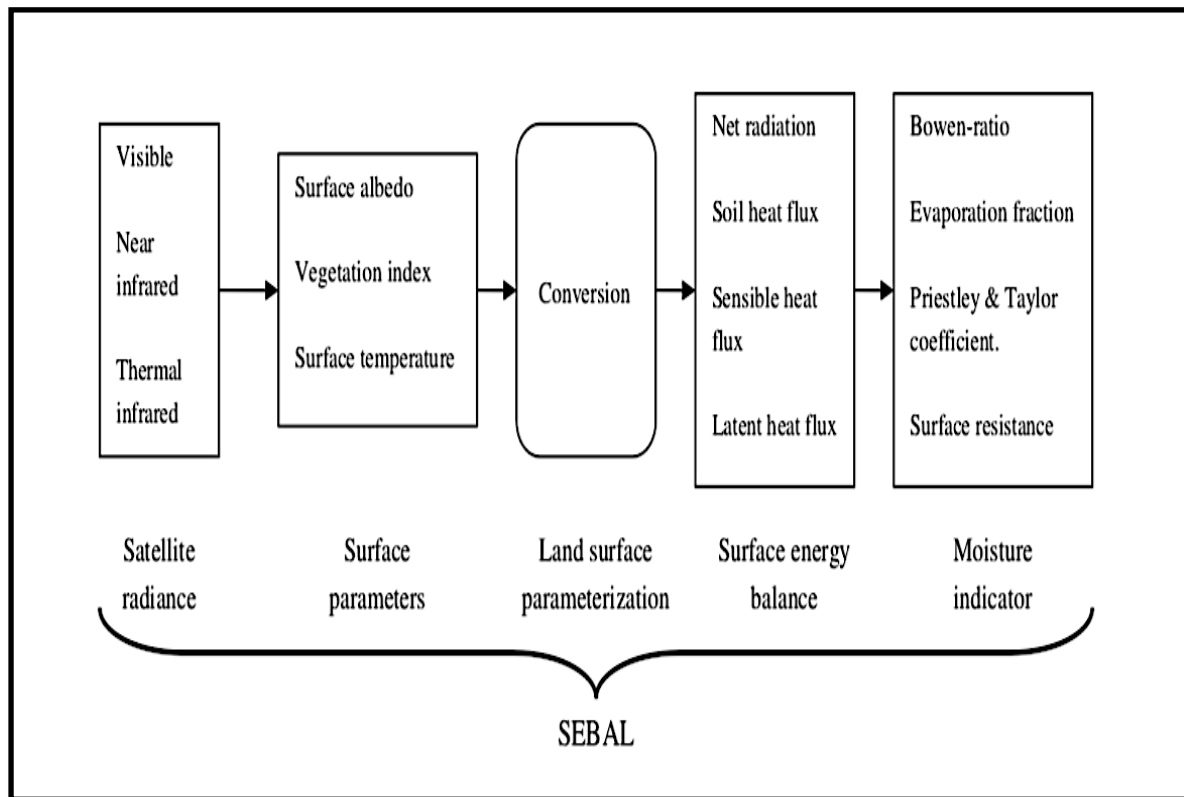


Figure 7: The primary components required in a SEBAL model (Bastiaanssen, 1998)

SEBAL is a commonly used model which has been validated under different environmental conditions and in various countries including; Italy, Spain, Turkey, Pakistan, Sri Lanka, Niger, United States and China (Bastiaanssen, 1998, 2000, 2005). With a level of accuracy being 85% at a field scale and 95% at seasonal and daily scale in more than 30 locations globally (Bastiaanssen *et al.*, 1998, 2000).

The SEBAL was formulated to determine the parameters of the surface energy balance with minimum ground meteorological data for both regional and local scales (Bastiaanssen, 2000). This model is based on a combination of both physical parameterization and an empirical relationship. The latent heat flux is determined as a residual of the surface energy balance equation on a pixel by pixel basis and evapotranspiration is determined by instantaneous latent heat flux (Kiptala *et al.*, 2013). The balance between the short and long wave radiation is used to compute the Net radiation (R_n). However, the soil heat flux is determined through the use of the equation found in the work of Bastiaanssen *et al.*, (1998, 2000). This equation

can be used for most types soil cover and vegetation. Proper quantification of the sensible heat flux (H) is of cardinal importance in order to retrieve the components that will be used to measure the rate of evapotranspiration as a residual from the energy balance (Liou *et al.*, 2014).

SEBAL makes use of two reference air temperatures (Beljaars and Holtslag, 1991 cited by, Bastiaanssen *et al.*, 2005). Mkwanzani, (2014) states that the one air temperature is located at height h_1 (0.1m) near the surface, and at a higher altitude h_2 (2m). In order to calculate the value associated with the surface temperature (dT) for each pixel. SEBAL acknowledges the occurrence of a linear relationship between the radiometric surface temperature (T_s) and the near-surface temperature (dT) by considering the surface and homogeneous metrological conditions:

$$dT = cT_s + d \tag{18}$$

where c and d are considered as empirical coefficients acquired from an anchor points (wet and dry) for a specific satellite image (Bastiaanssen *et al.*, 1995). The anchor points in the satellite image portray conditions of intensive evaporative behavior, these anchor points are manually selected on the satellite image by the user (Bastiaanssen *et al.*, 2005). According to Mkwanzani *et al.*, (2015) evaporation is predicted to be absorbing most of the accessible energy ($R_n - G$) at a “cold (wet)” pixel which means that the near-surface temperature and sensible heat flux (H) are both zero ($dT_{wet} = 0$). While at a “hot (dry)” pixel the evaporation is expected to be zero and all the accessible energy is converted into sensible heat (Sun *et al.*, 2011). The hot pixel is a dry uncovered agricultural land where the latent heat fluxes are given as 0, while the cold pixel have the lowest surface temperature values and they are often located on well irrigated land or open water bodies (Bastiaanssen *et al.*, 2005). Both these pixels allow the possibility of calculating the remaining pixels which lie within this raster image.

The near surface temperature (dT) is then determined through the aerodynamic theory for two extreme conditions of wet and dry as:

$$dT_{dry} = \frac{H_{dry} \times r_{a\ dry}}{\rho_{air\ dry} C_p} \tag{19}$$

where the sensible heat flux at the dry limit is indicated by H_{dry} and is equivalent to $(R_n - G)$. As soon as the surface-air temperature variations are determined at both the wet (cold) and dry (hot) pixels, coefficients “ d ” and “ c ” which are highlighted in equation 18 can be estimated with ease. Utilising these two coefficients, the surface-air temperature difference which is

represented as dT can easily be calculated at each pixel with surface temperature T_s , and by making use of equation 18. In this model the hot pixel is acquired from a pixel situated in an area that reflects high surface temperature, while the cold pixel is generally acquired from pixel situated in deep water. Locating the dry pixels is of cardinal importance in this model, while the wet pixels are generally located at areas with adequate supply of water, over a large calm surface with water.

The SEBAL model which estimates surface fluxes from thermal remotely sensed data include the following advantages:

1. The model does not require extensive auxiliary ground-based data as an input.
2. The model is incorporated with an automatic internal correction, which limits the strict correction of atmospheric effects on surface temperature.
3. Each picture analysed is internally calibrated.

Like any other remote sensing model SEBAL possess a few disadvantages:

1. Individual selection of the cold/wet and hot/dry pixels within each raster image is needed, to ascertain model parameter c and d (Long *et al.*, 2012). The resulting evapotranspiration and latent heat fluxes estimates can differ with different extreme pixels chosen by the operator, as well as the domain size and the spatial resolution of the satellite imaging system (Long *et al.*, 2011).
2. In mountainous regions, a few adjustments are needed with the use of a digital elevation model for surface temperature to consider the lapse rate (Bastiaanssen *et al.*, 2010).
3. The sensible heat fluxes are vastly influenced by errors in surface temperature measurements or differences in the surface-air temperatures.
4. Neglecting the effects associated with the viewing angle of the radiometer can result in changes in surface temperature by a few degrees for some images.

2.5.5 MAPPING EVAPOTRANSPIRATION AT HIGH RESOLUTION AND WITH INTERNALIZED CALIBRATION (METRIC)

METRIC is a version of SEBAL, which is an energy balance model developed by Bastiaanssen *et al.*, (1998) in the Netherlands. METRIC can be considered as an image-processing tool which maps out regional evapotranspiration over complex areas as a residual of the energy balance at the bottom of the atmosphere. METRIC has been modified from SEBAL, with the

inclusion of reference/potential evapotranspiration, which is measured through the use of ground-based meteorological data.

In order to internally calibrate the latent and sensible heat flux computation and rectify the boundary conditions for the energy balance, two anchor conditions need to be selected within an observed satellite image. This type of internal calibration eradicates the idea of an in-depth atmospheric correction of albedo and surface temperature measurements utilising the radiative transfer model (Tasumi et al., 2003). The internal calibration of this method is similar to that of SEBAL, as it minimizes the errors in determining surface roughness and aerodynamic stability correction. The calibration is achieved by manually selecting a cold and hot pixel to express the near-surface temperature (dT).

The advantages of METRIC are similar to that of SEBAL, but the surface slope needs to be considered. In terms of disadvantages, the model has uncertainties in determining the anchor pixels (Liou and Kar Kumar, 2014).

2.5.6 **TWO-SOURCE MODELS (TSM)**

The two source-model, which is also called the dual-source model, was developed by Norman *et al.*, (1995), to improve the accuracy of determining latent heat fluxes through the use of remotely sensed data. This model was particularly introduced to separate the complex radiometric surface temperatures into vegetation and soil components (Blyth and Dolman, 1996; Kustas and Norman, 1996). Furthermore, this method considers the latent heat and sensible heat fluxes are emitted from soil and vegetation components into the atmosphere (Wallace *et al.*, 1997 and Kabat *et al.*, 1997).

In the two-source model, satellite-derived surface temperature (T_s) is recognised as the compilation of canopy (T_{veg}) and soil temperature (T_{soil}). In addition, the latent heat and sensible heat are partitioned into vegetation and soil contributions, respectively. The canopy latent heat is quantified through the use of the Priestley-Taylor. A similar method is used to derive the canopy (T_{veg}) and soil temperature (T_{soil}), from the surface temperature derived from a satellite imaging system (Anderson *et al.*, 2008; Kustas *et al.*, 2009).

The ability of the model to make accurate emissivity estimations, atmospheric corrections and high accuracy in calibrating the sensor are amongst the main advantages of the Two-Source model. Linking the planetary boundary layer (*PBL*) with the Two-source model eradicates the need of ground-point measurements of air temperature (Kustas *et al.*, 1996), making this model ideal for regional and global scales (Anderson, 1999). A comparison of all the above mentioned remote sensing evapotranspiration models are depicted in

Table 2: Summary of remote sensing models

surface energy balance models	Input Parameters	Advantages	Disadvantages
SEBI	$\langle T \rangle_{pbl}, h_{pbl}, v, T_s, R_n, G$	Relating the effects of r_a and T_s directly on LE	Needs ground-based meteorological data
SEBS	$T_{air}, h_a, v, T_s, R_n, G$	Uncertainty in meteorological parameters and surface temperature can be solved easily. Roughness height for heat transfer is determined instead of utilising coefficients.	Needs a lot of parameters. The model possesses difficulties in attaining turbulent fluxes
S-SEBI	T_s, a_s, R_n, G	Does not need ground-based data	Extreme temperature is influenced by the location
SEBAL	v, h_a, VI, R_n, G	Needs sufficient ground-based measurements. The model has internal calibration. Atmospheric correction is not a necessity	Used over plain terrains. Possess error in determining anchor pixels
METRIC	v, h_a, VI, R_n, G	Identical to SEBAL, however the surface aspect and slope have to be highlighted	Possess error in determining anchor pixels
TSM	$v, h_a, T_{air}, T_s, T_c, F_r,$ or LAI, R_n, G	Incorporated with view geometry. The model reduces the need of empirical corrections for the "excess resistance".	Many components and ground measurements are needed

2.6 APPLICATION OF SEBAL WITH LANDSAT 7

The Landsat mission has successfully produced highly calibrated data for over 38 years of the Earth's surface which is available to a broad spectrum of users including global change researchers, agribusiness, state and local governments, academia, military and commercial users (Aeronautics, 1972). The data is pivotal in monitoring the Earth's terrestrial forests, agricultural activity, grasslands, surface hydrology and urban growth. Landsat has a primary objective of providing continuous high-quality multispectral data of the Earth's surface. In 1972 the first Landsat was launched, which was equipped with two Earth-viewing imagers; an 80m four spectral-band, multispectral scanner (MSS) and a return beam vidicon (Masek et al., 2001).

In 1975 and 1978 Landsat 2 and 3 were launched respectively, both these satellites were configured simultaneously. Landsat 4 was introduced with a new sensor called the Thematic Mapper. The Thematic Mapper improved the ground resolution and had more spectral bands (Masek et al., 2001). In 1984 Landsat 5, a replica of Landsat 4 was introduced and 26 years later- 21 years beyond its 5-year life span, it's still supplying quality data. Landsat 6 which was launched in 1993, went missing immediately after launch. Landsat 6 is a variant of Landsat 7 which was launched on the 15th of April, 1999. Furthermore, Landsat 6 is equipped with a 15-meter panchromatic band (Masek et al., 2001).

Table 3: The various Landsat satellites, sensors, bandwidths and spatial resolution

Satellite	Sensor	Bandwidths	Resolution
Landsat 1-2	RBV (1-3) Mss (4-7)	(1) 0.48-0.57 μm	80m
		(2) 0.58-0.68 μm	80m
		(3) 0.70-0.83 μm	80m
		(4) 0.5-0.6 μm	79m
		(5) 0.6-0.7 μm	79m
		(6) 0.7-0.8 μm	79m
		(7) 0.8-1.1 μm	79m
Landsat 3	RBV (1) Mss (4-8)	(1) 0.505-0.75 μm	40m
		(4) 0.5-0.6 μm	79m
		(5) 0.6-0.7 μm	79m
		(6) 0.7-0.8 μm	79m
		(7) 0.8-1.1 μm	79m
		(8) 10.4-12.6 μm	240m

Satellite	Sensor	Bandwidths	Resolution
Landsat 4-5	Mss (4-7)	(4) 0.5-0.6 μm	82m
		(5) 0.6-0.7 μm	82m
	TM (1-7)	(6) 0.7-0.8 μm	82m
		(7) 0.8-1.1 μm	82m
		(1) 0.45-0.52 μm	30m
		(2) 0.52-0.60 μm	30m
		(3) 0.63-0.69 μm	30m
		(4) 0.78-0.90 μm	30m
		(5) 1.55-1.75 μm	30m
		(6) 10.4-12.5 μm	120m
(7) 2.08-2.35 μm	30m		
Landsat 7	+ETM (1-8)	(1) 0.45-0.52 μm (Blue)	30m
		(2) 0.52-0.60 μm (Green)	30m
		(3) 0.63-0.69 μm (Red)	30m
		(4) 0.76-0.90 μm (Near Infrared)	30m
		(5) 1.55-1.75 μm (Short-wave Infrared. 1)	60m
		(6) 10.4-12.5 μm (Thermal)	30m
		(7) 2.08-2.35 μm (Short-wave Infrared. 2)	15m
		(8) PAN 0.50-0.90 μm	

NASA is accountable for the launch and the development of Landsat 7. However, the United States Geological Survey (USGS) is more accountable for the maintenance and development of the satellite (Aeronautics, 1972). In this capacity the USGS is responsible for processing and dispensing the data. Furthermore, the USGS is responsible for maintaining the data archive of Landsat 7. The overall goals which were set out for Landsat 7 mission include:

1. Provision of continuous data of Landsat 4 and 5;
2. Provision of data coverage at a repeat cycle of 16-days; and
3. Construct and provide cloud-free, sun-lit, land images.

The Landsat 7 satellite, maps out the Earth on a 16-day repeat cycle. Furthermore, the satellite is equipped with a sensor called the Enhanced Thematic Mapper (ETM+) which was designed

by Raytheon Santa Barbara Remote Sensing (SBRS). According to Wubet, (2003) the Landsat 7 bands can be categorised as visible (band 1-4), near infrared (4,5 and 7), shortwave infrared (5 and 7), thermal infrared (band 6) and Panchromatic (band 8)

The ETM+ sensor is a derivative of the Thematic Mapper which, was initially designed for Landsat 4 and 5, but is similar to the Enhanced Thematic Mapper (Melesse et al., 2007). The difference between TM+ and ETM+ is the addition of two gain ranges and the panchromatic band. Furthermore, ETM+ was equipped with two additional solar calibrators and the resolution of ETM+ was significantly improved. Landsat 7 utilizes the same standard worldwide reference system (WRS) that was used by Landsat 4 and 5. The WRS indexes/computes scene centers (rows) and orbits (paths) into a global system consisting of 233 paths and 248 rows (Aeronautics, 1972).

The SEBAL model can be applied to Landsat satellite images. In the study of Sun *et al.*, (2011), the SEBAL model along with Landsat 7 images were used to map out daily evapotranspiration in China. The spatial variations of daily actual evapotranspiration for the study area ranged from 0 to 8mm/day and 4.87mm/day for the entire study area (Sun *et al.*, 2011).

2.7 METHODS OF ESTIMATING EVAPOTRANSPIRATION

The two common categories for estimating evapotranspiration include: water vapor transfer and water budget methods. In the water budget method outgoing water is subtracted from the incoming water and the residual water is then coined water storage capacity (Szolgay et al., 2003). If all the components of the outgoing water component are known and only evapotranspiration is unknown, then evapotranspiration can be determined (Shoko et al., 2015; Shuttleworth, 2008). The water budget category is the most user-friendly method. However, this method has its own disadvantages such the inability to deduce the alteration of ground water storage, as well as the unreliable and incorrect measurements of the outgoing water components (Senay et al., 2011).

Water vapor methods utilise meteorological sensors mounted above the ground to determine the flow of water into the atmosphere (Shuttleworth, 2008). These sensors often quantify evaporation based on the surface energy balance algorithm as a latent heat flux rather than quantifying evaporation in mass terms. The latent heat flux describes the flow of energy that is conveyed with water vapor which leaves the Earth's surface in the form of latent heat flux (Shuttleworth, 2008).

In total Shuttleworth, (2008) indicated four categories of determining evapotranspiration (water budget measurements, water vapor transfer methods, components of evaporation and large-

scale evaporation). A brief synopsis of these categories and the different instruments used in each category can be seen in Table 4

Table 4: A summary of four methods of estimating evapotranspiration

1. Water budget measurements	Brief description	Assumptions
Evaporation pan	Measures the adjustment in the water level of open water with well-defined dimensions and sitting	Predicts that the relationship between the actual evaporation from the adjacent area and evaporation measured from pans can be calibrated. In addition, calibration can be transferred between climates and locations
Water balance of basin	The unquantified difference between of the components of the basin water balance that are measured such as; groundwater and surface outflow, incoming precipitation and water storage	An assumption can be made that all components of the basin water balance can be quantified as spatial averages.
Lysimeter	Quantifies the alteration in weight of an undisturbed or isolated soil sample with overlying vegetation while concurrently determining precipitation from the soil sample	This method assumes that the sample of soil and overlying vegetation on which measurements are conducted, can be represented in terms of vegetation growth and soil water content and vigor of the field or plot in question.
Soil moisture depletion	Quantifies the alteration in water content of a given sample of uniform vegetation and soil while quantifying precipitation and run-off and determining deep drainage for the sample plot	It is assumed that soil water measuring devices (neutron probes, resistance blocks, capacitance, tensiometers and time-domain reflectometers) adequately quantifies the change in soil water. The effects of sensor placement and deep roots are small, making it easy to calculate deep drainage.
2. Water vapor transfer methods	Brief description	Assumptions
Bowen Ration- Energy budget method	Determines evaporation in the form of latent heat from the surface energy budget utilising the ratio of sensible to latent heat, deduced from the ratio between humidity gradients and atmospheric temperature determined a few meters above the vegetation	In the lower atmosphere, where conditions are stable it is assumed that the turbulent diffusion coefficient for latent heat and sensible heat are identical. The plot-scale measurements of energy budget components represent upwind conditions.
Eddy correlation/ Eddy covariance method	Quantifies evaporation in 20 to 60 minute time intervals, as a result of the correlation coefficient between	Turbulent transfer of water vapor is assumed to occurring only at a sample point.

	atmospheric humidity and vertical windspeed	
3. Components of evaporation	Brief description	Assumptions
Transpiration measurement by porometry or monitoring sap flow	<p><u>Porometry</u>: quantified from an increase in humidity in a chamber temporarily enclosing leaves that are transpiring.</p> <p><u>Sap Flow</u>: The sap flow is determined from the rate of sap flow in the branches, trunk or roots utilising heat as a tracer.</p>	<p><u>Porometry</u>: It is assumed that the enclosure of shoots and leaves within the chamber does alter the transpiration rate.</p> <p><u>Sap flow</u>: It is assumed that the installation of sensors does not change the sap flow rate.</p>
Rainfall interception loss from tall vegetation	Determined as the difference between cumulative rainfall below/above tall canopy. This method requires accurate below-canopy sampling with troughs/gauges that sample at a spatial scale of a canopy.	Below-canopy sampling is assumed to be adequate. It is often difficult to take measurements within a 1-2 week's time interval.
Soil evaporation	A shallow, small-scale implementation of soil moisture or lysimetry depletion methods.	All the small soil-samples are assumed to be a representative of the entire soil surface, irrespective of their below canopy cover.
4. Large-scale evaporation	Brief description	Assumptions
Scintillometer measurements	This method utilizes theoretical relationship between latent and sensible heat fluxes and atmospheric scintillation channeled into a beam of electromagnetic radiation between a detector and a source by humidity and temperature fluctuations.	This method is limited to an ideal turbulent field close to the Earth's surface, possessing a uniform aerodynamic roughness.
Remote sensing estimates	The surface energy balance is utilised to indirectly calculate evaporation, with the sensible heat flux being determined from the difference between the temperature of the evaporating surface and air temperature.	This theory assumes that aerodynamic surface temperature can be calculated from radiometric surface temperature, or aerodynamic surface temperature is the same as radiometric surface temperature
LIDAR (Light detecting and ranging method)	The vertical gradient of water vapor at a local time average is sampled remotely utilising LIDAR. Local evaporation flux can then be calculated through the use of a similarity theory and supplementary measurements of atmospheric stability and friction velocity.	This theory assumes that the Monin-Obukov theory is applicable and the measurements of atmospheric stability and friction velocity are applicable.

3. MATERIALS AND METHODS

The meteorological and geological parameters of the validation site, as well as the location of the validation site will be highlighted in sub-section (3.1). A detailed description of the data used and the methodology applied for determining the properties of the surface energy balance and the rate of evapotranspiration is discussed in subsection (3.2).

3.1 VALIDATION SITE AND STUDY BACKGROUND

Sutherland (32° 22' 20.17" S, 20° 48' 23.05" E) is a small town situated in the Western Karoo in Northern Cape province of South Africa (Figure 8) covering a surface area of approximately 3000 Km² (Adams et al., 2001). The South African Astronomical Observatory enhances tourism in Sutherland which equally contributes to the local economy of Sutherland as sheep farming (Bradshaw *et al.*, 2000). This area was selected as the validation site firstly because Sutherland has good topographical variability. Secondly because, the ground is not fully covered with vegetation which makes it easier for the satellite to quantify the surface energy fluxes with a high degree of accuracy. Lastly, because there is good data set of ground based meteorological data which will be used to validate the remotely sensed data.

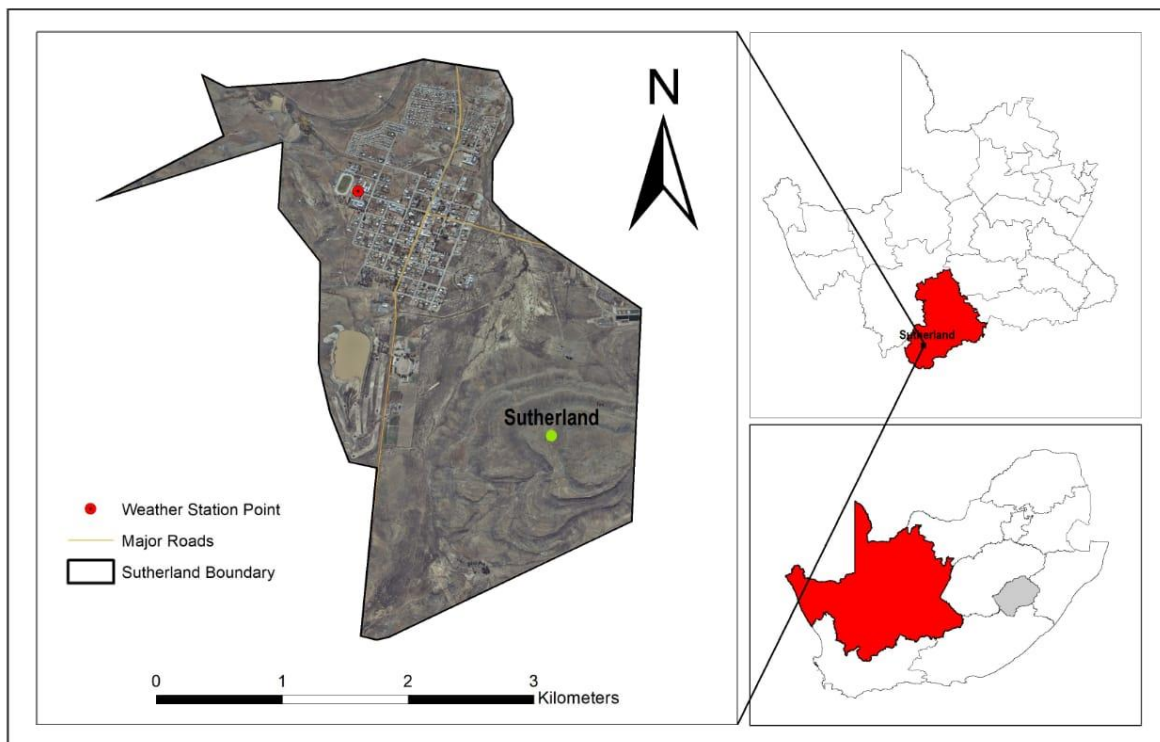


Figure 8: Locality map of Sutherland

3.1.1 **CLIMATE**

Sutherland is considered a semi-arid locale with evaporation rates exceeding the average annual rainfall, 1800-2000mm and 300-400mm respectively (Mukheirbir and Sparks, 2005). The annual rainfall in the area is highly variable, with the north-western parts of the region receiving less rainfall (100mm) as compared to the western (500mm) parts (Venter *et al.*, 1986). Moreover, Venter *et al.*, (1986) denotes that the western parts of the greater Karoo receives summer rainfall from (October-March). The annual average temperature in Sutherland is 12 degrees, with temperatures in winter dropping beyond freezing point, making Sutherland the coldest town in the country (Vey *et al.*, 2015). The annual average wind speed for Sutherland has been recorded as 10km/h which is equivalent to 5 knots.

3.1.2 **GEOLOGY AND GEOHYDROLOGY**

As reported by Visser *et al.*, (1980) the main Karoo Basin, which was filled from the early Jurassic (100 Ma) to the late Carboniferous covers a total area of 500 000 Km². In addition, the Karoo sequence in the northern region is thinner than the sequence in the western region of the basin which is, 100m and 6400m respectively. Sedimentary rocks originating from the Beaufort group relate conformably to the Eccca group within the main Karoo basin, Table 5 (Adams *et al.*, 2001).

Table 5: Stratigraphy of the Karoo Supergroup

Period	Group	Subgroup	Formation
Jurassic	Stormberg ^a		
Triassic		Tarkstad ^a	
225 Ma	Beaufort (3000 m)		
Permian		Adelaide	Teekloof
			Abrahamskraal
Permian	Ecca (1800 m)		Waterford ^b
			Koedoesberg ^b
			Kookfontein ^b
			Skoorsteenberg ^b
			Tierberg
			Whitehill (not exposed)
270 Ma-Carboniferous	Dwayka (600 m)		Not visible in the study area

a- Not found in Sutherland; b hasn't been approved

The sedimentary rocks that are prevalent in the study area are; silt stones, mudstones and shales which are affiliated with the **Beaufort group (Adelaide group)**. The width of the Abrahamskraal formation in Sutherland is reported to be 1000m (Theron, 1983). The outcrops of the Teekloof are prevalent in the Northern parts of Sutherland. The formation of the Teekloof is indistinguishable to the suppressed Abrahamskraal formation, excluding the presence of the chart layers and limestone bands (Theron, 1983). East-west trending basaltic dolerite dykes, together with sills during the Jurassic era, intruded the sediments and caused fractures in the sedimentary rocks. Throughout the Cretaceous era, the associated intrusions of the Salpeterkop Carbonatite complex and the carbonatites altered the geological formations in the study area.

South Africa is covered by approximately two-thirds of the Karoo basin. The basin evolved during the initial stages of the Carboniferous Period (Smith 1990). The evolution and formation of Carboniferous Period, was regulated by four significant geodynamic events which are indicated in the work of Woodford and Chevallier (2002) as:

- Deposition of sediments originating from the Karoo supergroup into the foreland basin during the evolution of the Cape Fold (± 250 Ma);
- The genesis of the Gondwana break-up with the extrusion of the Draakensburg basalts and the intrusion of the Karoo dolerite (± 180 Ma);
- Local positioning of fissures and kimerlite pipes with intra-plate mantle activity, along with the intrusion of major epeirogenic uplift with intensified erosion rates during the evolution of the Kalahari plateau (± 140 to Ma 80) and carbonite plus; and
- The reduction in the rate of erosion and the formation of the modern river system (± 60 Ma to present).

The salpeterkop volcanic morphology is regarded as an important local magmatic feature. Extensive carbonite intrusive are present, with pyroxene, amphibole and olivine minerals, inside the contact zone of the paleo-volcano. The Landsat Imagery system was employed by Newton (1987) to examine the fracturing network in the Salpeterkop structure. The magmatic formation has induced visible, concentric fracture patterns that dilate outwards from the middle of the Salpeterkop formation (Newton, 1987). Neotectonic stresses were examined by Viola *et al.*, (2002) and as a result ten episodes of ductile-brittle deformation were found on the west coast of South Africa, 300km from Sutherland. This has significant application for the incitement of fractures for groundwater flow in Sutherland. The landscape of Sutherland is characterised by undulating hills. The hills are composed of doleritic intrusions (Adams et al.,

2001). Furthermore. The landscape is characterised by dykes that are perpendicular to one another.

The Groundwater in the Sutherland region is drawn from the Permian mudstones and sandstones as well as the Jurassic dolerite sills and dykes (Adams *et al.*, 2001). In addition, Groundwater in this region occurs as a result of joint systems and fracture. Due to the intrusive rocks in the area (carbonatites, melilite basalts, carbonatites) and the dominant joints related to the Cape Orogeny, the formation of the area has been significantly fractured, making these formations suitable aquifers as a result of secondary permeability (Adams *et al.*, 2001). The hydraulic head measurements in Sutherland represent lower water tables in the Southern parts of Sutherland (Mahed, 2006). However, a detailed geohydrological information for Sutherland is still lacking such as detailed mineralogy, water strikes, borehole logs is still lacking.

3.1.3 VEGETATION AND BIOME

According to Rutherford *et al.*, (2006) a biome is divided into different bioregions for the type of plant that grows there. Sutherland is situated in the Rainshadow Valley Karoo Bioregion that falls under the succulent Karoo biome. The Rainshadow Valley Karoo Bioregion is the largest of the six bioregions that make up the Succulent Karoo biome. Mucina *et al.*, (2006) states that bioregions are further divided into vegetation units that show the most common plants that grow in a particular region. Sutherland is situated in the Koedesberg-Moordenaars Karoo vegetation unit.

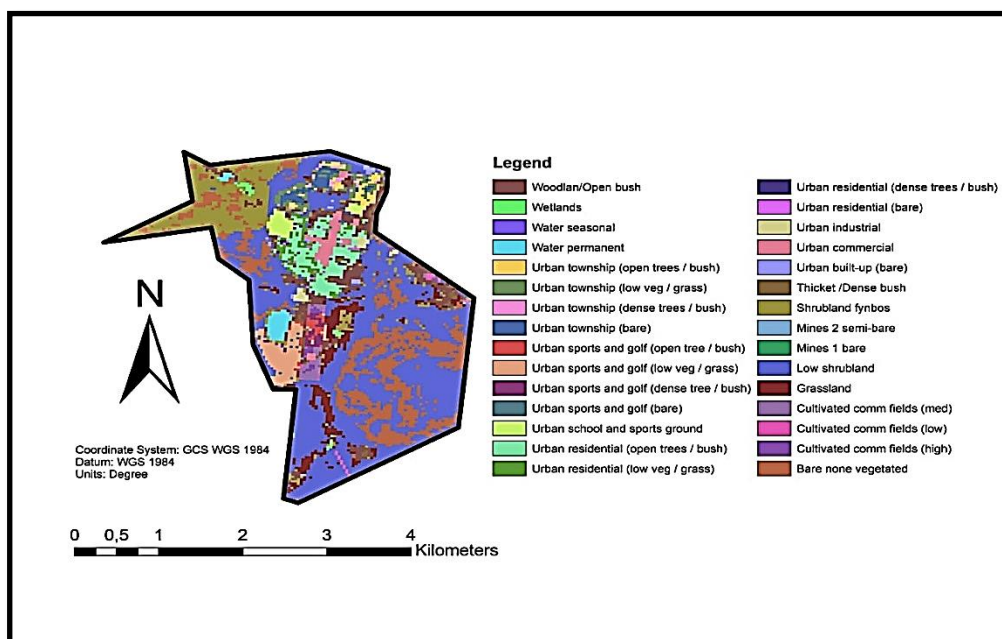


Figure 9 :Land use/cover map of Sutherland (Landsat, 2014)

The landscape features of this area include hilly to slightly uneven terrain, that is scattered with tall shrubs and dotted with low shrubs, Figure 9. There are patches of “white” grass visible on the plains and there are mainly shrubs of *Drosanthemum*, *Galenia* and *Pteronia*. It is no surprise that the most dominant plant species are succulent shrubs such as (Mucina *et al.*, 2006):

- *Hereroa odorata*;
- *Antimima fergusoniae*;
- *Aridaria noctiflora*;
- *Crassula nudicaulis*; and
- *Deilanthus peersii*.

3.2 METHODOLOGY

3.2.1 REMOTE SENSING ACQUISITION AND PREPROCESSING

The primary software being utilised for analysing and compiling data is ILWIS (Integrated Land Water Information System). ILWIS is built for Land-Water analysis and is incorporated with an exceptional GIS operation capability (Hendrikse, 2000). In addition, it is a user-friendly software with an added advantage of effortless script writing.

3.2.2 SATELLITE DATA

The Landsat ETM+7 satellites images are downloaded from EarthExplorer which is an USGS site <https://earthexplorer.usgs.gov>. Level-1 Products, which are described as high quality, geometrically and radiometrically corrected images (Aeronautics, 1972) are downloaded for Sutherland. The raw images are downloaded in a TIF format. Pre-processing such as radiometric, atmospheric and geometric corrections which is essential for analysing land cover parameters and energy fluxes were done on the satellite images. All the functions from analysing and Importing data are conducted in the GIS & RS software ILWIS. Additional data which was used in the ILWIS software include, ground-based meteorological data from the South African Geodynamic Observatory, Sutherland.

Table 6: Satellite imaging data acquired for the study

Satellite sensor	Date	Path/Row
Landsat 7 Enhanced Thematic Mapper + (ETM +)	2009/08/12	174/082
Landsat 7 Enhanced Thematic Mapper + (ETM +)	2009/24/12	174/082
Landsat 7 Enhanced Thematic Mapper + (ETM +)	2010/09/01	174/082

3.2.3 CONVERSION TO RADIANCE

All the satellite images were georeferenced to WGS-1984 UTM coordinate system in order for the satellite images coordinates to be aligned with the ground coordinates. The satellite images are calibrated in which the QCAL (quantified and calibrated values) or DN (Digital numbers) values are changed to radiance, because radiance values are needed for

determining evapotranspiration (Ghulam, 2010). The conversion of digital numbers (DN's) into radiance units is done by utilising equation 20:

$$L_{\lambda} = \text{gain} * \text{QCAL} + \text{"offset"}$$

(20)

Also expressed as:

$$L_{\lambda} = \left(\frac{L_{\text{MAX}\lambda} - L_{\text{MIN}\lambda}}{\text{QCAL}_{\text{MAX}} - \text{QCAL}_{\text{MIN}}} \right) * (\text{QCAL} - \text{QCAL}_{\text{MIN}}) + L_{\text{MIN}\lambda}$$

(21)

Where:

- L_{λ}** = Spectral radiance in watts at the sensor aperture
- "gain"** = Rescaled gain (the data product "gain" contained in the Level 1 product header or ancillary data record) measured in watts (meter squared*ster * μm)
- "offset"** = Rescaled bias (the data product "offset" contained in the Level 1 product header or ancillary data record) in watts
- QCAL** = The quantized calibrated pixel value in DN
- $L_{\text{MIN}\lambda}$** = The spectral radiance that is scaled to QCAL_{MIN} in watts
- $L_{\text{MAX}\lambda}$** = The spectral radiance that is scaled to QCAL_{MAX} in watts
- QCALMIN** = The minimum quantized calibrated pixel value (corresponding to $L_{\text{MIN}\lambda}$) in DN =1 (LPGS Products) = 0 (NLAPS Products)
- QCALMAX** = The maximum quantized calibrated pixel value (corresponding to $L_{\text{MAX}\lambda}$) in DN = 255

Table 7 indicates two sets of LMAXs and LMINs. The first set should be utilised for Landsat Product Generation System (LPGS) produced before the 1st of July, 2000 and the second set should be used for data products produced after the 1st of July 2000.

Table 7: Spectral radiance range for Landsat 7 in watts

Band Number	Before July 1, 2000				After July 1, 2000			
	Low Gain		High Gain		Low Gain		High Gain	
	LMIN	LMAX	LMIN	LMAX	LMIN	LMAX	LMIN	LMAX
1	-6.2	297.5	-6.2	194.3	-6.2	293.7	-6.2	191.6
2	-6.0	303.4	-6.0	202.4	-6.4	300.9	-6.4	196.5
3	-4.5	235.5	-4.5	158.6	-5.0	234.4	-5.0	152.9
4	-4.5	235.0	-4.5	157.5	-5.1	241.1	-5.1	157.4
5	-1.0	47.70	-1.0	31.76	-1.0	47.57	-1.0	31.06
6	0.0	17.04	3.2	12.65	0.0	17.04	3.2	12.65
7	-0.35	16.60	-0.35	10.932	-0.35	16.54	-0.35	10.80
8	-5.0	244.00	-5.0	158.40	-4.7	243.1	-4.7	158.3

3.2.4 **RADIANCE TO REFLECTANCE**

Landsat scenes can be made clear, by reducing in between-scene variability, which is done through a normalization of solar irradiance by converting spectral radiance to planetary albedo or reflectance (Chander and Markham, 2003). The combined atmospheric and surface reflectance of the Earth can be calculated from equation 22.

$$\rho_p = \frac{\pi * L_\lambda * d_r}{ESUN_\lambda * \cos\theta_s} \quad (22)$$

Where:

- ρ_p = Unitless planetary reflectance
- L_λ = Spectral radiance at the sensors aperture
- d_r = Earth-Sun distance in astronomical units
- $ESUN_\lambda$ = Mean solar spectral irradiances
- $\cos\theta_s$ = Solar zenith angle/ cosine incident angle from Nadir

3.2.5 **CONVERSION OF BAND 6 INTO LAND SURFACE TEMPERATURE**

Landsat ETM+7 band 6 can be converted into a useful variable from spectral radiance into surface temperature (Allen *et al.*, 2011 and Ghulam, 2010). This temperature is known as radiative surface temperature or brightness temperature because it is quantified from the top of the atmosphere by a satellite imaging system (Becker and Li, 1990 and Maxton, 2004). In order to determine the surface temperature, pre-launch calibration constants have to be utilised. The equation being used to convert band 6 into surface temperature is as follows:

$$T = \frac{K2}{\left(\frac{K1}{L_\lambda} + 1\right)} \quad (23)$$

Where:

- T = Effective at-satellite temperature in Kelvin
- K2 = Calibration constant
- K1 = Calibration constant
- L_λ = Spectral radiance of band 6 in watts

3.3 **SOLAR ZENITH ANGLE**

The highest instantaneous value of solar radiation (Solar constant) measured outside the atmosphere at an average of Earth-Sun distance which is perpendicular to solar rays is equivalent to 1367 watt/m² (Sun et al., 2013). The total amount of energy at the top of the atmosphere is a function of the solar zenith angle at a certain time and latitude and the distance between the Earth and the sun.

3.3.1 **SOLAR DECLINATION**

The position of the sun during winter and summer is described by solar declination angle (δ) in radians. Whereas δ is written as:

$$\begin{aligned} \delta = & 0.006918 - 0.399912 \cos(da) + 0.070257 \sin(da) - 0.006758 \cos(2da) \\ & + 0.0000907 \sin(2da) - 0.002697 \cos(3da) + 0.00148 \sin(3da) \end{aligned} \quad (24)$$

In order to determine the solar declination angle, the day angle has to be determined first following the use of equation 25.

$$d_a = (d_n - 1) \frac{2\pi}{365}$$

(25)

Where:

d_a = day angle

d_n = Julian day

3.3.2 EQUATION OF TIME

Irregularities in the quantification of the local time and the sun's position can be caused by the axial rotation of the Earth along with the revolution of the Earth in the elliptical orbit around the sun. However, it can be rectified by the use of equation 26.

$$E_t = 0.000075 + 0.0018 \cos(da) - 0.032077 \sin(da) - 0.014615 \cos(2da) - 0.04089 \sin(2da)$$

(26)

3.3.3 LOCAL APPARENT TIME (LAT)

In circumstances where the Coordinated Universal time is provided, the local apparent time is determined from the following equation:

$$LAT = UTC + \frac{4 * L_c}{60} + \frac{E_t}{60}$$

(27)

Where:

UTC = Coordinated Universal time in hour

LAT = Local apparent time in hour

L_c = represents longitude

3.3.4 HOUR ANGLE

The local apparent time is used to calculate the hour angle (ω) using equation 28 which is given by Trezza (2002) as:

$$\omega = 15(LAT - 12) \frac{\pi}{180}$$

(28)

Where:

LAT = Local apparent time

ω = omega/ the hour angle, ω = positive in the afternoon, ω = negative in the morning and ω = 0 at solar noon

3.3.5 SOLAR ZENITH ANGLE/ THE SOLAR INCIDENCE ANGLE

The cosine of the solar zenith angle which is defined as the angle between a vertical line perpendicular to the Earth's surface and the solar beam is quantified following the use of equation 29 (Weligepolage, 2005):

$$\cos\theta = \sin(\phi) \sin(\delta) + \cos(\phi)\cos(\delta)\cos(\omega)$$

(29)

Where:

θ = 90°, at the hour of sunset

ϕ = latitude of the pixel which is positive for the Northern Hemisphere and negative for the Southern hemisphere.

The latitude pixel (ϕ) equation is expressed by Trezza (2002) as:

$$\phi = \text{latitude} * \left(\frac{\pi}{180}\right)$$

(30)

The sunset hour angle equation is given as:

$$\cos(\omega) = \tan(\phi)\tan(\delta)$$

(31)

Whereas the day length equation is expressed as:

$$N = \frac{2}{5} \cos^{-1}(-\tan(\phi)\tan(\delta))$$

(32)

Where:

ϕ = latitude pixel in radians which is positive for the Northern Hemisphere and

negative for the Southern Hemisphere.

δ = solar declination in radians

3.3.6 CONVERSION OF REFLECTANCE (ρ) AND TEMPERATURE (T_{rad}) INTO MAPS

The thermal and reflective bands of Landsat 7 sensor were converted into temperature and reflectance maps utilising the calibration constants and the cosine solar zenith angle. Band 6 of the Landsat 7 sensor was converted into temperature and band 1,2,3,4,5 and 7 were converted into reflectance.

3.4 SEBAL METHODOLOGY

The SEBAL model, determines evapotranspiration from meteorological data and satellite images utilising the surface energy balance, (Trezza 2002). The satellite image provides information strictly limited to the satellite overpass time. Therefore, SEBAL determines an instantaneous evapotranspiration/latent heat, sensible heat, soil heat and net radiation flux for the image at the time of the satellite overpass (Timmermans et al., 2007). The schematic illustration below shows how evapotranspiration can be measured from remotely sensed data (Opoku-Duah et al., 2008).

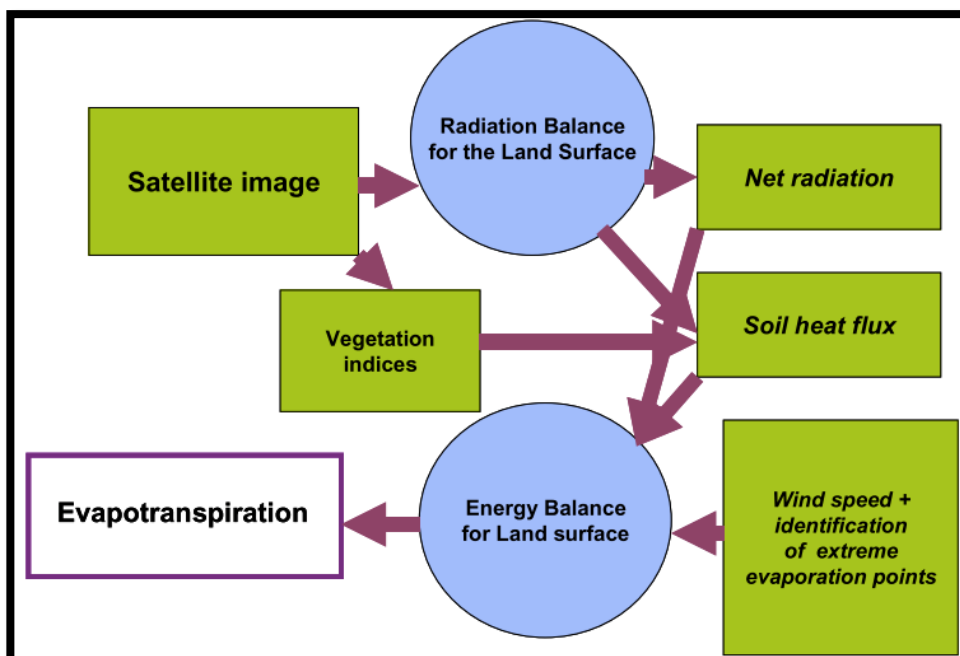


Figure 10: Actual framework of how to determine evapotranspiration (Opoku-Duah et al., 2008)

The commonly used method to determine evapotranspiration for each individual satellite pixel is based on the surface energy balance (Cristóbal et al., 2017). Equation 33 can be expressed in $\text{MJ m}^{-2} \text{d}^{-1}$ or W m^{-2} , being negative or positive (Teixeira, 2010). Where, the latent heat flux is quantified as a residual of the surface energy balance (Gao et al., 2011). The latent heat flux is significant in vaporizing water from the soil and vegetation surfaces.

$$LE = R_n - G - H \quad (33)$$

Where:

LE = Latent heat/Evapotranspiration flux

R_n = Net radiation

G = Soil heat flux

H = Sensible heat

The sensible heat flux H which is responsible for heating and cooling of the air is described as a function of the temperature difference between the lower part of the atmosphere and the canopy surface (Gao et al., 2011; Karimi and Bastiaanssen, 2015).

Majority of the energy penetrating the soil surface during the afternoon leaves the soil in the form of terrestrial long-wave radiation at night. Therefore the soil heat flux is regarded as a small fraction which can be ignored during the day (Jansen et al., 2011). However, if the soil heat flux is ignored, it may lead to inconsistencies in the surface energy balance.

The soil heat flux has an identical function which is related to temperature difference between the top soil and the land surface (Karimi and Bastiaanssen, 2015). An increase in surface temperature will increase the soil heat and sensible heat fluxes.

3.4.1 **PLANETARY ALBEDO (r_p)**

The planetary broadband albedo is defined as the magnitude of the reflected incoming solar radiation (about 29%) by the Earth's surface into the atmosphere (Stephens, 2015; Trlica et al., 2017). The planetary albedo is quantified at the solar effective wavelength which ranges between 0.3-3 μm in the visible range of the spectrum (Laounia et al., 2017). The planetary albedo is calculated by using equation 34 (Kosa, 2003; Wubet, 2003).

$$r_p = \frac{\sum ESUN \cdot \rho_p}{\sum ESUN_\lambda}$$

(34)

Where:

ρ_p = planetary reflectance

$ESUN$ = Sun-Earth distance for band 1-5 and 7

3.4.2 **BROADBAND SURFACE ALBEDO (r_o)**

The surface albedo is utilised as a regulating factor that determines the amount of incoming solar radiation being reflected by the Earth's surface (Liang et al., 2010). In order to determine the magnitude of broadband surface albedo using equation 35, the degree of transmissivity has to be known by employing equation 36.

$$r_o = (r_p - r_{pmin})/\tau^2 \quad (35)$$

Where, r_o represents the broadband surface albedo, r_p represents the planetary albedo, r_p is representative of the minimum planetary albedo. Transmissivity (τ^2) is dependent on atmospheric conditions such as cloud optical thickness, cloud content, aerosol extinction and absorption by other gases and water vapor (Matsuda et al., 2006). In addition, Trezza (2002) defined transmissivity (τ^2) as the degree of the incoming and outgoing solar radiation that is being reflected and absorbed in the atmosphere. The daily transmittance is equivalent to the instantaneous transmittance and can be computed as follows:

$$\tau_{day} = (a_s + b_s * \frac{n}{N}) \quad (36)$$

Constant values of 0.25 and 0.5 are given to a_s and b_s respectively, where n is the total number of sunshine hours. The day length is given as N .

3.5 BIO PHYSICAL PARAMETERS

In order to determine the bio physical parameters needed for the SEBAL model, a statistical method was developed by Bastiaanssen (1998). The bio-physical parameters are generally calculated from vegetation indices (Normalized Difference Vegetation Index, Soil Adjusted Vegetation Index and Leaf area Index) utilising the band reflectance of Near-Infrared and Visible (Gilbert et al., 2002; Lu et al., 2015). The role of vegetation indices is to reduce soil

background effects and solar irradiance whilst enhancing vegetation signals (Huete et al., 2002).

Reflectance is defined by Govaerts and Verhulst, (2010) as “the ratio of energy that is reflected from an object to the energy incident on the object”. Plants tend to have low reflectance in the visible spectrum, due to absorption by photosynthesis pigments such as carotenoids and chlorophylls. However, in the near infrared plants tend to have a higher reflectance because of the structural discontinuities of the leaf, hence plants appear green to our eyes, Figure 11.

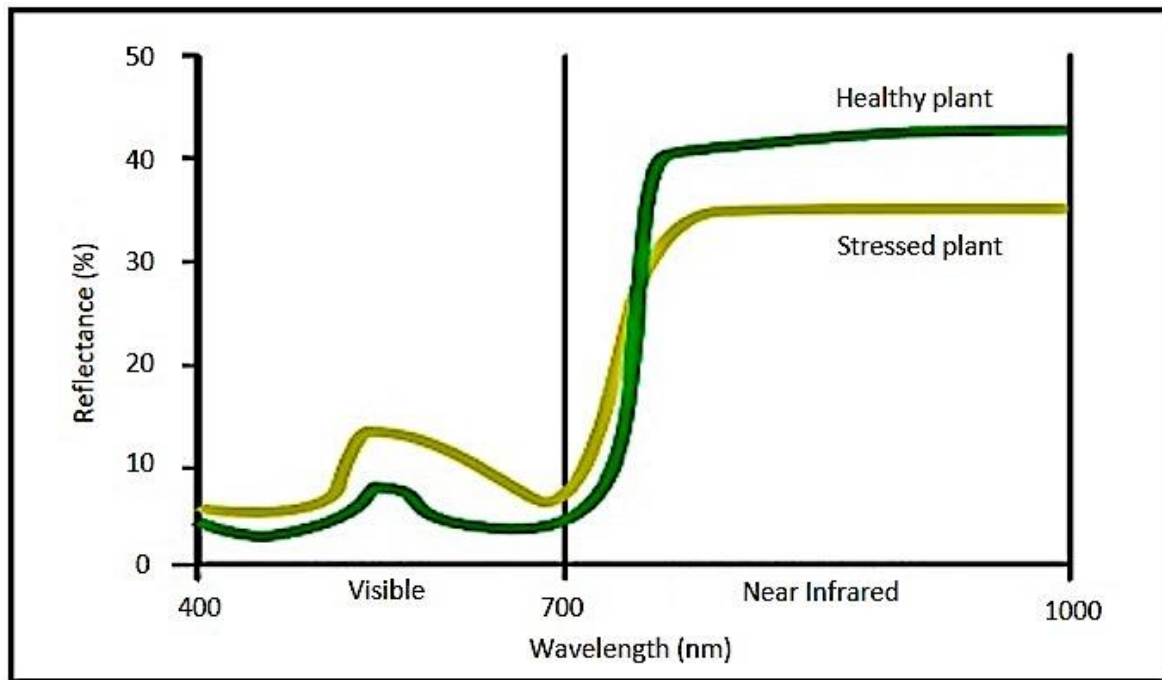


Figure 11: Typical reflectance spectrum of a stressed and healthy plant (Kumar and Silva, 1973, cited by Govaerts and Verhulst, 2010)

3.5.1 **NORMALIZED DIFFERENCE VEGETATION INDEX**

The Normalized Difference Vegetation Index (NDVI) indicates the amount and vigor of vegetation on the Earth’s surface (Junges et al., 2017). The NDVI is also closely related to the leaf area index (LAI) in canopies (Hatfield and Prueger, 2010). Healthy leaves/plants have a low reflectance percentage of 20% or less in the visible green-red range ($\lambda = 550 - 700$ nm) and about a 60% reflectance in the near infrared region ($\lambda = 700 - 1300$ nm) of the electromagnetic spectrum Figure 11. The NDVI values quantified through remote sensing techniques range between -1 and +1 (Huete et al., 2002). Cloud and water surfaces generally have values less than zero, whereas green surfaces have values ranging between 0 and 1 (Ali et al., 2016). The NDVI is determined from measurements of reflectance in the near

infrared and visible part of the spectrum and the equation is written as (Jato-Espino et al., 2017):

$$NDVI = \frac{R_{NIR} - R_{Red}}{R_{NIR} + R_{Red}} \quad (37)$$

Where:

R_{NIR} = The reflectance of NIR radiation

R_{Red} = The reflectance of visible red radiation

3.5.2 **SOIL ADJUSTED VEGETATION INDEX (SAVI)**

The SAVI was developed by Huete, (1988). This model aims to reduce the impacts associated with soil background in the application of vegetation indices (Hatfield and Prueger, 2010).

The initial model formulation of SAVI was based on measurements of grass and cotton canopies with light and dark soil background (Huete, 1988). The adjustment factor 'L' utilised in the SAVI model is aimed at reducing the impacts associated with soil background on the vegetation quantification (Mróz and Sobieraj, 2004). The correction factor for very high densities is equal 0 and for low densities is equal to 1 (Huete, 1988 and Ahmad, 2011). However, for areas with no information of the adjustment factor 'L' a value of 0.5 can be utilised (Gilabert et al., 2002; Kosa, 2003). When the value of L=0, then SAVI=NDVI (Ahmad, 2012; Lu *et al.*, 2015).

The equation used to determine SAVI is given in equation, 38 as:

$$SAVI = \frac{(NIR - R)}{NIR + R + L} (1 + L) \quad (38)$$

Where R and NIR represents reflectance value found in band 3 and 4 respectively.

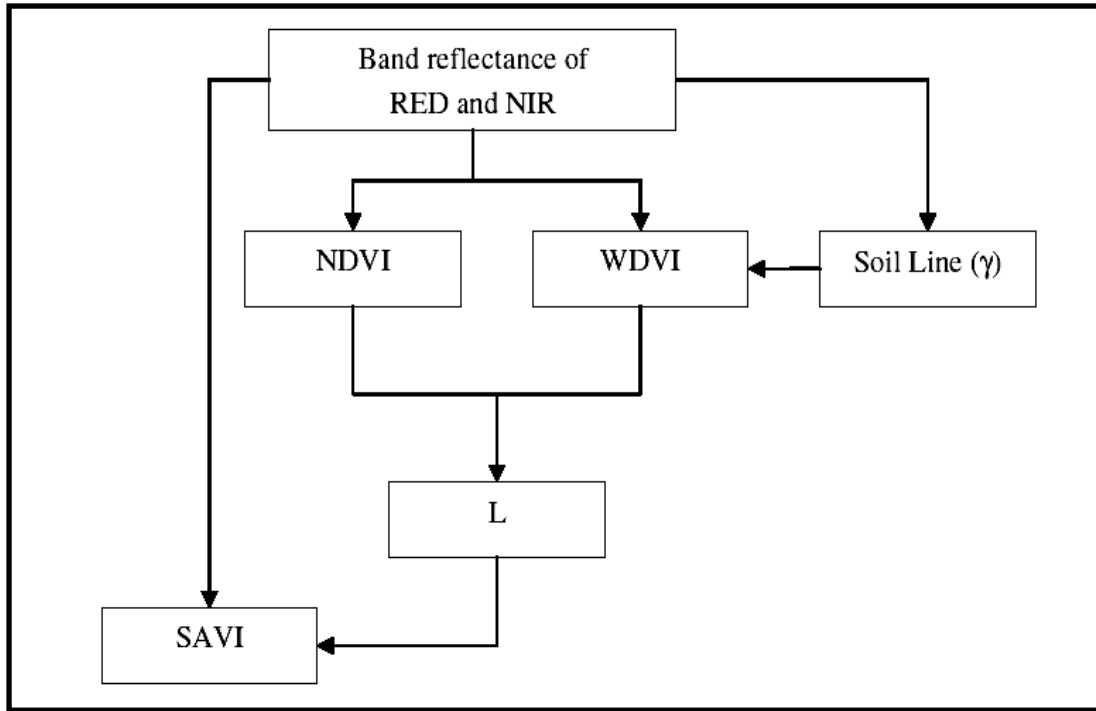


Figure 12: Actual framework of deriving the Soil Adjusted Vegetation Index value (Bala 2010)

The linear relationship that exists between bare soil reflectance observed between the near-infrared (NIR) and RED waveband is termed as the soil line (Richardson and Wiegand, 1977; Baret *et al.*, 1993; Yoshioka *et al.*, 2010). The equation of the soil line is given as:

$$\rho_{NIR} = \gamma \rho_{RED} + \beta \quad (39)$$

Typically γ is zero and β varies between -0.1 and 0.1 (Weligepolage, 2005). The weighted difference vegetation index (WDVI) is a variant of SAVI which aims to minimise the effects associated with variable soil background (Mróz and Sobieraj, 2004). The WDVI and the correction factor L is given in equation 40 and 41, respectively.

$$WDVI = NIR - \gamma \cdot R \quad (40)$$

Where:

NIR = Near infrared

γ = slope of the soil line

$$L = 1 - 2a \cdot NDVI \cdot WDWI \quad (41)$$

Where:

a = 0.5

3.5.3 **LEAF AREA INDEX**

The total biomass, heat flux, canopy resistance and the crop yield is indicated by the Leaf Area Index (Pope and Treitz, 2013). The LAI is defined as the magnitude of the leaf area (m^2) per unit ground area (m^2) in a canopy (Asner *et al.*, 2003; Gitelson *et al.*, 2003). LAI, is a dimensionless quantity, which can be analysed, modelled and measured across various spatial scales from tree clusters to individual trees or from local to regional to global scales (Rouse *et al.*, 1973; Asner *et al.*, 2003). The equation for LAI is given as (Bastiaanssen, 1998):

$$LAI = \frac{SAVI - C_1}{c_2} \quad (42)$$

Where:

C_1 = 0.13

c_2 = 0.35

3.5.4 **AERODYNAMIC ROUGHNESS LENGTH (Z_{om})**

Aerodynamic surface roughness length (Z_{om}) is a surface component, that can be used to scale the vertical profile of the horizontal parameter of the wind and distinguish the capacity of the surface to consume momentum from the airflow (Chen *et al.*, 2015). In various applications of meteorology and surface hydrology, the aerodynamic length is of paramount importance for determining heat and mass exchange between the atmosphere and land surface (Toda, 2003).

The roughness length is defined as the height above the surface, where the horizontal wind

profile reaches a stage of equilibrium and the vertical momentum fluxes are constant (Brock, *et al.*, 2000). The surface geometry is closely linked to the value of aerodynamic surface roughness (Maurer *et al.*, 2013). The surface roughness length was determined by using an equation developed by Bastiaanssen, (1998):

$$Z_{om} = \text{Exp} (C_1 + C_2 \cdot NDVI) \quad (43)$$

Where:

$$C_1 = -5.5$$

$$C_2 = 5.8$$

3.5.5 SURFACE ROUGHNESS FOR HEAT TRANSPORT (Z_{oh})

The surface roughness for heat is calculated using equation 44. Where KB^{-1} is a parameter coined as an excess resistance for heat transfer which is used to compare Z_{oh} and Z_{om} . The value of KB^{-1} for well grown homogenous grass is given as 2.3.

$$Z_{oh} = \frac{Z_{om}}{\exp(KB^{-1})} \quad (44)$$

3.5.6 DISPLACEMENT HEIGHT AND WIND PROFILE

The displacement height which is influential in the plant height is determined using equation 45, which is given as (Bastiaanssen, 1998):

$$d = h \left[1 - \frac{1 - e^{\sqrt{C_1 LAI}}}{\sqrt{C_1 LAI}} \right] \quad (45)$$

Where:

$$h = \text{crop height 1}$$

$$C_1 = 20.6$$

The above equation is dependent on the LAI map and requires only one coefficient. The wind speed is a phenomena influenced by height above the surface (Immerzeel *et al.*, 2006). When the wind blows close to the surface, it is assumed that the wind speed is zero because of frictional effects of the air (Immerzeel *et al.*, 2006). However, as the wind blows further away from the surface, the effects and wind speed increases (Al-Abbadi and Rehman, 2009). Thus,

an inversely proportional relationship exists between air momentum and height, Figure 13.

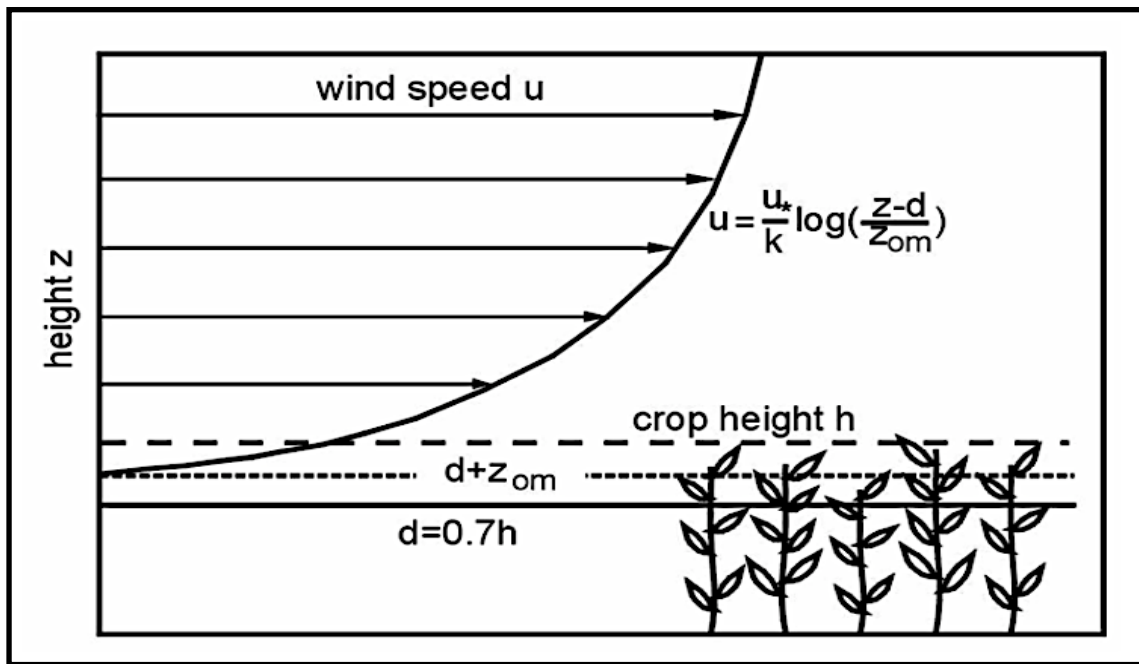


Figure 13: Inversely proportional relationship between wind speed and height (Immerzeel *et al.*, 2006)

3.6 SURFACE EMISSIVITY

The ratio of the energy emitted by a body at specific temperature to the energy emitted by a blackbody at an identical temperature is referred to as emissivity (Wubet, 2003). There is a vast difference in the emissivity of natural surfaces due to the difference in, soil composition, moisture content, soil structure and organic matter. Surface with near complete or complete vegetation will generally have an emissivity of 0.97 and 0.98 (Schott and Volchok, 1985). The emissivity of pure fresh water will have an emissivity of 1.0 (Marlatt, 1967), whereas natural lake water will range around 0.97 (Raphael, 1962 and Davies *et al.*, 1971). The apparent emissivity which is dependent on vegetation cover characteristics is quantified with an equation based on temperature and vapor pressure (Brutsaert, 1975).

$$\varepsilon_a = 1.24 \left(\frac{e_a}{T_a} \right)^{1/7} \quad (46)$$

Where:

e_a = saturation vapor pressure

T_a = air temperature

3.7 INCOMING SHORTWAVE RADIATION

The incoming shortwave radiation, which is defined as the diffuse and direct solar radiation that reaches the surface is determined using the equation below (Sun et al., 2013):

$$R_s^\downarrow = s_0 \times \cos\theta \times dr \times \tau_{sw} \quad (47)$$

Where:

- R_s^\downarrow = Incoming shortwave radiation
- s_0 = Solar constant (1367 W/m²)
- τ_{sw} = Transmissivity
- dr = Earth-Sun distance
- $\cos\theta$ = cosine of the solar zenith angle

The outgoing longwave radiation given in equation 5 is calculated using the Stefan-Boltzmann equation. The values of the outgoing longwave radiation which depends on the time and location of the image, ranges between 200-700 W/m²(Trezza, 2002).

The SEBAL process uses two anchor pixels of cold and dry pixels. Therefore, before calculating the incoming longwave radiation, the cold and wet pixels have to be manually selected on the satellite image. The quality of modelling evapotranspiration depends on these anchor pixels. The incoming solar radiation is calculated using the following equation:

$$R_{L\downarrow} = 0.85 \times (-\ln\tau_{sw})^{.09} \times \sigma \times T_{cold}^4 \quad (48)$$

The values of incoming solar radiation which are dependent on the time and location of the image ranges between 200 – 500 W/m² (Trezza, 2002). The final step in this section is to quantify the net radiation, using equation 2.

3.8 SOIL HEAT FLUX

Conduction is the primary form of transport that is active in the soil. Therefore, soil heat flux is explained as the momentum of heat energy in the soil used for cooling or heating the substrate soil (Opoku-Duah *et al.*, 2008; Li *et al.*, 2009; Gowda *et al.*, 2011). The soil heat flux is determined by utilising the empirical equation of Bastiaanssen, 1998, which is given as:

$$G_0 = R_n \frac{T_s - 273}{\alpha} (0.0032 \times (1.1 \times \alpha) + 0.0062 \times (1.1 \times \alpha)^2 \times (1 - 0.978 \times NDVI^4)) \quad (49)$$

Where:

T_s = Surface temperature

$NDVI^4$ = Normalized Difference Vegetation Index.

G = Soil heat flux

α = albedo

R_n = Net radiation

3.9 SENSIBLE HEAT FLUX (H)

The sensible heat flux is considered as the heat transfer between the atmosphere and the ground, which is pivotal in cooling/warming the air slightly above the surface (Opoku-Duah *et al.*, 2008 and Liang *et al.*, 2009). The sensible heat flux equation is given as (Paul and Aiken, 2013):

$$H = \frac{P_a \times C_p \times T_o - T_a}{r_{ah}} \quad (50)$$

Where:

P_a = density of the air

C_p = the air specific capacity

T_a = average air temperature at 2m

T_o = aerodynamic surface temperature at 0.1m

r_{ah} = Aerodynamic resistance for heat transport

The aerodynamic temperature is difficult to quantity, therefore SEBAL substitutes $T_o - T_a$ by a dT function depicted in equation 51. Where the dT function is explained as the near surface temperature difference quantified between two heights, 2m and 0.1m (Allen *et al.*, 2011). The sensible heat equation with a new substitute is then written as:

$$H = \frac{P_a \times C_{pa} \times dT}{r_{ah}} \quad (51)$$

The latter equation is often difficult to solve because of two unknown parameters, dT and r_{ah} . Therefore, the dry pixel has to be manually selected in order to get valid values of Sensible heat and to determine dT (Mkwanazi, 2014). The dry pixel is considered a pixel with extreme temperature. This pixel of extreme temperature is an ideal candidate for a dry pixel which

represents extreme dryness, due to the available energy at the surface being used to warm up the surface and the air above, as there is no water to evaporate (Mkwanzazi, 2014). In addition, the pixel should represent a surface with minimal biomass or a dry uncovered agricultural land (Bastiaanssen *et al.*, 2005) which is characterised by a low leaf area index (LAI) value. The pixel is assumed to have a large dT value.

3.9.1 **AERODYNAMIC RESISTANCE TO HEAT TRANSPORT (r_{ah})**

The integrated factors of surface roughness (vegetation structure and height), atmospheric stability and wind speed tend to influence aerodynamic resistance (Li *et al.*, 2009). Aerodynamic resistance (r_{ah}) has an inversely proportional relationship with wind speed and it tends to decrease when the surface becomes rougher (Hatfield *et al.*, 1983). The work of Treza (2002) indicates that the aerodynamic resistance to heat transport (r_{ah}) is quantified for neutral stability utilising equation (51) given as:

$$r_{ah} = \frac{1}{ku_*} \left[\ln \left(\frac{z_{ref} - d}{z_{oh}} \right) - \psi_h \right] \quad (52)$$

Where:

- z_{ref} = Is a constant value of 2m
- K = von Karman's constant (0.41)
- u_* = friction velocity (m/s)
- d = Displacement height
- z_{oh} = Surface roughness for heat transport
- ψ_h = Correction factor for heat transfer

3.9.2 **FRICTION VELOCITY (u_*)**

The friction velocity calculates the turbulent velocity fluctuations in the air through a logarithmic wind law equation for stable atmospheric conditions (Spiliotopoulos *et al.*, 2017 and Ndou *et al.*, 2017):

$$u_* = \frac{k * U_B}{\ln \left(\frac{z_B - d}{z_{om}} \right) - \psi_m} \quad (53)$$

Where:

- k = von Karman's constant
- U_B = Wind speed at blending height
- Z_B = blending height
- ψ_m = Correction factor for momentum transfer
- d = Displacement height
- Z_{om} = Surface roughness for momentum transport

The frictional velocity calculation is normally done on a calculator or on a spreadsheet (Allen *et al.*, 2002).

3.9.3 **WIND SPEED AT BLENDING HEIGHT (U_B)**

The height at which surface roughness can be ignored is considered as blending height (Horvat, 2013). At this height (200m above the ground) the wind velocity is said to be constant for the entire region, and is quantified as a function of roughness length and friction velocity. The blending height equation is given as (Paul and Aiken, 2013):

$$U_B = U_{ref} \left(\frac{\ln(Z_B - d) - \ln(Z_{om})}{\ln(Z_{ref} - d) - \ln(Z_{om})} \right) \quad (54)$$

Where:

- U_{ref} = Wind speed from the meteorological weather station
- Z_B = blending height
- d = displacement height
- Z_{ref} = A constant value of 2m

3.9.4 **MONIN-Obukhov LENGTH (L)**

In the iterative process the Monin-Obukhov (L) equation is utilised to define the stability of the atmosphere, Figure 15 (Trezza, 2002). Note that this (L) is not identical to the one used in the computation of SAVI. The Monin-Obukhov (L) is regarded as a function of momentum and heat fluxes which is determined as:

$$L = \frac{\rho C_p u_*^3 T_s}{kgH} \quad (55)$$

Where:

- k = von Karman's constant
- p = density of the air
- C_p = air specific heat
- u_* = friction velocity
- T_s = surface temperature
- g = gravity
- H = Sensible heat

The values of the Monin-Obukhov (L) indicate the stability of the atmosphere. Under unstable conditions $L < 0$, and under stable conditions $L > 0$ and in the situation whereby $L = 0$ the atmosphere is regarded neutral (Trezza, 2002).

3.9.5 CORRECTION FACTORS

Vertical gradients are often difficult to measure accurately, therefore a correction factor between two heights is integrated. These correction factors are applied to heat and momentum transfer with suffixes of "m" and "h", respectively to equation 56 and 58.

$$x_m = \left(1 - 16 \frac{Z_B - d}{L}\right)^{0.25} \quad (56)$$

$$\psi_m = 2 \ln \left[\frac{(1+x_m)}{2} \right] + \ln \left[\frac{1+x_m^2}{2} \right] - 2 \arctan(x_m) + \frac{\pi}{2} \quad (57)$$

$$x_h = \left(1 - 16 \frac{Z_{ref} - d}{L}\right)^{0.25} \quad (58)$$

$$\varphi_h = 2 \ln \left[\frac{(1+x_h)^2}{2} \right] \quad (59)$$

The combination of the above three equations results in a new equation, expressed as:

$$T_0 - T_a = \frac{H}{k \rho_a C_p u_*} \left[\ln \left(\frac{Z_{ref} - d}{Z_{oh}} \right) - \varphi_h \right] \quad (60)$$

According to Papadavid *et al.*, (2017) the SEBAL methodology utilises the dry and wet pixels to develop a linear relationship between the radiometric surface temperature T_o and the difference between the radiometric surface temperature and air temperature ($T_o - T_a$). The difference between ($T_o - T_a$) is assumed to be related to the surface temperature (Jacob *et al.*, 2002; Paul and Aiken, 2013) :

$$T_o - T_a = dT = a + b \times T_o \quad (61)$$

Where 'a' and 'b' are empirical linear regression coefficients acquired from an anchor pixel (wet and dry), once the coefficients are acquired dT is determined using the surface temperature (Bastiaanssen *et al.*, 1995). Figure 14 shows how coefficients 'a' and 'b' was determined for the first satellite image, the linear regression graphs for the other two graphs are depicted in Appendix (B). The relationship of the NDVI-albedo and temperature-albedo is used to carefully select the dry and wet pixel in a satellite image. The dry pixel is usually selected from a pixel with a low NDVI and a high temperature value. Whereas, the wet pixel is selected from a pixel with a high NDVI and low temperature (Paul and Aiken, 2013). The sensible heat flux is given as zero for the wet pixel and because $T_o - T_a = dT$, the value of dT is given as zero (Paul *et al.*, 2013). However, for the dry pixel $dT = dT_{max}$ and the sensible heat flux is given as a maximum value (H_{max}).

The dT_{max} is quantified through an iterative process using equation 61, 62 and 52 (Paul *et al.*, 2013), the iterative process for all three satellite images is depicted in Appendix (C).

$$H_{max} = C_a C_p \frac{dT_{max}}{r_{ah}} \quad (62)$$

Where:

C_a = density of the air (1.17 kg m^{-3})

C_p = air specific heat at constant pressure ($1.005 \text{ J kg}^{-1} \text{ K}^{-1}$)

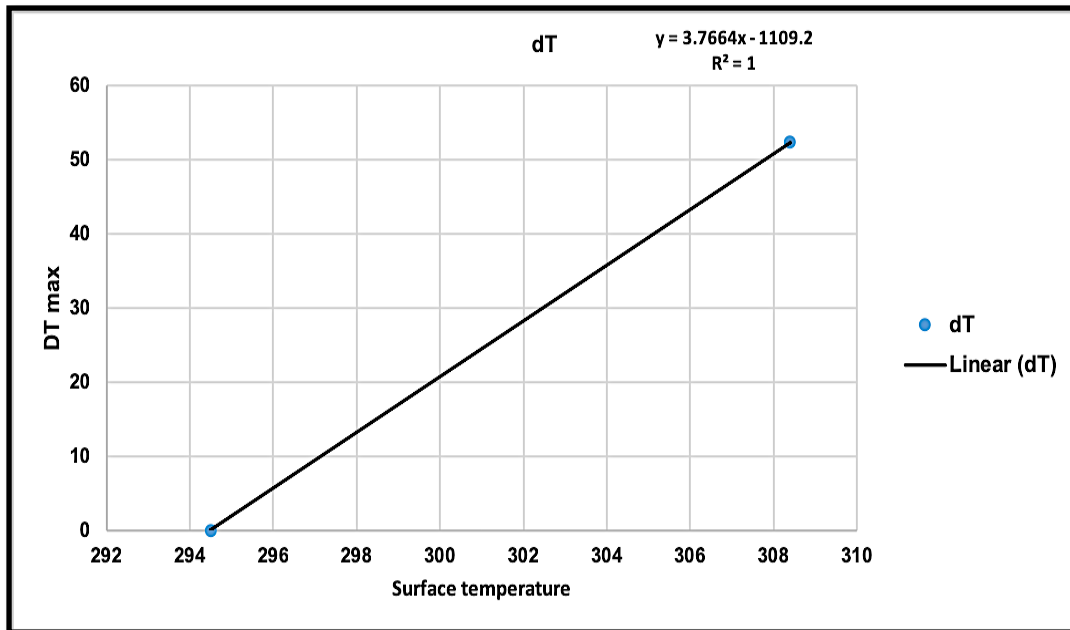


Figure 14: Solving for coefficients using the dry and wet pixels

After the dry and wet pixels were determined, the values of T_o -dry, R_n -dry, d_h -dry, T_o -wet and G_o -dry are easily accessible from the corresponding maps. The suffix wet and dry represents wet and dry pixel values. The correction factors of ψ_m and ψ_h were initially taken as “0”. The dT map was determined as $dT = a + b \cdot T_s$. Figure 15 represents a conceptual framework of the iterative process used to calculate the sensible heat flux, the process is run until a constant value of those parameters is attained (Bala, 2010).

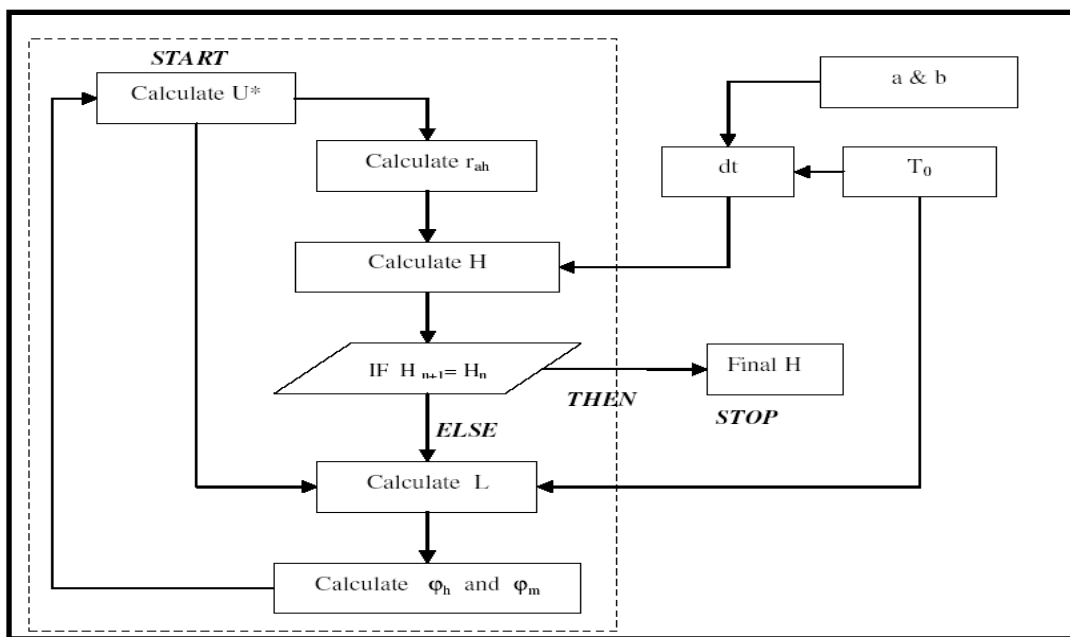


Figure 15: The iterative process used to determine sensible heat flux values (Bala, 2010)

3.10 INSTANTANEOUS LATENT HEAT FLUX

Immediately after calculating the components in the energy balance, the Instantaneous latent energy flux which is responsible for changing liquid into water vapor has to be calculated (Horvat, 2013). The Instantaneous latent heat which is based on Equation 7 is considered as the residual of the surface energy budget (Papadavid et al., 2017). All the components of the surface energy balance are instantaneous and are given in W/m^{-2} .

3.11 EVAPORATIVE FRACTION

The ratio between latent heat flux (λE) and available surface energy ($R_n - G$) is defined as the evaporative fraction (Nutini et al., 2014; Papadavid et al., 2017; Peng and Loew, 2014). Daily evaporative fraction can be calculated using the instantaneous evaporative fraction equation, by assuming that the daily evaporative fraction remains constant during the day time hours (09:00-15:00), on cloud-free days (Lee and Kim, 2016; Lu et al., 2015). This assumption is based on numerous studies, which concludes that evaporative fraction remains steady during the day (Cargo, 1996, Tang and Li, 2015 and Cammalleri *et al.*, 2014). The difference between the evaporative fraction for a 24-h cycle and at the time of the satellite overpass is marginal, and can be ignored (Papadavid et al., 2017). The instantaneous evaporative fraction is then calculated as:

$$\Lambda_{ins} = \frac{\lambda E}{R_n - G} \quad (63)$$

3.12 DAILY NET RADIATION

The daily net radiation is defined as the sum of the longwave radiation and shortwave radiation and can be expressed as (Wu et al., 2017):

$$R_{n-day} = R_{ns} + R_{nl} \quad (64)$$

Where:

R_{n-day} = Daily net radiation

R_{ns} = Net shortwave radiation

R_{nl} = Long wave radiation

The net shortwave radiation is quantified by initially determining the global solar irradiation and the surface albedo, where the global solar radiation R_s equation is given as (Wu et al., 2017):

$$R_{ns} = R_s(1 - \alpha) \quad (65)$$

Where:

R_{ns} = Net shortwave radiation

R_s = global solar radiation

α = Surface albedo

The global solar radiation equation which is based on the Angstrom-Prescott model is written as:

$$R_s = (a_s + b_s \frac{n}{N})R_a \quad (66)$$

Where:

n = actual sunshine hours

N = Maximum sunshine hours

a_s = empirically determined coefficients

b_s = empirically determined coefficients

R_a = extra-terrestrial solar irradiance

The extra-terrestrial solar irradiance is determined with the use of this equation:

$$R_a = \frac{24 \times 60}{\pi} G_{sc} d_r [\omega_s \sin(\phi) \sin(\delta) + \cos(\phi) \cos(\delta) \sin(\omega_s)] \quad (67)$$

Where:

d_r = Earth-sun distance

G_{sc} = solar constant $0.082 \text{ Mj.m}^{-2}.\text{min}^{-1}$

δ = solar declination in radians

ω_s = The sunset hour angle

The values of the solar declination (δ) and Earth-sun distance (d_r) can be calculated using equation 68 and 69 respectively, where j represents the Julian day of the calendar.

$$\delta = 0.409 \sin\left(\frac{2\pi}{365}j - 1.39\right) \quad (68)$$

$$d_r = 1 + 0.033 \cos\left(\frac{2\pi}{365}j - 1.39\right) \quad (69)$$

The sunset hour ω_s is determined using the following two parameters (δ and φ), and the equation for determining ω_s is given as:

$$\omega_s = \arccos = [-\tan(\varphi)\tan(\delta)] \quad (70)$$

The maximum possible sunshine hours are calculated following this equation:

$$N = \frac{24}{\pi} \omega_s \quad (71)$$

Net longwave radiation is quantified for clear sky conditions by utilising equation 72 given as:

$$R_{nl} = \sigma \frac{T_{\max}^4 + T_{\min}^4}{2} \varepsilon_{\text{net}} f_{\text{cloudiness}} \quad (72)$$

Where

σ = Stefan-Boltzman constant

T_{\max}^4 = Maximum air temperature at a height of 2m

T_{\min}^4 = Minimum air temperature at a height of 2m

ε_{net} = Net emissivity

$f_{\text{cloudiness}}$ = The cloudiness factor

The cloudiness factor equation can be written as:

$$c_1 \frac{n}{N} + d_1 \quad (73)$$

Where:

$$c_1 = 0.9$$

$$d_1 = 0.1$$

Both these latter coefficients are suggested in the work of Penman (1948) and Jensen *et al.*, (1990).

3.13 DAILY EVAPOTRANSPIRATION

The daily evapotranspiration was quantified using the evapotranspiration equation which can be written as:

$$ET_{24} = \frac{\Lambda_{ins} R_{n-daily}}{28.588} \quad (74)$$

Where:

$$\Lambda_{ins} = \text{Instantaneous evaporative fraction}$$

$$R_{n-daily} = \text{Daily net radiation}$$

3.14 REFERENCE EVAPOTRANSPIRATION EQUATION

The remotely sensed evapotranspiration is validated with the use of the American Society of Civil Engineers reference evapotranspiration equation, which utilises meteorological data as inputs in the equation to determine evapotranspiration. The equation is given as:

$$ET_{sz} = \frac{0.408\Delta(R_n - G) + \gamma_{T+273}^{C_n} U_2 (e_s - e_a)}{\Delta + \gamma(1 + C_d u_2)} \quad (77)$$

Where:

$$ET_{sz} = \text{standardized reference crop evapotranspiration for tall (ET}_{rs}) \text{ surfaces or short (ET}_{os})$$

$$R_n = \text{Net radiation}$$

$$G = \text{Soil heat flux}$$

$$e_s = \text{Saturation vapor}$$

$$e_a = \text{mean actual vapor pressure}$$

$$\Delta = \text{slope of vapor pressure}$$

$$\gamma = \text{psychrometric constant}$$

- C_n = numerator constant
 C_d = denominator constant
 T = air temperature

3.15 CHARACTERISING EVAPORATION AND RAINFALL DATA OF SUTHERLAND

Measurements of evaporation are normally quantified through the use of a Class A evaporation pan. The pan is usually mounted onto a wooden platform, which is placed on top of a surface with grass. The pan is normally exposed to ambient conditions after it has been filled with water. The evaporation rate is then measured by a gauge. In order to measure the evaporation rate, it is pivotal to measure the water and the rainfall level in the pan simultaneously. The evaporation and rainfall data for this study was measured on daily interval. The data was then characterised into yearly and monthly averages for the years 1983-2009.



Figure 16: Class-A type pan

4. RESULTS AND DISCUSSION

This section will focus on the results of the dissertation. An in-depth analysis on the spatiotemporal measurements of some of the energy balance parameters as well as evapotranspiration measurements will be given. A total number of 3 satellite images from Landsat 7 were used to model the surface energy balance parameters as well as the spatiotemporal variability of evapotranspiration. The actual evapotranspiration measurements were then validated with ground-based evapotranspiration measurements.

4.1 EVAPORATION AND RAINFALL DATA FROM AN A-CLASS TYPE PAN

A 26-year trend of the annual average precipitation and evaporation rates of Sutherland is depicted in Figure 17. The year 1985 and 2001 received the highest annual precipitation rates of 419mm and 354mm, respectively. The highest evaporation rates were experienced during the year 1996 and 1984 with evaporation rates of 304mm and 224mm, respectively, Figure 17. The cause of the low annual evaporation rates of 94mm, 27mm and 75mm for the year 2007-2009 may be due to some technical errors associated with the pan. This assumption is based on data gaps for several months during the year 2007-2009.

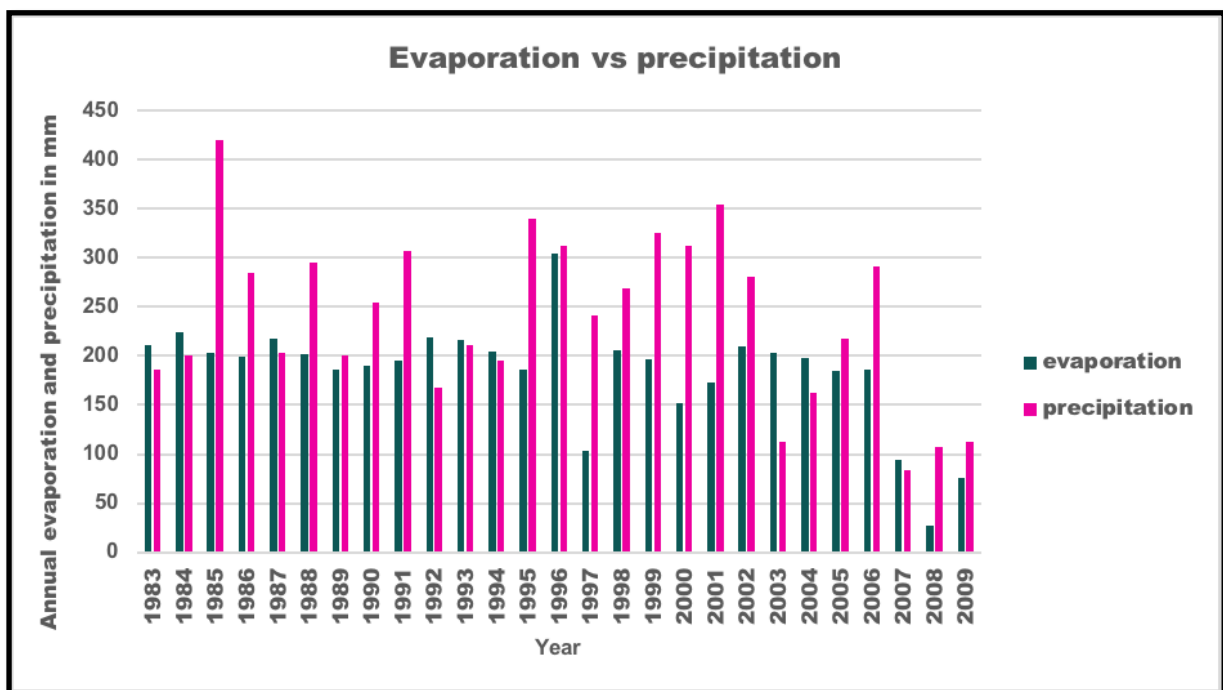


Figure 17: Class A pan-type evaporation and precipitation data from the year 1983-2009

Sutherland is a remote location situated 146 meters above sea level, having a Mediterranean climate. A Mediterranean climate is defined as a region which receives winter rainfall and summer drought (Blumler, 2005). This statement can be supported by Figure 18 which shows a 23-year trend of monthly average precipitation and rainfall data. The highest levels of precipitation was recorded in winter, with May having the highest precipitation rates of 24,62mm. Due to the elevated altitude, temperatures in winter tend to drop beyond freezing point, making Sutherland the coldest town in the country (Vey et al., 2016).

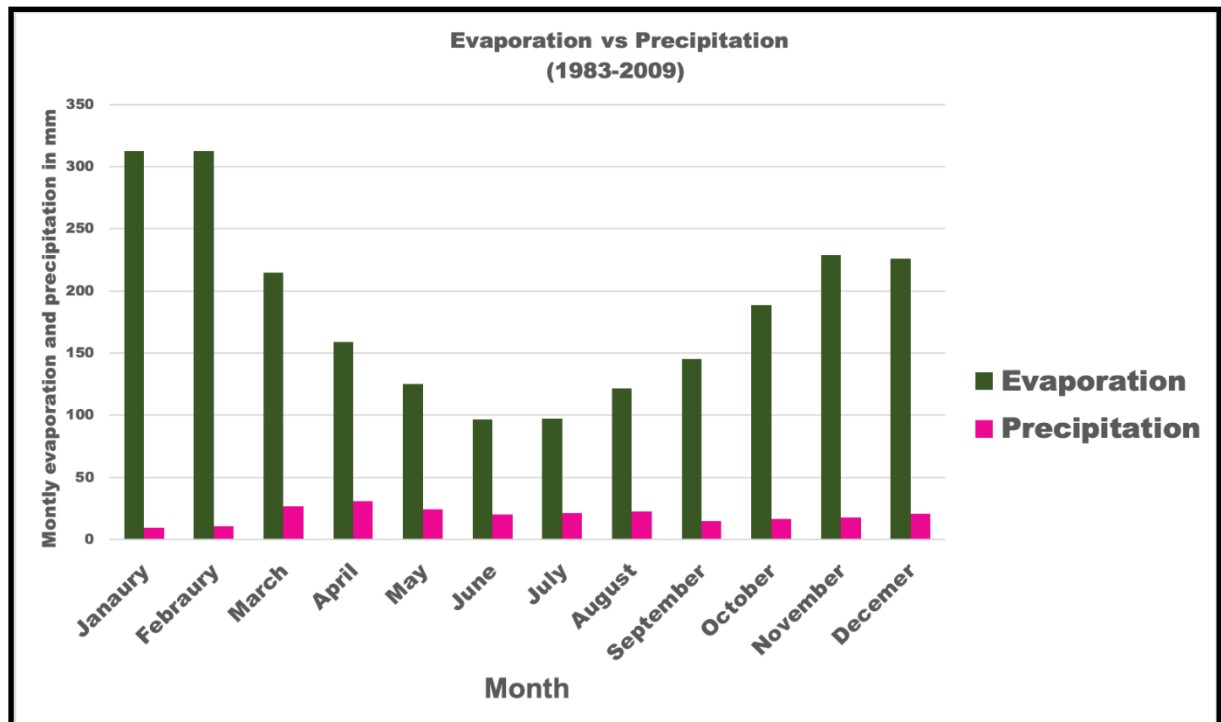


Figure 18: Class A pan-type Monthly evaporation and precipitation data from the year 1983-2009

It is evident that the precipitation rates are exceeded by the evaporation rates for Sutherland, this based on a 26-year trend from data that was recorded by a Class-A type pan in Sutherland. The modelling of the spatiotemporal variability of evapotranspiration and the surface energy balance parameters were done for the summer months (December-January) of 2009-2010. These months represents the extreme conditions of evaporation (Figure 18). In addition, the selection of the modelling period was based on the availability of meteorological data and cloud free Landsat images.

4.2 SPATIOTEMPORAL VARIABILITY OF SURFACE ENERGY BALANCE PARAMETERS

4.2.1 RELATIONSHIP BETWEEN SURFACE TEMPERATURE AND LATENT HEAT FLUX

An indirect relationship between the surface temperature and latent heat flux is prevalent through the energy balance equation (Khaldi *et al.*, 2011). In addition, Surface temperature tends to yield significant information on the status of the surface moisture (Khaldi *et al.*, 2011 and Laounia *et al.*, 2017).

Generally, the analysis of the correlation between the latent heat and surface temperature denotes a good dependency between the two parameters. Three scatterplots for three satellite images were created to determine the relationship between latent heat and surface temperature. All the results were in agreement and yielded a regression of -0.65,

A similar inverse relationship between the latent heat and surface temperature flux has been obtained in other evapotranspiration studies conducted in arid or semi-arid areas. Where, Khaldi *et al.*, (2011) and Laounia *et al.*, (2017) obtained a good regression of -0.945 and -0.92 respectively, between latent heat and surface temperature.

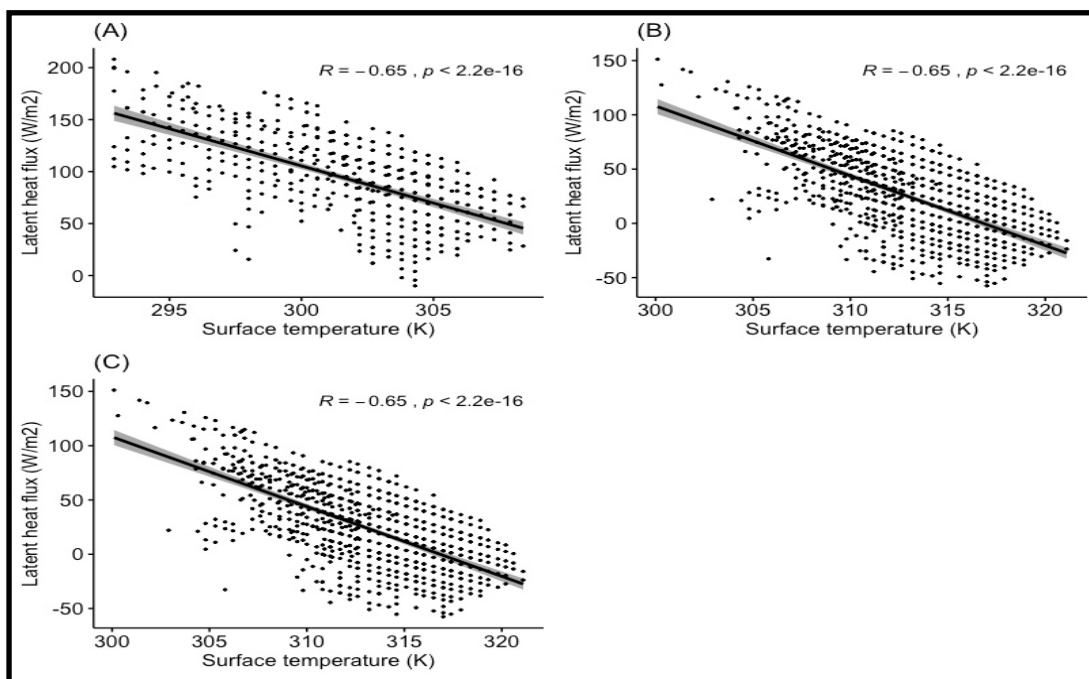


Figure 19: Relationship between surface temperature and latent heat flux obtained with SEBAL

The surface temperature of Figure 20-C represents the highest surface temperature measurement of 322 K, while Figure 20-A represents the lowest surface temperature measurement of 308.4 K. The Southern parts of Sutherland have a lower surface temperature measurements as compared to the Northern parts, Figure 20. This is due to the southern parts of Sutherland being highly characterised by shrub vegetation and the northern parts being characterised by bare soils and urban residential areas. The study of Horvat, (2013) indicates that high surface temperatures values are found in areas with no or scarce vegetation and low surface temperature are found in areas with vegetation. The spatiotemporal variation of the surface temperature is influenced by the view angle of the thermal infrared sensor and the vegetation cover (Numata et al., 2017).

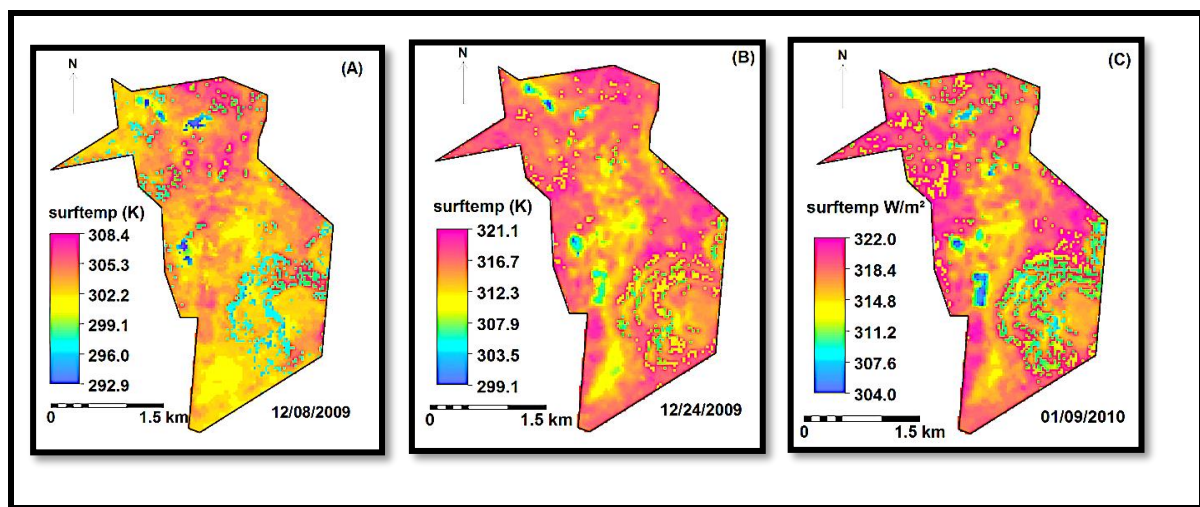


Figure 20: Spatiotemporal measurements of surface temperature estimated with SEBAL for cloud free days on December 4th, 2000; December 24th, 2009; January 09th, 2010.

4.2.2 LATENT HEAT FLUX

The lowest latent heat flux value of 151.177 W/m^2 is depicted in Figure 21-B, while the highest value of 335.849 W/m^2 is depicted in Figure 21-C. The Southern parts of the images represent a higher latent heat flux values compared to the Northern parts, Figure 21. The high values tend to be associated with wet pixels whereas the low values tend to be associated with dry pixels. A direct relationship between latent heat flux measurement and evapotranspiration measurements exists in this study, where the low values of latent heat flux Figure 21-B corresponds with low values of evapotranspiration Figure 26-B

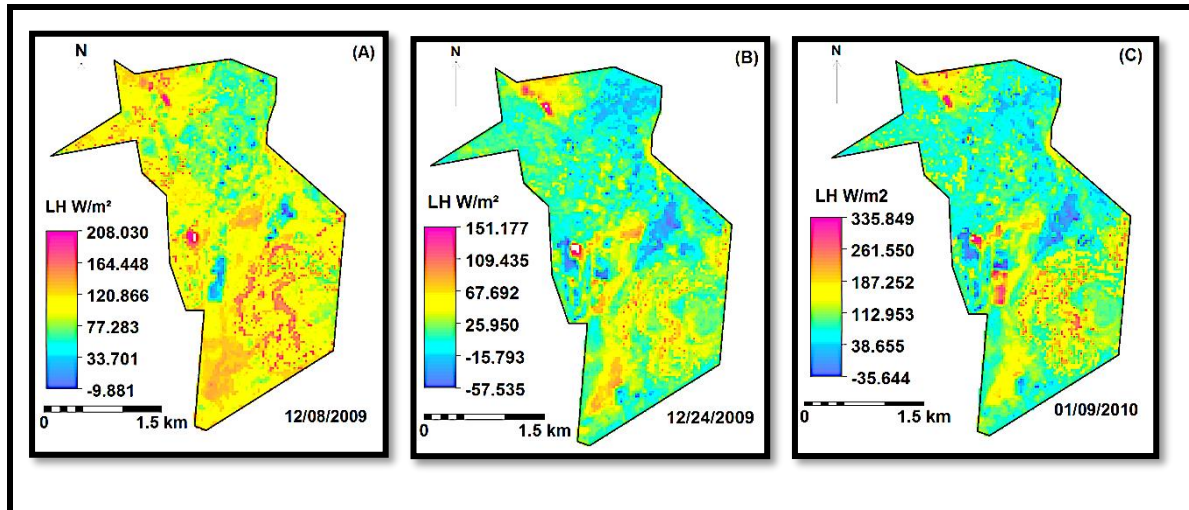


Figure 21: Spatiotemporal measurements of latent heat flux estimated with SEBAL for cloud free days on December 4th, 2000; December 24th, 2009; January 09th, 2010.

4.2.3 SOIL HEAT FLUX

The soil heat flux indicates the amount of energy being released or absorbed at the surface of the soil at a given moment (Roxy *et al.*, 2014). For the image acquired on the 8th of December 2009 the maximum soil heat flux is $47.8659 W/m^2$ and for the image acquired on the 24th of December the maximum soil heat flux value is $38.4084 W/m^2$, with the highest soil heat flux value being on the 9th of January 2010 as $96.7795 W/m^2$ (Figure 22). The high values of soil heat flux are as a result of a rainfall event that occurred a few days before 12th and the 9th of January.

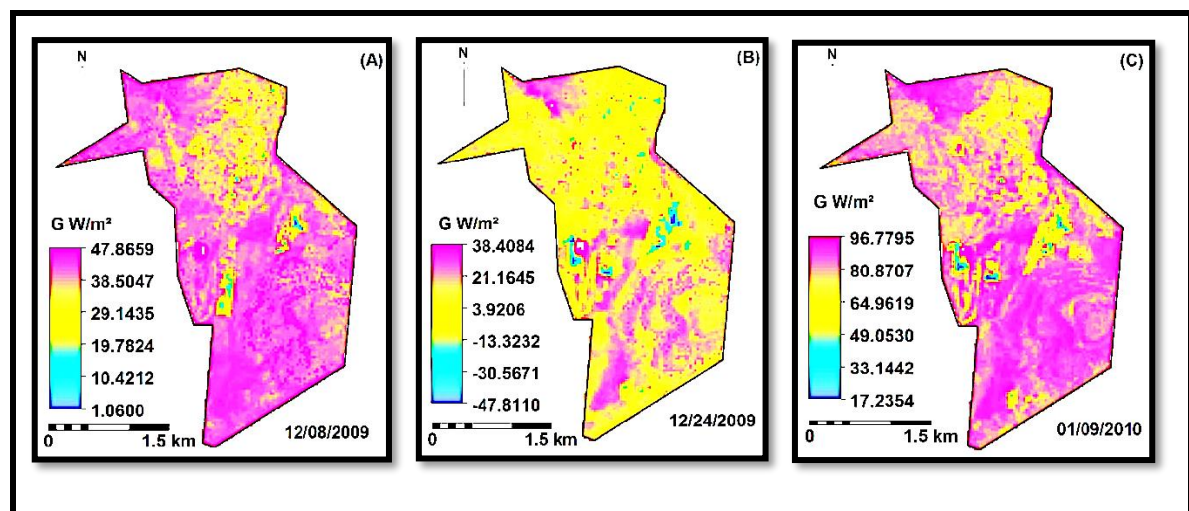


Figure 22: Spatiotemporal measurements of soil heat flux estimated with SEBAL for cloud free days on December 4th, 2000; December 24th, 2009; January 09th, 2010.

The soil heat flux ranged from negative to positive on the 24th of December. The negative values (cooling) indicate that energy is being released into the atmosphere and the positive (warming) values indicate that the fluxes are directed towards the ground (Roxy *et al.*, 2014). The negative soil heat flux values of the image acquired on the 24th of December are normal as similar results have been found in previous research conducted in semi-arid areas (Ogée *et al.*, 2001; Roxy *et al.*, 2014). In the dry soil, less absorption of energy takes place due to the low conductance in the dry soil, as compared to the wet soil (Bala *et al.*, 2016).

4.2.4 RN DAY

The only source of energy for all biological and physical processes existing on the Earth is the radiant energy of the sun (Roxy *et al.*, 2014). Higher values of net radiation are observed on the wet pixels (vegetated areas) and the lower values are associated with dry pixels (bare soils) this is the same trend that was observed in the work of Laounia *et al.*, (2017). The image acquired on the 8th of December has lowest net radiation value of 35.300 W/m² with the highest reading being 154.52 W/m² on the 24th of December 2009 (Figure 23).

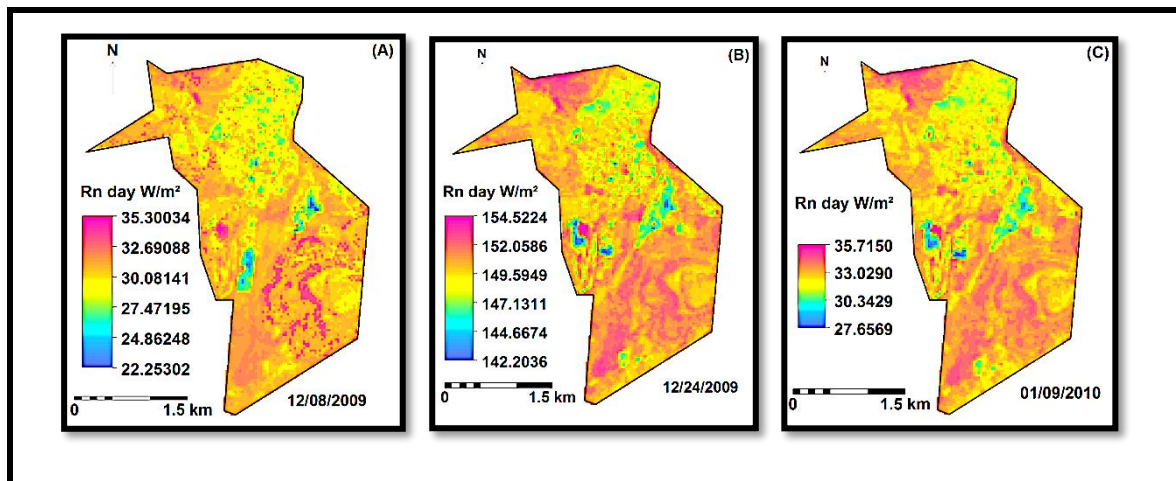


Figure 23: Spatiotemporal measurements of daily net radiation estimated with SEBAL for cloud free days on December 4th, 2000, December 24th, 2009, January 09th, 2010.

4.2.5 NORMALISED DIFFERENCE IN VEGETATION INDEX

Normalised Difference in Vegetation Index which indicates the life green of various vegetation species is a pivotal satellite property for the energy balance model (Roby & Kallarackal, 2017 and Saadi *et al.*, 2018). The NDVI maps depicted in Figure 24 represents the spatial distribution of the NDVI pixel values for Sutherland. According to Kallarackal (2017) the NDVI values should range between -1 and +1. The pixel values for this present study ranges between -0.2 and 0.6, these values fall well within the acceptable NDVI value range. The highest NDVI value of 0.6 is obtained on the 9th of January 2010 and the lowest value of 0.1

is obtained on the 8th of December 2009. The high NDVI values of 0.1, 0.2 and 0.6 can be associated with cultivated commercial land (black circle) and the low NDVI values can be associated with bare soils. In general, the biomass cover of vegetation represented by forests, grasslands and cultivated land can be recognised by higher NDVI values, whereas water and rock bodies can be recognised by low NDVI values (Beg *et al.*, 2016).

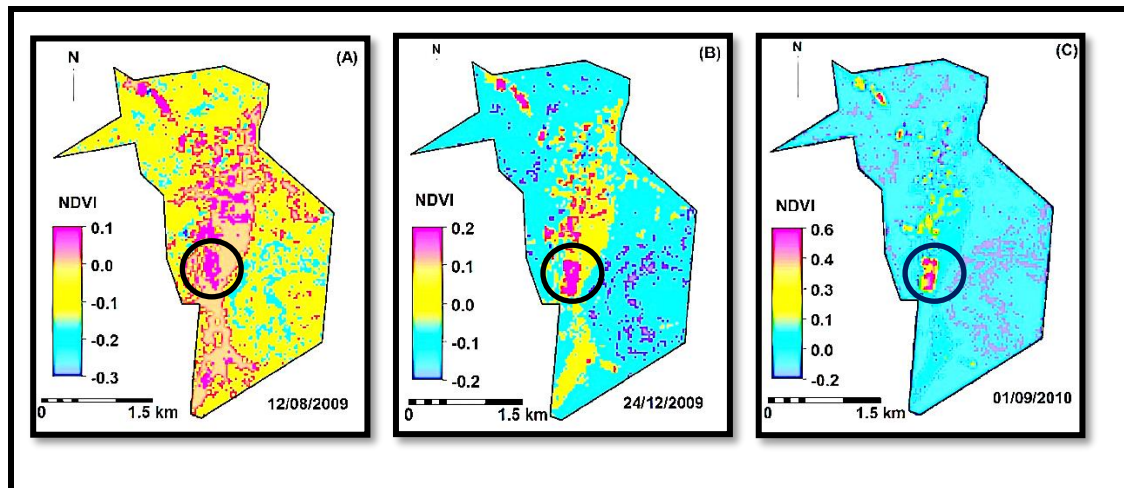


Figure 24: Spatiotemporal measurements of NDVI estimated with SEBAL for cloud free days on December 4th, 2000, December 24th, 2009, January 09th, 2010.

The relationship of surface temperature is not only limited to latent heat and sensible heat exchange process, surface temperature is also influenced by land cover and land use (Effendi, 2012). Vegetation index and surface temperature are two important input parameters in the SEBAL model. The latter parameters which have a strong inverse relationship are used to select the dry/wet pixel (Ruhoff *et al.*, 2012).

According to Nouri *et al.*, (2017), low values of surface temperature corresponds well with high NDVI values (irrigated vegetation). Whereas, high surface temperature values corresponds well with low NDVI values (bare soil). In this study an inverse relationship from full Landsat scenes ($N=106$) was evident for two scatterplots titled B and C, Figure 25. A similar trend has been observed in other evapotranspiration studies (Nouri *et al.*, 2013; Ruhoff *et al.*, 2012).

The low values of surface temperature as depicted indicate areas with well-watered vegetation. Whereas high values of surface temperature indicate areas of bare soil. The scatterplot titled (A), did not yield a strong inverse relationship. This might be due to an error with the selection of the cold and dry pixels while modelling.

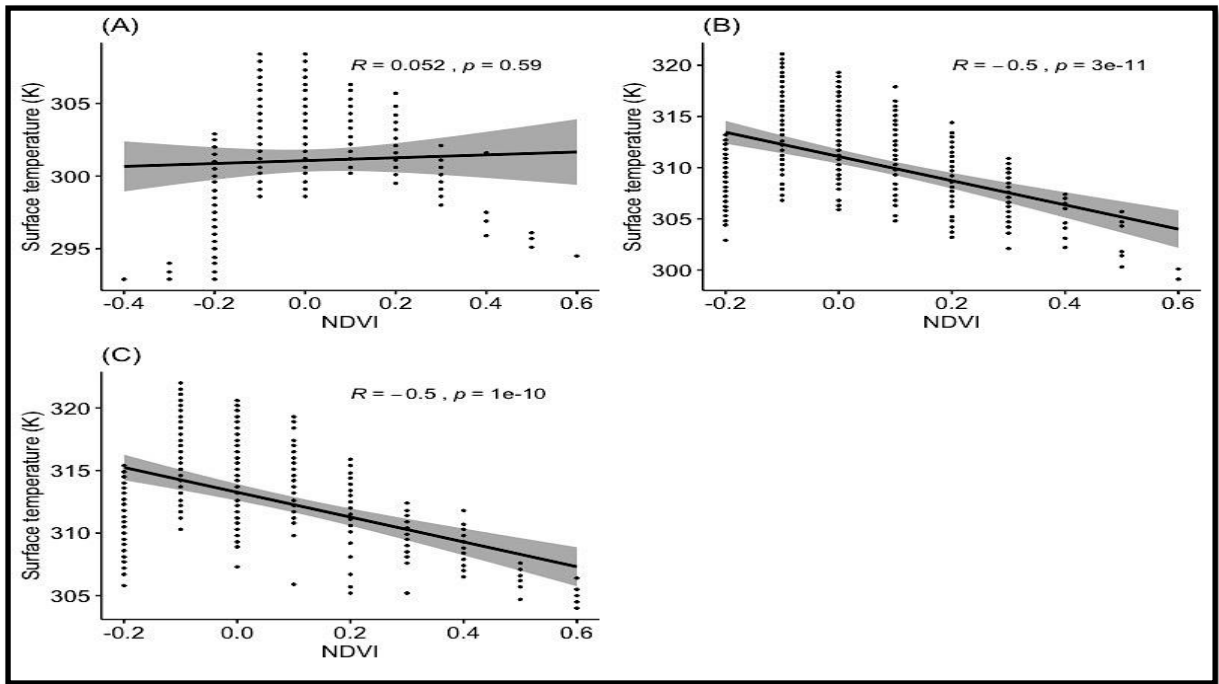


Figure 25: Relationship between NDVI and surface temperature

4.3 SPATIOTEMPORAL VARIABILITY IN EVAPOTRANSPIRATION MEASUREMENTS

The proper quantification of soil moisture content and evapotranspiration are of paramount importance in land management, fire detection, food security research, carbon balance and hydrological modelling (Verstraeten *et al.*, 2008). Due to the spatiotemporal distribution of rainfall and the different irrigation practices in different places, the soil moisture in the root zone will be highly variable for various places (Lin, 2008). Therefore, it is normal to experience a high spatiotemporal variability in terms of evapotranspiration measurements for Sutherland, Figure 26.

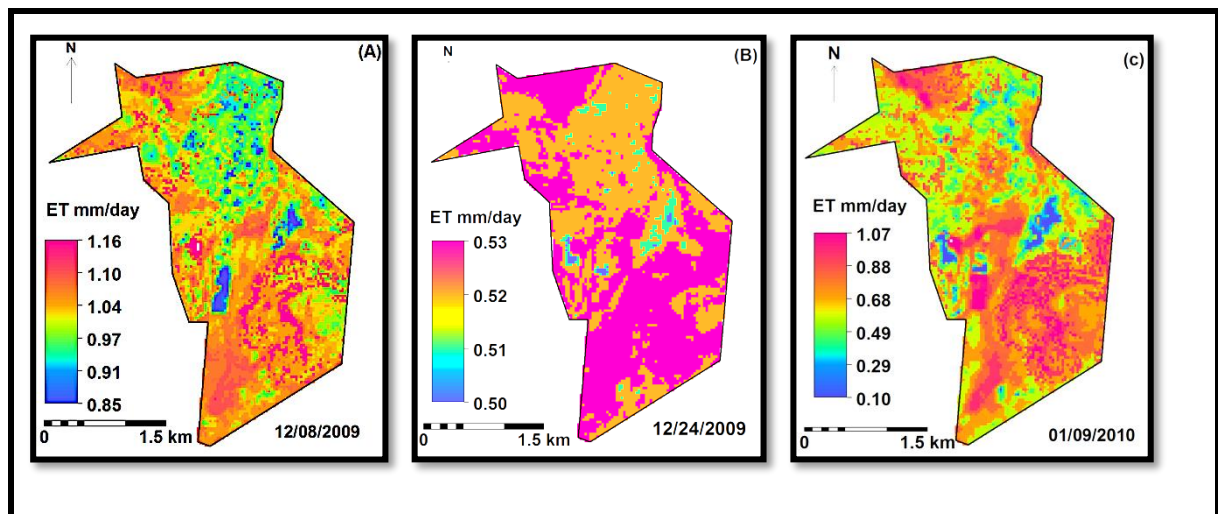


Figure 26: Spatiotemporal measurements of evapotranspiration estimated with SEBAL for cloud free days on December 4th, 2000, December 24th, 2009, January 09th, 2010.

Figure 26-A, has the highest evapotranspiration rate (1.16mm/day) this is potentially related to larger accumulated soil moisture content because of the rainfall event that occurred on the 7th of December 2009. The second highest evapotranspiration rate (1.07mm/day) was measured on the 9th of January 2010. Similar to Figure 26-A the high evapotranspiration rates were influenced by a rainfall event that occurred on 2nd of January.

Leading to the 24th of December there was no rainfall events, resulting in a low soil moisture content and relatively low evapotranspiration rates (0.50-0.53mm/day), Figure 26-B. The high evapotranspiration rates are closely associated with low shrubland and cultivated land. Whereas the low evapotranspiration estimates are closely related to areas with bare soils. The remotely sensed evapotranspiration measurements were validated against ground based evapotranspiration measurements calculated using meteorological data and the ASCE ETSZ equation. The validation allows for the use of remotely sensed data with a high degree of accuracy.

The average daily ET results of SEBAL and ASCE ETSZ for cloud free days during December 2009 and January 2010 are depicted in Figure 27. The SEBAL results shows a good agreement with the ASCE ETSZ results for DOY 358, 0.52mm and 0.29mm respectively. A good agreement between ASCE ETSZ and SEBAL evapotranspiration measurements was also obtained for DOY 09 (0.44m and 0.37mm) except for DOY 342 where the results were not in agreement (0.9mm and 0.3mm). This large difference between SEBAL and ASCE ETSZ is due to the over overestimation of the latent heat flux by SEBAL for DOY 342. The overestimation of the latent heat flux may be caused by the wrong selection of cold and warm pixels in the modelling stages.

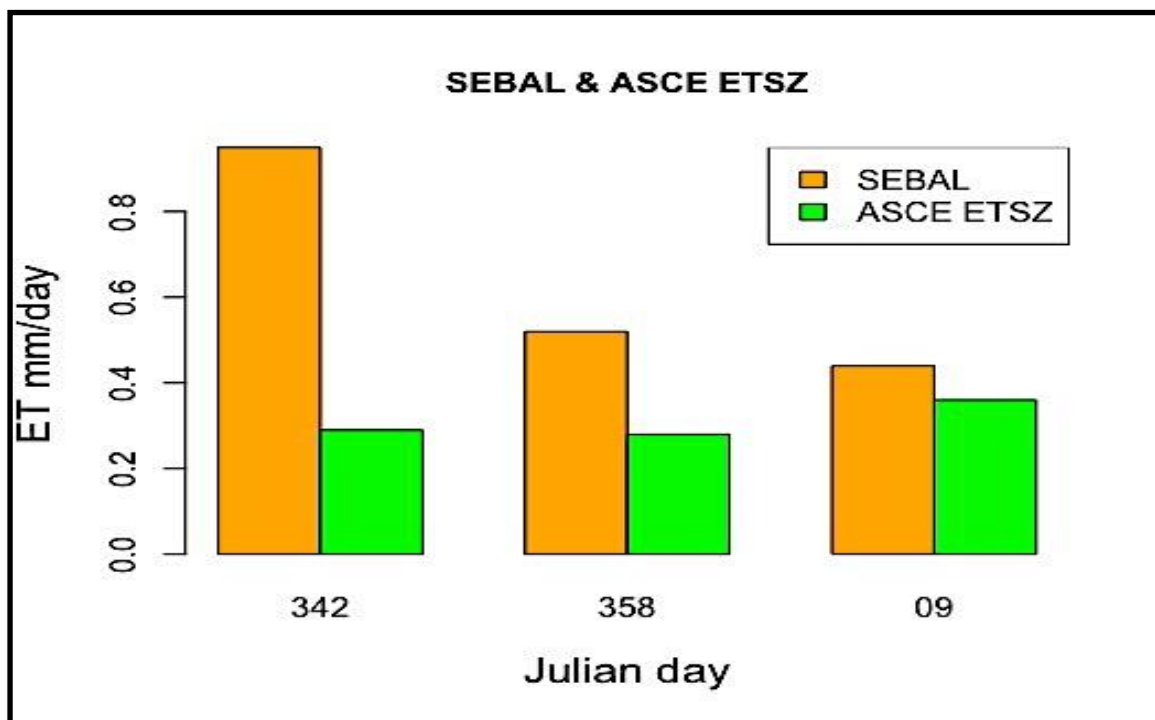


Figure 27: Comparison of the daily evapotranspiration estimated with SEBAL and ASCE ETSZ equation .

5. CONCLUSION AND RECOMMENDATIONS

5.1 RESEARCH SUMMARY AND RECOMMENDATIONS

Well-informed water management relies on accurate estimates of evapotranspiration, yet in many countries the required meteorological data to determine evapotranspiration is very scarce or completely not available. Remote sensed evapotranspiration estimates from satellite data offers an alternative data source, given that it can be validated with point-based estimates (Najmaddin *et al.*, 2017). The aim of this research was to validate satellite-based evapotranspiration measurements with ground based meteorological data. This was achieved by using the pre-packaged SEBAL model in ILWIS. The objectives of this research were limited to:

1. Characterising the rainfall and evaporation data of Sutherland;
2. Assessing and mapping spatiotemporal evapotranspiration measurements by utilizing LANDSAT 7 products, SEBAL model and Integrated Land and Water Information System; and
3. Validating the spatiotemporal evapotranspiration maps acquired through remote sensing techniques with ground based meteorological data, which is used as inputs in the American Society of Civil Engineers Reference Evapotranspiration Equation.

In fulfillment of objective 1, the rainfall and evaporation data was characterised for Sutherland and is presented in Chapter 4.1. The surface energy balance parameters were quantified using the SEBAL pre-package model and ILWIS are represented in chapter 4.2. The surface energy balance parameters were used to determine the spatiotemporal measurements of evapotranspiration which showed considerably variation for the study period. The remotely sensed evapotranspiration measurements were validated against the American Society of Civil Engineers Reference Evapotranspiration equation which utilises meteorological data from a local weather station. However, despite much effort given to the accuracy of the modelling of the surface energy balance parameters. The latent heat flux was overestimated by SEBAL, resulting in the overestimation of remotely sensed evapotranspiration measurements for DOY 342. Therefore, the use of the CIMEX procedure is recommended for the selection of dry and wet pixel which is key in determining accurate estimates of remotely sensed surface energy balance parameters.

5.2 LIMITATIONS

The availability of soil moisture data which could have been used to establish a relationship between soil-moisture and evapotranspiration rates was also a constraint in this study. Generally, this relationship helps with identifying periods of high soil moisture content, which corresponds with high evapotranspiration estimates. The modelling period for this study was only limited for three days due to time constraints, making it difficult to observe the general trend of the spatiotemporal properties of the surface energy balance and evapotranspiration measurements seasonally and annually.

Accurate estimates of evapotranspiration remains a challenge for water resource planners and managers as well as for researchers in the field of hydrology and micrometeorology (Jarman *et al.*, 2009). Evapotranspiration can be measured using empirical formulas and through weather stations, this type of approach is not practical over large scales such as Sutherland. Therefore, it is recommended that a point-based instrument covering a larger spatial area (*e.g.* Scintillometer) be used for future research in Sutherland. This approach might yield a better comparison of the spatiotemporal measurements of evapotranspiration measured by remote-sensing techniques and point-based measurements at a local scale.

5.3 CONTRIBUTION TO THE BODY OF KNOWLEDGE

Evapotranspiration studies have previously focused on regional and field (farming) scales in the Northern Cape (Gwate *et al.*, 2018). This study tries to bridge the gap by looking at the effectiveness of remote sensing techniques in determining spatiotemporal evapotranspiration measurements at a local scale (Sutherland). Physical parameters at local, catchment and regional scales can be represented effectively by satellite based evapotranspiration models, which are also ideal for determining the water use of various vegetation types (Allen *et al.*, 2007). However, it is recommended that an unmanned aerial vehicle be used for water use of vegetation at a field scale. Unmanned aerial vehicles produce imagery at an ultra-fine resolution (1-20cm pixel size) and they provide a good scaling tool between satellite and field data (McCabe *et al.*, 2017).

6. REFERENCE LIST

- Adams, S., Titus, R., Pietersen, K., Tredoux, G., Harris, C., 2001. Hydrochemical characteristics of aquifers near Sutherland in the Western Karoo, South Africa. *J. Hydrol.* 241, 91–103.
- Aeronautics, N., 1972. Landsat 7 Science Data Users Handbook Landsat 7 Science Data Users Handbook.
- Ahmad, M., Biggs, T., Turrall, H., Scott, C.A., 2006. Application of SEBAL approach and MODIS time-series to map vegetation water use patterns in the data scarce Krishna river basin of India 83–90.
- Al-Abbadi, N.M., Rehman, S., 2009. Wind speed and wind power characteristics for gassim, Saudi Arabia. *Int. J. Green Energy* 6, 201–217.
- Alexandris, S.G., Stricevic, R., 2013. Evapotranspiration - An Overview.
- Ali, A., Beg, F., Al-sulttani, A.H., Ochtyra, A., Marcinkowska, A., 2016. Estimation of Evapotranspiration Using SEBAL Algorithm and Landsat-8 Data—A Case Study: Tatra Mountains Region 6, 257–270.
- Ali, H., Khan, E., Sajad, M.A., 2013. Author's personal copy Phytoremediation of heavy metals—Concepts and applications. *Chemosphere* 91, 869–881.
- Allen, Richard G., Pereira, L.S., Raes, D., Smith, M., 1998. Crop evapotranspiration: Guidelines for computing crop requirements. *Irrig. Drain. Pap. No. 56*, FAO 300.
- Allen, Richard G, Pereira, L.S., Raes, D., Smith, M., Ab, W., 1998. Crop evapotranspiration - Guidelines for computing crop water requirements - FAO Irrigation and drainage paper 56 By 1–15.
- Allen, R.G., Tasumi, M., Morse, a, Trezza, R., 2005. A Landsat-based energy balance andevapotranspiration model in Western USwater rights regulation and planning. *Irrig. Drain. Syst.* 19, 251–268.
- Anderson, M., 1999. High Overhead : ET Measurement via Remote Sensing 2004–2006.
- Anderson, M.C., Norman, J.M., Kustas, W.P., Houborg, R., Starks, P.J., Agam, N., 2008. A thermal-based remote sensing technique for routine mapping of land-surface carbon, water and energy fluxes from field to regional scales. *Remote Sens. Environ.* 112, 4227–4241.
- Anderson, M.C., Norman, J.M., Mecikalski, J.R., Otkin, J.A., Kustas, W.P., 2007. A climatological study of evapotranspiration and moisture stress across the continental

- United States based on thermal remote sensing: 1. Model formulation. *J. Geophys. Res. Atmos.* 112, 1–17.
- Asner, G.P., Scurlock, J.M.O., Hicke, J. a, 2003. Global synthesis of leaf area index observations : *Glob. Ecol. Biogeogr.* 12, 191–205.
- Bala, A., Rawat, K.S., Misra, A.K., Srivastava, A., 2016. Assessment and validation of evapotranspiration using SEBAL algorithm and Lysimeter data of IARI agricultural farm, India. *Geocarto Int.* 31, 739–764.
- Bala, S.K., 2010. Assessment of Crop Water Deficit and Estimation of Yield of Wheat in Greater Dinajpur Region Using MODIS Data FINAL REPORT Assessment of Crop Water Deficit and Estimation of Yield of Wheat FINAL REPORT.
- Baret, F., Jacquemoud, S., Hanocq, J.F., 1993. About the soil line concept in remote sensing. *Adv. Sp. Res.* 13, 281–284.
- Bastiaanssen, W., Thoreson, B., Clark, B., Davids, G., 2010. Discussion of “Application of SEBAL Model for Mapping Evapotranspiration and Estimating Surface Energy Fluxes in South-Central Nebraska” by Ramesh K. Singh, Ayse Irmak, Suat Irmak, and Derrel L. Martin. *J. Irrig. Drain. Eng.* 136, 282–283.
- Bastiaanssen, W.G.M., 1995. Regionalization of surface flux densities and moisture indicators in composite terrain: a remote sensing approach under clear skies in Mediterranean climates, Doctoral thesis, Wageningen Agricultural University, Wageningen The Netherlands.
- Bastiaanssen, W.G.M., Ahmad, M.-D., Chemin, Y., 2002. Satellite surveillance of evaporative depletion across the Indus Basin. *Water Resour. Res.* 38, 9-1-9–9.
- Bastiaanssen, W.G.M., Menenti, M., Feddes, R.A., Holtslag, A.A.M., 1998a. A remote sensing surface energy balance algorithm for land (SEBAL) 213, 198–212.
- Bastiaanssen, W.G.M., Noordman, E.J.M., Pelgrum, H., Davids, G., Thoreson, B.P., Allen, R.G., 2005. SEBAL Model with Remotely Sensed Data to Improve Water-Resources Management under Actual Field Conditions 85–93.
- Bastiaanssen, W.G.M., Pelgrum, H., Wang, J., Ma, Y., Moreno, J.F., 1998b. A remote sensing surface energy balance algorithm for land (SEBAL) 213, 213–229.
- Benites, J., Castellanos, A., 2015. Improving soil moisture with conservation agriculture.
- Bethenod, O., Katerji, N., Goujet, R., Bertolini, J.M., Rana, G., 2000. Determination and validation of corn crop transpiration by sap flow measurement under field conditions.

- Theor. Appl. Climatol. 67, 153–160.
- Bilt, D., Kustas, W.P., Norman, J.M., 1996. Use of remote sensing for evapotranspiration monitoring over land surfaces. *Hydrol. Sci. J.* 41, 495–516.
- Blumler, M., 2005. Three Conflated Definitions of Mediterranean Climates. *Middle States Geogr.* 38, 52–60.
- Blyth, Dolman, n.d. blyth_z0h_JAM.pdf.
- Bouman, B.A.M., 2007. A conceptual framework for the improvement of crop water productivity at different spatial scales. *Agric. Syst.* 93, 43–60.
- Brock, B.W., Willis, I.C., Sharp, M.J., 2000. Measurement and parameterisation of albedo variations at Haut Glacier d' Arolla, Switzerland. *J. Glaciol.* 46, 675–688.
- Brown, P., 2000. Basics of Evaporation and Evapotranspiration. Univ. Arizona Coop. Ext. 1–4.
- Campillo, C., Fortes, R., Prieto, H., n.d. Solar Radiation Effect on Crop Production.
- Chander, G., Markham, B., 2003. Revised Landsat-5 TM Radiometric Calibration Procedures and Postcalibration Dynamic Ranges. *IEEE Trans. Geosci. Remote Sens.* 41, 2674–2677.
- Chen, Q., Jia, L., Hutjes, R., Menenti, M., 2015. Estimation of aerodynamic roughness length over oasis in the heihe river basin by utilizing remote sensing and ground data. *Remote Sens.* 7, 3690–3709.
- Cordova, M., Carrillo-Rojas, G., Crespo, P., Wilcox, B., Celleri, R., 2015. Evaluation of the Penman-Monteith (FAO 56 PM) Method for Calculating Reference Evapotranspiration Using Limited Data Application to the Wet Paramo of Southern Ecuador. *Mt. Res. Dev.* 35, 230–239.
- Courault, D., Seguin, B., Olioso, A., 2003. Review to estimate Evapotranspiration from remote sensing data: some examples from the simplified relationship to the use of mesoscale atmospheric models. 1–18.
- Cow, I.R., Ton, H.T.O.U.G., 1971. The Relative Role of Stomata in Transpiration and Assimilation * The mean rate of evaporation per unit area of lamina is 336, 325–326.
- Cristóbal, J., Prakash, A., Anderson, M.C., Kustas, W.P., Euskirchen, E.S., Kane, D.L., 2017. Estimation of surface energy fluxes in the Arctic tundra using the remote sensing thermal-based Two-Source Energy Balance model. *Hydrol. Earth Syst. Sci.* 21, 1339–1358.

- Danodia, A., Patel, N.R., Chol, C.W., Nikam, B.R., Sehgal, V.K., 2017. Application of S-SEBI model for crop evapotranspiration using Landsat-8 data over parts of North India. *Geocarto Int.* 6049, 1–18.
- Diffenbaugh, N.S., Swain, D.L., Touma, D., 2015. Anthropogenic warming has increased drought risk in California. *Proc. Natl. Acad. Sci.* 112, 3931–3936.
- Dingman-Physical Hydrology-Chapter 3.pdf, n.d.
- Dodds, P., Meyer, W., Barton, A., 2005. A Review of Methods to Estimate Irrigated Reference Crop Evapotranspiration across Australia. *CRC Irrig. Futur. Tech. Rep.* 54.
- Dye, P., 2013. A review of changing perspectives on Eucalyptus water-use in South Africa. *For. Ecol. Manage.* 301, 51–57.
- E, S., A, B., Waters, R., Trezza, R., 2002. *S e b a l* 1–97.
- Effendi, I., 2012. Evapotranspiration in Dry Climate Area: Comparing Remote Sensing Techniques With Unsaturated Zone Water Flow Simulation Evapotranspiration in Dry Climate Area : Comparing Remote Sensing Techniques With Unsaturated Zone Water.
- Engelbrecht, C.J., Engelbrecht, F.A., 2016. Shifts in Köppen-Geiger climate zones over southern Africa in relation to key global temperature goals. *Theor. Appl. Climatol.* 123, 247–261.
- Engelbrecht, F., Adegoke, J., Bopape, M.-J., Naidoo, M., Garland, R., Thatcher, M., McGregor, J., Katzfey, J., Werner, M., Ichoku, C., Gatebe, C., 2015. Projections of rapidly rising surface temperatures over Africa under low mitigation. *Environ. Res. Lett.* 10, 085004.
- Farooq Ahmad, 2012. Spectral vegetation indices performance evaluated for Cholistan Desert. *J. Geogr. Reg. Plan.* 5, 165–172.
- Ferreira, M.I., Valancogne, C., Daudet, F. a, Ameglio, T., Pacheco, C. a, Michaelsen, J., 1996. Evapotranspiration and crop-water relations in a peach orchard. *Evapotranspiration Irrig. Sched.* 61–68.
- Fisher, J.B., Debiase, T.A., Qi, Y., Xu, M., Goldstein, A.H., 2005. Evapotranspiration models compared on a Sierra Nevada forest ecosystem 20.
- Fu, Q., 2003. Radiation (Solar). *Radiat. (SOLAR). Proc. IEEE* 63, 1859–1863.
- Gao, Z.Q., Liu, C.S., Gao, W., Chang, N.B., 2011. A coupled remote sensing and the Surface Energy Balance with Topography Algorithm (SEBTA) to estimate actual evapotranspiration over heterogeneous terrain. *Hydrol. Earth Syst. Sci.* 15, 119–139.

- Ghulam, A., 2010. Calculating surface temperature using Landsat thermal imagery. *Calc. Surf. Temp. using Landsat Therm. Imag.* 1, 1–9.
- Gibson, L., Jarman, C., Su, Z., Eckardt, F.E., 2013. Estimating evapotranspiration using remote sensing and the Surface Energy Balance System - a South African perspective : review. *Water SA* 39, 477–484.
- Gibson, L.A., 2013. THE APPLICATION OF THE SURFACE ENERGY BALANCE SYSTEM MODEL TO ESTIMATE EVAPOTRANSPIRATION IN SOUTH AFRICA.
- Gibson, L.A., Jarman, C., Su, Z., Eckardt, F.E., 2013. Estimating evapotranspiration using remote sensing and the Surface Energy Balance System – A South African perspective 39, 477–484.
- Gilabert, M.A., González-Piqueras, J., García-Haro, F.J., Meliá, J., 2002. A generalized soil-adjusted vegetation index. *Remote Sens. Environ.* 82, 303–310.
- Gill, T., Punt, C., 2010. The potential impact of increased irrigation water tariffs in South Africa. *African Assoc. Agric. Econ. Assoc. South Africa Conf.*
- Gitelson, A.A., Viña, A., Arkebauer, T.J., Rundquist, D.C., Keydan, G., Leavitt, B., 2003. Remote estimation of leaf area index and green leaf biomass in maize canopies. *Geophys. Res. Lett.* 30, n/a-n/a.
- Glenn, E.P., Huete, A.R., Nagler, P.L., Hirschboeck, K.K., Brown, P., 2007. Integrating remote sensing and ground methods to estimate evapotranspiration. *CRC. Crit. Rev. Plant Sci.* 26, 139–168.
- Govaerts, B., Verhulst, N., 2010. The Normalized Difference Vegetation Index (NDVI) GreenSeeker TM Handheld Sensor: Toward Integrated Evaluation of Crop Management. Part B: User Guide. *Cimmyt* 12.
- Gowda, P.H., Chávez, J.L., Colaizzi, P.D., Evett, S.R., Howell, T.A., Tolk, J.A., 2007. Remote sensing based energy balance algorithms for mapping ET: current status and future challenges. *Am. Soc. Agric. Biol. Eng.* 50, 1639–1644.
- Gowda, P.H., Howell, T.A., Paul, G., Colaizzi, P.D., Marek, T.H., 2011. Sebal for Estimating Hourly ET Fluxes Over Irrigated and Dryland Cotton During BEAREX08. *World Environ. Water Resour. Congr.* 41173, 2787–2795.
- Hadjimitsis, D.G., Papadavid, G., 2011. Remote Sensing for Determining Evapotranspiration and Irrigation Demand for Annual Crops 25–56.

- Hassan-esfahani, L., Torres-rua, A., Mckee, M., 2015. Assessment of optimal irrigation water allocation for pressurized irrigation system using water balance approach , learning machines , and remotely sensed data. *Agric. Water Manag.* 153, 42–50.
- Hassan-esfahani, L., Torres-rua, A., Ticlavilca, A.M., Jensen, A., Mckee, M., 2014. TOPSOIL MOISTURE ESTIMATION FOR PRECISION AGRICULTURE USING UNMMANED. 2014 IEEE Geosci. Remote Sens. Symp. 3263–3266.
- Hatfield, J.L., Prueger, J.H., 2010. Value of using different vegetative indices to quantify agricultural crop characteristics at different growth stages under varying management practices. *Remote Sens.* 2, 562–578.
- Hatzianastassiou, N., Matsoukas, C., Fotiadi, A., Pavlakis, K.G., Drakakis, E., Hatzidimitriou, D., Vardavas, I., 2005. Global distribution of Earth's surface shortwave radiation budget. *Atmos. Chem. Phys.* 5, 2847–2867.
- Hedden, S., Cilliers, J., 2014. Parched prospects: The emerging water crisis in South Africa. *Water Wheel* 13, 42–47.
- Hendrikse, J., 2000. Geostatistics in ILWIS XXXIII, 365–375.
- Horvat, B., 2013. Spatial dynamics of actual daily evapotranspiration. *Gradevinar* 65, 693–705.
- Houghton JT, Y, D., DJ, G., M, N., PJ, van der L., X, D., K, M., C, J., 2001. Climate Change 2001: The Scientific Basis. *Clim. Chang.* 2001 Sci. Basis 881.
- Hsiao, B.T., Xu, L., 2005. Evapotranspiration and Relative Contribution by the Soil and the Plant Evapotranspiration and Relative Contribution by the Soil and the Plant. *Water Use* 4, 129–154.
- Huete, A., Didan, K., Miura, H., Rodriguez, E.P., Gao, X., Ferreira, L.F., 2002. Overview of the radiometric and biophysical performance of the MODIS vegetation indices. *Remote Sens. Environ.* 83, 195–213.
- Huete, A.R., 1988. A soil-adjusted vegetation index (SAVI). *Remote Sens. Environ.* 25, 295–309.
- Huntington, T.G., 2006. Evidence for intensification of the global water cycle: Review and synthesis. *J. Hydrol.* 319, 83–95.
- Hurk, B. Van Den, 2001. Energy balance based surface flux estimation from satellite data, and its application for surface moisture assimilation. *Meteorol. Atmos. Phys.* 52, 43–52.

- Immerzeel, W.W., Droogers, P., Gieske, A., 2006. Remote Sensing and Evapotranspiration Mapping : State of the Art 39.
- International Federation of Red Cross, 2004. South Africa: Drought 2004, Bulletin No. 1.
- Jackson, R.D.; Idso, S.B.; Reginato, R.J.; Pinter, J., 1981. Canopy temperature as a crop stress indicator.pdf. Water Resour. Res.
- Jacob, F., Olioso, A., Gu, X.F., Su, Z., Seguin, B., 2002. Mapping surface fluxes using airborne visible, near infrared, thermal infrared remote sensing data and a spatialized surface energy balance model. *Agronomie* 22, 669–680.
- Jansen, J., Stive, P.M., van de Giesen, N., Tyler, S., Steele-Dunne, S.C., Williamson, L., 2011. Estimating soil heat flux using Distributed Temperature Sensing. *GRACE, Remote Sens. Ground-based Methods Multi-Scale Hydrol.* 140–144.
- Jato-Espino, D., Charlesworth, S.M., Perales-Momparler, S., Andrés-Doménech, I., 2017. Prediction of Evapotranspiration in a Mediterranean Region Using Basic Meteorological Variables. *J. Hydrol. Eng.* 22, 04016064.
- Jia, D.U., Kaishan, S., Zongming, W., Bai, Z., Dianwei, L.I.U., 2013. Evapotranspiration Estimation Based on MODIS Products and Surface Energy Balance Algorithms for Land (SEBAL) Model in Sanjiang Plain , Northeast China 23, 73–91.
- Jin, X., Guo, R., Xia, W., 2013. Distribution of actual evapotranspiration over Qaidam basin, an Arid area in China. *Remote Sens.* 5, 6976–6996.
- Jovanovic, N., Mu, Q., Bugan, R.D.H., Zhao, M., 2015. Dynamics of MODIS evapotranspiration in South Africa 41, 79–90.
- Junges, A.H., Fontana, D.C., Anzanello¹, R., Bremm, C., 2017. Normalized difference vegetation index obtained by ground-based remote sensing to characterize vine cycle in Rio Grande do Sul, Brazil. *Ciência e Agrotecnologia* 41, 543–553.
- K.M.P.S.Bandara, 2006. Assessing irrigation performance by using remote sensing.
- Kabat, P., Dolman, A.J., Elbers, J.A., 1997. Evaporation, sensible heat and canopy conductance of fallow savannah and patterned woodland in the Sahel. *J. Hydrol.* 188–189, 494–515.
- Kalma, J., McVicar, T., McCabe, M.F., 2008. Estimating Land Surface Evaporation : A Review of Methods Using Remotely Sensed Surface Temperature Data. *Surv Geophys* 421–469.

- Kalma, J.D., McVicar, T.R., McCabe, M.F., 2008. Estimating land surface evaporation: A review of methods using remotely sensed surface temperature data. *Surv. Geophys.* 29, 421–469.
- Kang, Y., Khan, S., Ma, X., 2009. Climate change impacts on crop yield , crop water productivity and food security – A review. *Prog. Nat. Sci.* 19, 1665–1674.
- Karimi, P., Bastiaanssen, W.G.M., 2015. Spatial evapotranspiration, rainfall and land use data in water accounting - Part 1: Review of the accuracy of the remote sensing data. *Hydrol. Earth Syst. Sci.* 19, 507–532.
- Katul, G.G., Parlange, M.B., 1992. A Penman-Brutsaert Model for wet surface evaporation. *Water Resour. Res.*
- Khalidi, A, Hamimed, A, Mederbal, K and Seddini, A., 2011. OBTAINING EVAPOTRANSPIRATION AND SURFACE ENERGY FLUXES WITH REMOTELY SENSED DATA TO IMPROVE AGRICULTURAL WATER MANAGEMENT 11, 4558–4581.
- Kiptala, J.K., Mohamed, Y., Mul, M.L., Van Der Zaag, P., 2013a. Mapping evapotranspiration trends using MODIS and SEBAL model in a data scarce and heterogeneous landscape in Eastern Africa. *Water Resour. Res.* 49.
- Kiptala, J.K., Mohamed, Y., Mul, M.L., Van Der Zaag, P., 2013b. Mapping evapotranspiration trends using MODIS and SEBAL model in a data scarce and heterogeneous landscape in Eastern Africa. *Water Resour. Res.* 49, 8495–8510.
- Kogan, F.N., 1999. Operational Space Technology for Global Vegetation Assessment.
- Kosa, P., 2003. The Effect of Temperature on Actual Evapotranspiration based on Landsat 5 TM Satellite Imagery 56.
- Kundu, A., Chatterjee, S., Dutta, D., Siddiqui, A.R., 2015. Meteorological Trend Analysis in Western Rajasthan (India) using Geographical Information System and Statistical Techniques. *J. Environ. Earth Sci.* 5, 90–100.
- Kustas, W., Anderson, M., 2009. Advances in thermal infrared remote sensing for land surface modeling. *Agric. For. Meteorol.* 149, 2071–2081.
- KUSTAS, W.P., NORMAN, J.M., 1996. Use of remote sensing for evapotranspiration monitoring over land surfaces. *Hydrol. Sci. J.* 41, 495–516.

- Laounia, N., Abderrahmane, H., Abdelkader, K., Zahira, S., Mansour, Z., 2017. Evapotranspiration and Surface Energy Fluxes Estimation Using the Landsat-7 Enhanced Thematic Mapper Plus Image over a Semiarid Agrosystem in the North-West of Algeria. *Rev. Bras. Meteorol.* 32, 691–702.
- Lawrence, Thorto, 2006. The Partitioning of Evapotranspiration into Transpiration , Soil Evaporation , and Canopy Evaporation in a GCM: Impacts on Land – Atmosphere Interaction 862–880.
- Lee, K.-H., Cho, H.-Y., 2012. Simple Method for Estimating Pan Coefficients: Conversion of Pan Evaporation to Reference Evapotranspiration. *J. Irrig. Drain. Eng.* 138, 98–103.
- Lee, Y., Kim, S., 2016. The modified SEBAL for mapping daily spatial evapotranspiration of South Korea using three flux towers and Terra MODIS data. *Remote Sens.* 8.
- Li, Z., Tang, R., Wan, Z., Bi, Y., Zhou, C., Tang, B., Yan, G., Zhang, X., 2009. A Review of Current Methodologies for Regional Evapotranspiration Estimation from Remotely Sensed Data 3801–3853.
- Liang, S., Member, S., Wang, K., Zhang, X., Wild, M., 2010. Review on Estimation of Land Surface Radiation and Energy Budgets From Ground Measurement , Remote Sensing and Model Simulations 3, 225–240.
- Liou, Y.A., Kar, S.K., 2014. Evapotranspiration estimation with remote sensing and various surface energy balance algorithms-a review. *Energies* 7, 2821–2849.
- Long, D., Singh, V.P., 2012. A modified surface energy balance algorithm for land (M-SEBAL) based on a trapezoidal framework. *Water Resour. Res.* 48.
- Long, D., Singh, V.P., Li, Z.L., 2011. How sensitive is SEBAL to changes in input variables, domain size and satellite sensor? *J. Geophys. Res. Atmos.* 116, 1–20.
- Lu, L., Kuenzer, C., Wang, C., Guo, H., Li, Q., 2015. Evaluation of three MODIS-derived vegetation index time series for dryland vegetation dynamics monitoring. *Remote Sens.* 7, 7597–7614.
- Lyon, B., Dewitt, D.G., 2012. A recent and abrupt decline in the East African long rains. *Geophys. Res. Lett.* 39, 1–5.
- Maeda, E.E., Wiberg, D.A., Pellikka, P.K.E., 2011. Estimating reference evapotranspiration using remote sensing and empirical models in a region with limited ground data availability in Kenya. *Appl. Geogr.* 31, 251–258.

- Mahed, G. 2006. Development of a conceptual geohydrological model for a fractured rock aquifer in the Karoo, near Sutherland, South Africa
- Majozi, N.P., Mannaerts, C.M., Ramoelo, A., Mathieu, R., Mudau, A.E., Verhoef, W., 2017. An intercomparison of satellite-based daily evapotranspiration estimates under different eco-climatic regions in South Africa. *Remote Sens.* 9, 1–21.
- Masek, J.G., Honzak, M., Goward, S.N., Liu, P., Pak, E., 2001. Landsat-7 ETM + as an observatory for land cover Initial radiometric and geometric comparisons with Landsat-5 Thematic Mapper 78, 118–130.
- Matsuda, Y., Fujita, K., Ageta, Y., Sakai, A., 2006. Estimation of atmospheric transmissivity of solar radiation from precipitation in the Himalaya and the Tibetan Plateau. *Ann. Glaciol.* 43, 344–350.
- Maurer, K.D., Hardiman, B.S., Vogel, C.S., Bohrer, G., 2013. Canopy-structure effects on surface roughness parameters: Observations in a Great Lakes mixed-deciduous forest. *Agric. For. Meteorol.* 177, 24–34.
- McCabe, M.R., Alsdorf, D.E., Miralles, D.G., Uijlenhoet, R., Wagner, W., Lucieer, A., Houborg, R., Niko E. C. Verhoest, Trenton E. Franz, J.S., Gao, H., Wood, E.F., 2017. The Future of Earth Observation in Hydrology. *Hydrology and Earth System Sciences (under review)*. *Hydrol. Earth Syst. Sci.* (under Rev. 3879–3914.
- McJannet, D.L., Cook, F.J., McGloin, R.P., McGowan, H.A., Burn, S., 2011. Estimation of evaporation and sensible heat flux from open water using a large-aperture scintillometer. *Water Resour. Res.* 47, 1–14.
- McMahon, T.A., Peel, M.C., Lowe, L., Srikanthan, R., McVicar, T.R., 2013. Estimating actual, potential, reference crop and pan evaporation using standard meteorological data: A pragmatic synthesis. *Hydrol. Earth Syst. Sci.* 17, 1331–1363.
- Melesse, A., Weng, Q., Prasad, S., Senay, G., 2007. Remote Sensing Sensors and applications in environmental resources mapping and modelling. *Sensors* 7, 3209–3241.
- Menon, S., Hansen, J., Nazarenko, L., Luo, Y., 2002. Climate Effects of Black Carbon Aerosols in China and India. *Science (80-)*. 297, 2250–2253.
- Mkwanazi, 2014. DEVELOPING A MODIFIED SEBAL ALGORITHM THAT IS RESPONSIVE TO ADVECTION BY USING LIMITED WEATHER DATA.
- Mölg, T., Cullen, N.J., Kaser, G., 2009. Solar radiation, cloudiness and longwave radiation over low-latitude glaciers: Implications for mass-balance modelling. *J. Glaciol.* 55, 292–

- Mróz, M., Sobieraj, A., 2004. Comparison of several vegetation indices calculated on the basis of a seasonal SPOT XS time series, and their suitability for land cover and agricultural crop identification. *Tech. Sci.* 7, 39–66.
- Mucina, L., Juergens, N., Le Roux, A., Rutherford, M.C., Schmiedel, U., Esler, K.J., Powrie, L.W., Desmet, P.G., Milton, S.J., 2006. Succulent Karoo Biome. *Veg. South Africa, Lesotho Swaziland. Strelitzia* 19 19, 220–299.
- Mukheirbir, P., Sparks, D., 2005. Climate variability, climate change and water resource strategies for small municipalities 81.
- Najmaddin, P.M., Whelan, M.J., Balzter, H., 2017. Estimating daily reference evapotranspiration in a semi-arid region using remote sensing data. *Remote Sens.* 9.
- Norman, J.M., Kustas, W.P., Humes, K.S., 1995. Source approach for estimating soil and vegetation energy fluxes in observations of directional radiometric surface temperature. *Agric. For. Meteorol.* 77, 263–293.
- Nouri, H., Beecham, S., Kazemi, F., Hassanli, A.M., Anderson, S., 2013. Remote sensing techniques for predicting evapotranspiration from mixed vegetated surfaces. *Hydrol. Earth Syst. Sci. Discuss.* 10, 3897–3925.
- Numata, I., Khand, K., Kjaersgaard, J., Cochrane, M.A., Silva, S.S., 2017. Evaluation of landsat-based metric modeling to provide high-spatial resolution evapotranspiration estimates for amazonian forests. *Remote Sens.* 9.
- Nutini, F., Boschetti, M., Candiani, G., Bocchi, S., Brivio, P.A., 2014. Evaporative fraction as an indicator of moisture condition and water stress status in semi-arid rangeland ecosystems. *Remote Sens.* 6, 6300–6323.
- Ogée, J., Lamaud, E., Brunet, Y., 2001. A long-term study of soil heat flux under a forest canopy. *Agric. For. Meteorol.* 106, 173–186.
- Ogunode, A., Akombelwa, M., 2017. An algorithm to retrieve Land Surface Temperature using Landsat-8 Dataset 6, 262–276.
- Oki, T., Kanae, S., 2006. Global Hydrological Cycles and World Water Resources. *Science (80-)*. 313, 1068–1072.
- Opoku-Duah, S., Donoghue, D.N.M., Burt, T.P., 2008. Intercomparison of evapotranspiration over the Savannah Volta Basin in West Africa using remote sensing data. *Sensors* 8,

2736–2761.

- Papadavid, G., Neocleous, D., Kountios, G., Markou, M., Michailidis, A., Ragkos, A., Hadjimitsis, D., 2017. Using SEBAL to Investigate How Variations in Climate Impact on Crop Evapotranspiration. *J. Imaging* 3, 30.
- Parlange, Marc B. and Katul, G.G., 1995. Watershed scale shear stress from thethersonde wind profile measurements under near neutral and unstable atmopsheric stability.
- Paul, G., Aiken, R.M., 2013. Role of hot and cold pixel concept in remote sensing based single source energy balance algorithms Using 21st Century Technology to Better Manage Irrigation Water Supplies Seventh International Conference.
- Pearlmutter, 2001. Ocean circulation: Thermohaline circulation. *Encycl. Atmos. Sci.* 4, 1549-1555.
- Peng, J., Loew, A., 2014. Evaluation of daytime evaporative fraction from MODIS TOA radiances using FLUXNET observations. *Remote Sens.* 6, 5959–5975.
- Pope, G., Treitz, P., 2013. Leaf Area Index (LAI) estimation in boreal mixedwood forest of Ontario, Canada using Light detection and ranging (LiDAR) and worldview-2 imagery. *Remote Sens.* 5, 5040–5063.
- Publisher, A., Norton, A., Report, A., 2017. Field Determination of Permanent Wilting Point Field Determination of Permanent Wilting Point.
- Ramoelo, A., Majozi, N., Mathieu, R., Jovanovic, N., Nickless, A., Dzikiti, S., 2014. Validation of Global Evapotranspiration Product (MOD16) using Flux Tower Data in the African Savanna, South Africa 7406–7423.
- Richardson, A.J., Wiegand, C.L., 1977. Distinguishing vegetation from soil background information. *Photogramm. Eng. Remote Sensing* 43, 1541–1552.
- Roerink, G.J., Su, Z., Menenti, M., 2000. S-SEBI: A simple remote sensing algorithm to estimate the surface energy balance. *Phys. Chem. Earth, Part B Hydrol. Ocean. Atmos.* 25, 147–157.
- Rouse, J.W., Hass, R.H., Schell, J.A., Deering, D.W., 1973. Monitoring vegetation systems in the great plains with ERTS. *Third Earth Resour. Technol. Satell. Symp.* 1, 309–317.
- Roxy, M.S., Sumithranand, V.B., Renuka, G., 2014. Soil heat flux and day time surface energy balance closure at astronomical observatory, Thiruvananthapuram, south Kerala. *J. Earth Syst. Sci.* 123, 741–750.

- Ruhoff, A.L., Paz, A.R., Collischonn, W., Aragao, L.E.O.C., Rocha, H.R., Malhi, Y.S., 2012. A MODIS-based energy balance to estimate Evapotranspiration for clear-sky days in Brazilian tropical savannas. *Remote Sens.* 4, 703–725.
- Rutherford, M.C., Mucina, L., Leslie, W., 2006. *Biomes and Bioregions of Southern Africa*.
- Schmugge, 2002. Remote sensing in hydrology. Elsevier Sci. Ltd 64, 1012–1012.
- Senay, G.B., Budde, M., Verdin, J.P., Melesse, A.M., 2007. A coupled remote sensing and simplified surface energy balance approach to estimate actual evapotranspiration from irrigated fields. *Sensors* 7, 979–1000.
- Senay, G.B., Leake, S., Nagler, P.L., Artan, G., Dickinson, J., Cordova, J.T., Glenn, E.P., 2011. Estimating basin scale evapotranspiration (ET) by water balance and remote sensing methods. *Hydrol. Process.* 25, 4037–4049.
- Shaw, G., Burke, H., 2003. Spectral Imaging for Remote sensing. *Lincoln Lab. J.* 14, 3–28.
- Shoko, C., Dube, T., Sibanda, M., Adelabu, S., 2015. Applying the Surface Energy Balance System (SEBS) remote sensing model to estimate spatial variations in evapotranspiration in Southern Zimbabwe. *Trans. R. Soc. South Africa* 70, 47–55.
- Shoroma, L.B., 2014. Mitigating the effects of recurrent drought: The case of Setlagole community, Ratlou Municipality (North West Province).
- Shuttleworth, J., 2008. Evapotranspiration Measurement Methods. *SouthWest Hydrol.* 22–23.
- Sperna Weiland, F.C., Van Beek, L.P.H., Kwadijk, J.C.J., Bierkens, M.F.P., 2012. Global patterns of change in discharge regimes for 2100. *Hydrol. Earth Syst. Sci.* 16, 1047–1062.
- Stephens, G.L., 2015. The Albedo of Earth. *Rev. Geophys.* 141–163.
- Stephenson, N.L., 1998. Actual evapotranspiration and deficit: biologically meaningful correlates of vegetation distribution across spatial scales. *J. Biogeogr.* 25, 855–870.
- Su, Z., 2002. The Surface Energy Balance System (SEBS) for estimation of turbulent heat fluxes. *Hydrol. Earth Syst. Sci.* 6, 85–100.
- Su, Z., Li, X., Zhou, Y., Wan, L., Wen, J., Sintonen, K., 2003. Estimating areal evaporation from remote sensing. *Geosci. Remote Sens. Symp. 2003. IGARSS'03. Proceedings. 2003 IEEE Int.* 2, 1166–1168.

- Sun, Z., Gebremichael, M., Wang, Q., Wang, J., Sammis, T.W., Nickless, A., 2013. Evaluation of Clear-Sky Incoming Radiation Estimating Equations Typically Used in Remote Sensing Evapotranspiration Algorithms 4735–4752.
- Sun, Z., Wei, B., Su, W., Shen, W., Wang, C., You, D., 2011. Evapotranspiration estimation based on the SEBAL model in the Nansi Lake Wetland of China. *Math. Comput. Model.* 54, 1086–1092.
- Szolgay, J., Hlavčová, K., Kohnová, S., Danihlík, R., 2003. Regional estimation of parameters of a monthly water balance model. *J. Hydrol. Hydromechanics* 51, 256–273.
- Tasumi, M, Trezza, R, Allen, R G, Wright, J L, Tasumi, Masahiro, Trezza, Ricardo, Allen, Richard G, Wright, James L, 2003. Poster Session : available during the workshop U . S
- Teixeira, A.H. de C., 2010. Determining Regional Actual Evapotranspiration of Irrigated Crops and Natural Vegetation in the São Francisco River Basin 1287–1319.
- Thornton, P.K., Jones, P.G., Ericksen, P.J., Challinor, A.J., 2011. Agriculture and food systems in sub-Saharan Africa in a 4 C+ world. *Philos. Trans. R. Soc. A Math. Phys. Eng. Sci.* 369, 117–136.
- Timmermans, W.J., Kustas, W.P., Anderson, M.C., French, A.N., 2007. An intercomparison of the Surface Energy Balance Algorithm for Land (SEBAL) and the Two-Source Energy Balance (TSEB) modeling schemes. *Remote Sens. Environ.* 108, 369–384.
- Toda, M., 2003. Single level turbulence measurements to determine roughness parameters of complex terrain. *J. Geophys. Res.* 108, 4363.
- Todd, R.W., Klocke, N.L., Hergert, G.W., Parkhurst, A.M., 1991. Evaporation from soil influenced by crop shading, crop residue, and wetting regime. *Trans. ASAE.*
- Trenberth, K.E., Smith, L., Qian, T., Dai, A., Fasullo, J., 2007. Estimates of the Global Water Budget and Its Annual Cycle Using Observational and Model Data. *J. Hydrometeorol.* 8, 758–769.
- Trlica, Hutyra, Schaaf, Erb, Wang, 2017. Earth ' s Future Albedo , Land Cover , and Daytime Surface Temperature Variation Across an Urbanized Landscape Earth ' s Future.
- Tsouni, A., Kontoes, C., Koutsyiannis, D., Elias, P., Mamassis, N., 2008. Estimation of actual evapotranspiration by remote sensing: Application in Thessaly plain, Greece. *Sensors* 8, 3586–3600.

- Valipour, M., 2015. Importance of solar radiation, temperature, relative humidity, and wind speed for calculation of reference evapotranspiration. *Arch. Agron. Soil Sci.* 61, 239–255.
- Verstraeten, W.W., Veroustraete, F., Feyen, J., 2008. Assessment of evapotranspiration and soil moisture content across different scales of observation. *Sensors* 8, 70–117.
- Vey, S., Güntner, A., Wickert, J., Blume, T., Ramatschi, M., 2016. Long-term soil moisture dynamics derived from GNSS interferometric reflectometry: a case study for Sutherland, South Africa. *GPS Solut.* 20, 641–654.
- Visser, J.N.J, Looock, J.C. and, Jordaan, M.J., 1980. Permian Deltaic Sedimentation in the Western Half of the Karoo Basin, South Africa. *Trans. Geol. Soc. South Africa* 83, 415–424.
- Weligepolage, K., 2005. ESTIMATION OF SPATIAL AND TEMPORAL DISTRIBUTION OF EVAPOTRANSPIRATION BY SATELLITE REMOTE SENSING A case study in Hupselse Beek , The Netherlands ESTIMATION OF SPATIAL AND TEMPORAL DISTRIBUTION OF EVAPOTRANSPIRATION BY SATELLITE REMOTE SENSING A case stud.
- Wu, B., Liu, S., Zhu, W., Yan, N., Xing, Q., Tan, S., 2017. An Improved Approach for Estimating Daily Net Radiation over the Heihe River Basin. *Sensors* 17, 86.
- Wubet, M.T., 2003. Estimation of Absolute Surface Temperature By Satellite Remote Sensing 121.
- WWF-SA, 2016. Water: facts and futures 96.
- Yocum, L.E., 1935. stag,es. *Plant Physiol.* 795–801.
- Yoshioka, H., Miura, T., Demattê, J.A.M., Batchily, K., Huete, A.R., 2010. Soil line influences on two-band vegetation indices and vegetation isolines: A numerical study. *Remote Sens.* 2, 545–561.
- Zhao, L., Xia, J., Xu, C. yu, Wang, Z., Sobkowiak, L., Long, C., 2013. Evapotranspiration estimation methods in hydrological models. *J. Geogr. Sci.* 23, 359–369.

Appendix A

Calculation of net emissivity, utilised for Net long wave radiation, for the image acquired on the 8th of December 2009.

$$\varepsilon_a = 1.24 \left(\frac{e_d}{T_a + 273} \right)^{1/7}$$

$$e_s = 0.6108 \exp\left(\frac{17.27 * T_a}{T_a + 237.3}\right)$$

$$e_d = \frac{RH}{100 * e_s}$$

$$RH = 76.84$$

$T_a = 13.11$. Both Air temperature and relative humidity readings are collected from the meteorological station

$$e_s = 6.108 \left(\frac{17.27 * 13.11}{13.11 + 237.3} \right) = 1.51$$

$$e_d = \frac{88.7}{100} * 1.51 = 1.16$$

e_d = water vapor pressure

T_a = air temperature in celsius

ε_a = apparent emissivity

Calculation of net emissivity, utilised for Net long wave radiation, for the image acquired on the 24th of December 2009.

$$\epsilon_a = 1.24 \left(\frac{e_d}{T_a + 273} \right)^{1/7}$$

$$e_s = 0.6108 \exp\left(\frac{17.27 * T_a}{T_a + 237.3}\right)$$

$$e_d = \frac{RH}{100 * e_s}$$

$RH = 76.84$.

$T_a = 13.11$. Both Air temperature and relative humidity readings are collected from the meteorological station

$$e_s = 6.108 \left(\frac{17.27 * 11.72}{11.72 + 237.3} \right) = 1.55$$

$$e_d = \frac{56.75}{100} * 1.51 = 0.69$$

Where:

e_d = water vapor pressure

T_a = air temperature in celsius

ϵ_a = apparent emissivity

Calculation of net emissivity, utilised for Net long wave radiation, for the image acquired on the 9th of December 2009.

$$\epsilon_a = 1.24 \left(\frac{e_d}{T_a + 273} \right)^{1/7}$$

$$e_s = 0.6108 \exp\left(\frac{17.27 * T_a}{T_a + 237.3}\right)$$

$$e_d = \frac{RH}{100 * e_s}$$

Where:

$$RH = 33.98$$

$T_a = 21.46$. Both Air temperature and relative humidity readings are collected from the meteorological station.

$$e_s = 6.108 \left(\frac{17.27 * 21.46}{21.46 + 237.3} \right) = 2.55$$

$$e_d = \frac{33.98}{100} * 2.55 = 0.86$$

Where:

e_d = water vapor pressure

T_a = air temperature in celsius

ϵ_a = apparent emissivity

Appendix B

Both these figure were used to solve the correlation coefficients for images acquired on the 24th and the 9th of December 2009.

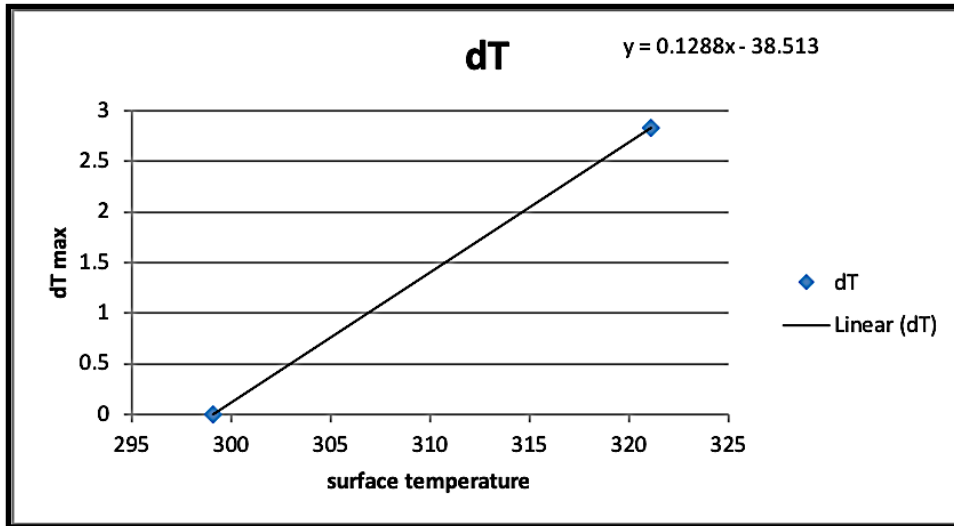


Figure 28: Solving for correlation coefficient satellite for satellite image acquired on the 24th of December 2009

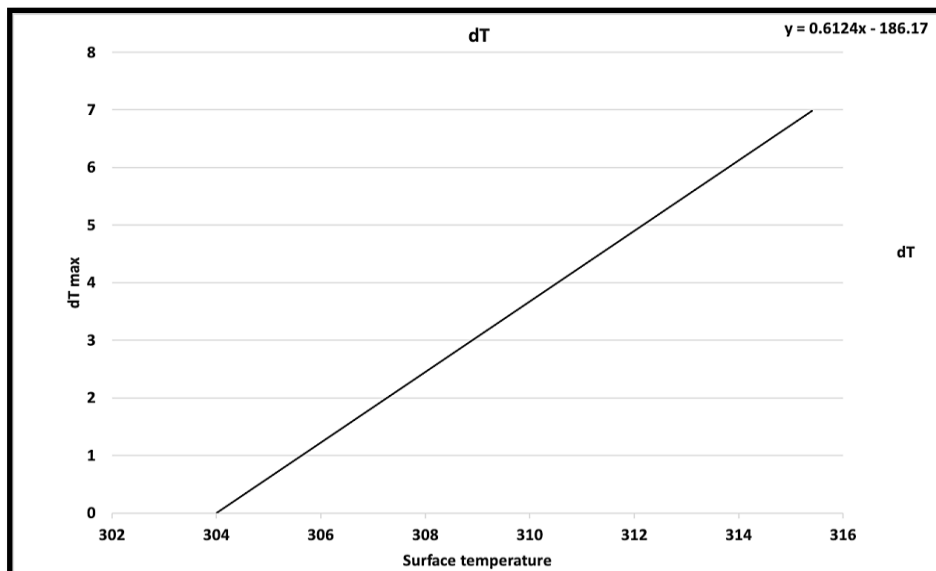


Figure 29: Solving for correlation coefficient for satellite image acquired on the 9th of January 2010

Appendix C

The iterative process for stabilising the final sensible heat flux value is depicted in the figures below. This process was done for all three satellite images and until a stable value was found.

disheight	Column1	Ψ_h	Ψ_m	Ustar	rah	dTmax	L	Xh	Xm	Ψ_{h2}	Ψ_{m3}
0.572	Step1	0	0	0.0293	213.423	52.35259	44309.7	1	1.009	0.0003	0.0084
	Step2	0.0003	0.0084	0.7442	13.99	3.431742	1516783.9	1	1	0	-0.0005
	Step3	0	-0.0005	0.7432	14.01	3.436648	-503559.2	1	0.999	0	-0.0016
	Step4	0	-0.0016	0.7431	14.01	3.436648	-503356.0	1	0.999	0	-0.0016
	Step5	0	-0.0016	0.7431	14.01	3.436648	-503356.0	1	0.999	0	-0.0016
	Step6	0	-0.0016	0.7431	14.01	3.436648	-503356.0	1	0.999	0	-0.0016

Figure 30: Iterative process for stabilising the sensible heat flux value, for the image acquired on the 8th of December 2009

disheight	Column1	Ψ_h	Ψ_m	Ustar	rah	dTmax	L	Xh	Xm	Ψ_{h2}	Ψ_{m3}
0.6	Step1	0	0	0.0499	149.538	24.70453	-8931.3	0.999	0.999	-0.0013	-0.0014
	Step2	-0.0013	-0.0014	0.743	13.767	2.28074	15629.7223	1	1	0.0007	-0.0004
	Step3	0.0007	-0.0004	0.743	17.147	3.436648	5774.664	1	0.999	0	-0.0016
	Step4	0	-0.0016	0.7431	14.01	3.436648	-503356.0	1	0.999	0	-0.0016
	Step5	0	-0.0016	0.7431	14.01	3.436648	-503356.0	1	0.999	0	-0.0016
	Step6	0	-0.0016	0.7431	14.01	3.436648	-503356.0	1	0.999	0	-0.0016

Figure 31: Iterative process for stabilising the sensible heat flux value, for the image acquired on the 24th of December 2009

disheight	Column1	Ψ_h	Ψ_m	Ustar	rah	dTmax	L	Xh	Xm	Ψ_{h2}	Ψ_{m3}
0.6	Step1	0	0	0.0547	129.739	45.0624	0.2	1.62	1.62	1.1898	0.6695
	Step2	1.1898	0.6695	0.7	17.2	5.974096	17671.4	1	1	0.0006	-0.0005
	Step3	0.0006	-0.0005	0.6	20.1	3.436648	9164.513	1.001	1.001	0.0012	-0.0002
	Step4	0.0012	-0.0002	0.6	20.1	3.436648	9164.513	1.001	1.001	0.0012	-0.0002
	Step5	0.0012	-0.0002	0.6	20.1	3.436648	9164.513	1.001	1.001	0.0012	-0.0002
	Step6	0.0012	-0.0016	-0.0002	20.1	3.436648	9164.513	1.001	1.001	0.0012	-0.0002
	step7	0.0012	-0.0016	-0.0002	20.1	3.436648	9164.513	1.001	1.001	0.0012	-0.0002
	step8	0.0012	-0.0016	-0.0002	20.1	3.436648	9164.513	1.001	1.001	0.0012	-0.0002

Figure 32: Iterative process for stabilising the sensible heat flux value, for the image acquired on the 9th of January 2010